

DETECTION OF LANDSLIDES BY OBJECT-  
ORIENTED IMAGE ANALYSIS

**Tapas Ranjan Martha**

## **Examining Committee**

Prof.dr. Freek van der Meer  
Prof.dr. Andrew Skidmore  
Prof.dr. Leonardo Cascini  
Dr. K. Vinod Kumar  
Dr. Miet Van Den Eeckhaut

University of Twente  
University of Twente  
University of Salerno, Italy  
NRSC, India  
JRC, Italy

ITC dissertation number 189  
ITC, P.O. Box 217, 7500 AE, Enschede, The Netherlands

ISBN 978-90-6164-309-8  
Cover designed by Benno Masselink / Job Duim  
Printed by ITC Printing Department  
Copyright © 2011 by Tapas Ranjan Martha

This doctoral dissertation was produced with the support of:

- Faculty of Geo-information Science and Earth Observation (ITC), University of Twente, Enschede, The Netherlands
- National Remote Sensing Centre (NRSC), Indian Space Research Organisation (ISRO), Hyderabad, India



**UNIVERSITY OF TWENTE.**

**ITC**

FACULTY OF GEO-INFORMATION SCIENCE AND EARTH OBSERVATION



**Indian Space Research Organisation**

# DETECTION OF LANDSLIDES BY OBJECT-ORIENTED IMAGE ANALYSIS

DISSERTATION

To obtain  
the degree of doctor at the University of Twente,  
on the authority of the Rector Magnificus,  
prof.dr. H. Brinksma,  
on account of the decision of the graduation committee,  
to be publicly defended  
on Monday, 04 July 2011 at 13:30 hrs

by

**Tapas Ranjan Martha**

born on 05 August 1977

in Begunia, Khurda district, Odisha state, India

This thesis is approved by

**Prof. Dr. V. G. Jetten**, promotor

**Dr. C. J. van Westen**, assistant promotor

**Dr. N. Kerle**, assistant promotor

*To my beloved father late B. N. Martha*



## Acknowledgements

There are many people who have contributed towards the completion of the thesis. However, there are few, whom I would like to mention by name.

First of all, I express my sincere gratitude to National Remote Sensing Centre (NRSC) for providing me the opportunity to pursue PhD at ITC, The Netherlands. The support of Dr. K. Radhakrishnan, Chairman, Indian Space Research Organisation (ISRO) and Secretary, Department of Space, Government of India, Dr. G. Madhavan Nair, former Chairman, ISRO, Dr. R. Navalgund, Director, SAC, Dr. V. Jayaraman, former Director, NRSC is gratefully acknowledged. My sincere thanks to Dr. V. K. Dadhwal, Director, NRSC and Dr. P. S. Roy, Director, IIRS for their technical guidance and continuous encouragement during the PhD period. I express my thankfulness to United Nations University—ITC School for Disaster Geo-Information Management (UNU-DGIM) under which this research was carried out. The support of Prof. Martin Hale, Dr. Paul van Dijk and Drs. Sjaak Bereens of ITC, The Netherlands is gratefully acknowledged.

I thank Shri G. Behera, Dy. Director, RSGIS-AA, NRSC for his support to this PhD programme. Controller, NRSC and Dr. M. V. Krishnarao, former Group Head, PPEG, NRSC provided administrative support at various stages of the PhD course and I am obliged to them. The support of Shri M. V. V. Kamaraju, former Head, Geosciences division during the initial stage of the PhD programme is thankfully acknowledged.

I would like to thank Dr. N. Rajendran, Dr. K. Vinod Kumar and Dr. Cees J. van Westen, the three key persons of the GSI-NRSC-ITC joint agreement on landslide studies under which I was nominated for this research activity. Without their initiative perhaps it would have been difficult for me to come to ITC for PhD.

My PhD supervisors deserve special thanks for training me to build a temperament for the systematic investigation of a scientific problem. Particularly, I owe a lot to Dr. Norman Kerle for his constructive criticism, encouragement, and teaching me the styles of scientific writing and presentation. Without his valuable and timely comments it would have been difficult to complete this dissertation. It was great pleasure to work with Prof. Victor Jetten. He always advised me to stay focussed on my research problems. Dr. Cees J. van Westen, whom I knew before coming to ITC, shared his vast experience in the landslide field that helped me to solve some of my important research questions. Dr. K. Vinod Kumar provided valuable

support for the fieldwork and also during the critical period of the PhD while working in India. I sincerely thank all my supervisors for being so supportive and friendly throughout the PhD period. It was an unforgettable experience in working with them.

ITC provided me a very good working atmosphere during the hectic days of my PhD research. I would like to thank the staff of ITC Hotel, ITC library and help desk, Ms. Loes Colenbrander and Ms. Marjolein Woerle for their great support during my stay at ITC.

I had several useful discussions with my three PhD mates, Saibal Ghosh, Pankaj Jaiswal from GSI and Iswar Chandra Das from ISRO, and we learned a lot from each other. I thank them for sharing their individual experiences, which were beneficial to my research. The landslide literature database and endnote library created by Enrique Castellanos was of immense help in writing papers and this thesis. I thank him for sharing it. It was great to be a part of the ITC Indian community and we shared a lot of common time, coffee breaks, and organised get-togethers, which provided a homely atmosphere though away from home. Thanks friends - the list is really long, my association with you and with families of some of you in Enschede will be difficult to forget. My other ITC office mates Fei Teng, Jahanzeb Malik, Longhui Li, Andre Stumpf provided a very good working atmosphere. Thanks for tolerating me during some of the discussions. My colleagues in the Geosciences and Hydrogeology divisions at NRSC, Hyderabad provided a healthy environment during my PhD work and I thank them all.

Needless to say, it would have been very difficult to finish the PhD without the support of my family. I thank them, particularly, my wife Swarnalika for taking care of our son Adarsh during my absence from India. Towards the completion of the thesis I was blessed with my daughter Prishika. It will remain as a cherishable moment in my post PhD life.

Finally, I pay my obeisance to the almighty for being so kind to me during this period of trials and tribulations.

**Tapas R. Martha**

04 July 2011

# Table of Contents

Acknowledgements.....	i
List of figures .....	vi
List of tables.....	viii
List of acronyms .....	ix
<b>Chapter 1</b> .....	<b>1</b>
<b>Introduction</b> .....	<b>1</b>
1.1 Problem statement .....	1
1.2 Remote sensing for landslide inventory mapping .....	2
1.3 Research objectives .....	4
1.4 Test area.....	5
1.5 Structure of the thesis.....	7
<b>Chapter 2</b> .....	<b>9</b>
<b>Accuracy Assessment of DSMs</b> .....	<b>9</b>
2.1 Introduction.....	9
2.1.1 Automatic DSM generation .....	12
2.2 Study area.....	13
2.3 Methods .....	14
2.3.1 DGPS survey .....	14
2.3.2 Processing of Cartosat-1 data .....	15
2.3.3 Accuracy assessment.....	16
2.3.4 Effect of valley orientation.....	19
2.4 Results.....	21
2.4.1 DSM Global accuracy .....	21
2.4.2 Effect of valley orientation on DSM accuracy .....	22
2.4.3 Effect of shadow on DSM generation .....	22
2.5 Discussion .....	23
2.6 Conclusion .....	27
Acknowledgements.....	28
<b>Chapter 3</b> .....	<b>29</b>
<b>Volumetric analysis of landslides</b> .....	<b>29</b>
3.1 Introduction.....	29
3.1.1 Landslide volume estimation.....	30
3.2 Area and data analysis .....	32
3.2.1 Test area .....	32
3.2.2 DSM generation.....	33
3.2.3 Volumetric analysis .....	36
3.3 Results and discussion.....	36
3.3.1 Accuracy assessment of volume .....	39
3.4 Conclusion .....	40
Acknowledgements.....	41
<b>Chapter 4</b> .....	<b>43</b>
<b>Characterisation and detection of landslides</b> .....	<b>43</b>
4.1 Introduction.....	43

4.2	Landslide characterisation from satellite data and DEM.....	46
4.3	Materials and methods .....	48
4.3.1	Study area.....	48
4.3.2	Data sources .....	49
4.3.2.1	Satellite data .....	49
4.3.2.2	DEM .....	49
4.3.3	Segmentation technique .....	50
4.3.4	Approach for landslide recognition and classification.....	51
4.3.4.1	Identification of landslide candidates (Step-1) .....	51
4.3.4.2	Separation of landslides from false positives (Step-2).....	51
4.3.4.3	Identification of landslide types (Step-3) .....	53
4.4	Results.....	54
4.4.1	Extraction of landslide candidate objects .....	54
4.4.2	Landslide recognition.....	55
4.4.3	Landslide classification.....	59
4.4.4	Accuracy assessment.....	61
4.5	Discussion .....	63
4.6	Conclusion .....	66
<b>Chapter 5</b>	.....	<b>69</b>
<b>Segment optimisation and data-driven thresholding</b>	.....	<b>69</b>
5.1	Introduction.....	69
5.2	Segmentation and thresholding methods.....	71
5.2.1	Segmentation methods.....	71
5.2.2	Thresholding methods .....	73
5.3	Data set, area and methodology .....	73
5.3.1	Knowledge-based detection of landslides .....	74
5.3.2	Optimisation of segments (Sub-module 1) .....	75
5.3.2.1	Optimisation strategy with objective function .....	77
5.3.3	Extraction of landslide candidates (Sub-module 2) .....	78
5.3.3.1	Thresholding by K-means .....	78
5.3.4	Identification of false positives (Sub-module 3) .....	79
5.3.4.1	Linking optimal scales.....	79
5.3.5	Classification of landslides (Sub-module 4) .....	79
5.3.6	Transferability of the method.....	80
5.4	Results.....	80
5.4.1	Training area (Okhimath) result .....	84
5.4.2	Testing area (Darjeeling) result.....	88
5.5	Accuracy assessment .....	89
5.6	Conclusion .....	94
	Acknowledgement .....	95
<b>Chapter 6</b>	.....	<b>97</b>
<b>Historical landslide inventories from panchromatic images</b>	.....	<b>97</b>
6.1	Introduction.....	97
6.2	Materials and method.....	99
6.2.1	Data sources .....	99
6.2.2	Pre-processing of satellite data .....	100
6.2.2.1	Image geometric correction .....	100
6.2.2.2	TOA reflectance calculation.....	100
6.2.2.3	Image Normalisation .....	101

6.2.3 Detection approach .....	102
6.2.3.1 Identification of landslide candidates .....	102
6.2.3.2 Identification landslide false positives .....	104
6.2.3.3 Classification of landslide types .....	104
6.2.3.4 Detection from time-series images.....	104
6.3 Results and discussion.....	106
6.3.1 Landslide candidates .....	106
6.3.2 Detection of landslides.....	107
6.3.4 Accuracy assessment.....	111
6.3.4.1 Comparing landslide density .....	115
6.4 Conclusion.....	117
Acknowledgements.....	118
<b>Chapter 7</b> .....	119
<b>Use of semi-automatically derived landslide inventories</b> .....	119
7.1 Introduction.....	119
7.2 Methodology and data .....	120
7.2.1 Preparation of multi-temporal landslide inventory .....	121
7.2.2 Generation of landslide susceptibility map .....	123
7.2.2.1 Input data.....	123
7.2.2.2 Weights of evidence (wofe) method .....	125
7.2.3 Landslide hazard assessment.....	127
7.2.3.1 Estimation of spatial probability.....	127
7.2.3.2 Estimation of temporal probability .....	127
7.2.4 Landslide risk assessment .....	128
7.3 Results and discussion.....	130
7.3.1 Landslide susceptibility assessment .....	130
7.3.2 Landslide hazard assessment.....	135
7.3.3 Risk assessment .....	135
7.4 Conclusion .....	137
Acknowledgements.....	138
<b>Chapter 8</b> .....	139
<b>Synthesis</b> .....	139
8.1 Introduction.....	139
8.2 The role of DEM for detection of landslides .....	140
8.3 Knowledge-based object-oriented method .....	141
8.3.1 Detection of landslides using multispectral images .....	141
8.3.2 Detection of landslides using panchromatic images .....	143
8.4 Use of the semi-automated landslide detection technique .....	144
8.4.1 Rapid event-based mapping .....	144
8.4.2 Hazard and risk assessment .....	145
8.5 Future work .....	146
8.5.1 Towards an operational method in India .....	147
<b>Bibliography</b> .....	149
<b>Summary</b> .....	161
<b>Samenvatting</b> .....	165
<b>Biography</b> .....	169
<b>Publications</b> .....	170
<b>ITC Dissertation List</b> .....	171

## List of figures

Figure 1.1: Cartosat-1 image showing landslides. ....	2
Figure 1.2: Conceptual diagram showing the methodology. ....	4
Figure 1.3: Location of the test area. ....	6
Figure 2.1: Schematic diagram showing occlusion and shadow.....	13
Figure 2.2: 3D perspective view of Okhimath, India. ....	15
Figure 2.3: 3D terrain profile extracted using LPS and SAT-PP .....	17
Figure 2.4: 10 m DSM extracted from the Cartosat-1 data. ....	19
Figure 2.5: Drainage line buffer used for calculation of spatial accuracy. ....	20
Figure 2.6: Drainage comparison for valley orientations. ....	24
Figure 2.7: Difference in the distribution and density of matched points .....	25
Figure 2.8: Field photograph showing typical topography of Okhimath .....	26
Figure 2.9: Local image contrast explained with histograms .....	27
Figure 3.1: 3D and ground view of the Salna landslide.....	33
Figure 3.2: Cartosat-1 orthoimage of the Salna landslide. ....	34
Figure 3.3: Pre- and post-failure surface profile .....	38
Figure 3.4: Volumetric analysis of the Salna landslide.....	39
Figure 4.1: Schematic block diagrams of landslide types .....	48
Figure 4.2: Methodology flowchart for detection of landslides .....	52
Figure 4.3: Multiresolution segmentation of LISS-IV image.....	55
Figure 4.4: Quantitative classification criteria for false positives .....	56
Figure 4.5: Image object and stream network .....	57
Figure 4.6: Field photograph of a typical agricultural terrace.....	58
Figure 4.7: Relationship between landslide and road object axes.....	58
Figure 4.8: Resegmentation and merging of objects .....	60
Figure 4.9: Quantitative classification criteria for landslide types. ....	61
Figure 4.10: Landslides automatically detected.....	62
Figure 4.11: Relationship between landslide area and frequency. ....	66
Figure 5.1: Concept diagram for knowledge-based detection of landslide....	76
Figure 5.2: Spatial structure of most common landslide false positives.....	80
Figure 5.3: Objective function for Okhimath and Darjeeling .....	81
Figure 5.4: Important stages towards successful landslide recognition .....	84
Figure 5.5: Statistical evaluation of clusters of brightness and hillshade .....	86
Figure 5.6: Landslides correctly recognised in the Okhimath area. ....	87
Figure 5.7: Effect of multi-scale classification of false positives .....	88
Figure 5.8: Effect of segment optimisation on a large landslide. ....	89
Figure 5.9: Landslides correctly recognised in the Darjeeling area .....	90
Figure 5.10: Comparison of the accuracies.....	91
Figure 6.1 Post-and pre-landslide images for change detection .....	103
Figure 6.2 Detection from multi-temporal panchromatic images. ....	106
Figure 6.3 Objective function curves for panchromatic images. ....	108
Figure 6.4 Extraction of landslide candidates from panchromatic images. .	109
Figure 6.5 Usefulness of texture for identification of false positives.....	110

Figure 6.6 Independent annual inventory of landslides (1998–2006).....	112
Figure 6.7 Monitoring of an active landslide.....	113
Figure 6.8 Accuracy assessment for number and extent of landslides.....	114
Figure 6.9 Detection of translational rock slide .....	115
Figure 6.10 Comparison of landslide density.....	116
Figure 7.1 Procedure for landslide hazard and risk assessment .....	122
Figure 7.2 Mean monthly rainfall pattern in the study area for 34 years. ...	122
Figure 7.3 Layers used for preparation of landslide susceptibility map.....	125
Figure 7.4 Contrast values for all classes of the seven evidence layers .....	131
Figure 7.5 Analysis of wofe model for landslide susceptibility mapping .....	133
Figure 7.6 Landslide susceptibility map of the Okhimath area .....	134
Figure 7.7 ROC curve of the wofe model. ....	135
Figure 7.8 Gumbel plot for estimating the return period. ....	136
Figure 7.9 Total risk due to landslide in the Okhimath area.....	137

## List of tables

Table 2.1: RMSE of control point residuals after block orientation. ....	16
Table 2.2: Statistical assessment of the global accuracy of DSMs .....	21
Table 2.3: Reliability of the vertical global accuracy of both the DSMs .....	21
Table 3.1: Quantitative comparison of volume. ....	37
Table 4.1: Landslide false positives and their logical classification criteria ...	53
Table 4.2: Landslide types and their logical classification criteria. ....	54
Table 4.3: Accuracy assessment for the number of landslides. ....	63
Table 4.4: Accuracy assessment for the extent (km <sup>2</sup> ) of landslides. ....	63
Table 5.1: Description of study areas .....	75
Table 5.2: Characteristic features of false positives and landslide types.....	82
Table 5.3: NDVI and brightness and hillshade cluster center values .....	85
Table 5.4: Accuracy assessment in the Okhimath area.....	92
Table 5.5: Accuracy assessment in the darjeeling area .....	93
Table 6.1 Details of high resolution panchromatic satellite data used .....	100
Table 6.2 Optimal scales derived using POF .....	107
Table 6.3 Texture measures used for identification of false positives. ....	110
Table 6.4 Comparison of stable and unstable slope facets .....	116
Table 7.1 List of evidence layers and their sources .....	124
Table 7.2 List of evidence classes showing positive correlation .....	132
Table 7.3 Building category in Okhimath area and their vulnerability.....	136

## List of acronyms

CRED	Centre for Research on the Epidemiology of Disasters
COTS	Commercial off the Shelf
DEM	Digital Elevation Model
DGPS	Differential Global Positioning System
DSM	Digital Surface Model
DTM	Digital Terrain Model
EMR	Electro Magnetic Radiation
EO	Earth Observation
FNEA	Fractal Net Evolution Approach
GCP	Ground Control Point
GEOBIA	Geographic object-based image analysis
GPS	Global Positioning System
GLCM	Grey Level Co-occurrence Matrix
GSD	Ground Sampling Distance
LiDAR	Light Detection and Ranging
LISS-IV	Linear Imaging Self-scanning Sensor IV
LPS	Leica Photogrammetric Suite
MCT	Main Central Thrust
NDVI	Normalised Difference Vegetation Index
OBIA	Object-based image analysis
OOA	Object-Oriented Analysis
POF	Plateau Objective Function
RFM	Rational Function Model
RMSE	Root Mean Square Error
RPC	Rational Polynomial Co-efficient
SAR	Synthetic Aperture Radar
SAT-PP	Satellite Precision Positioning
UN/ISDR	United Nations International Strategy for Disaster Reduction



# Chapter 1: Introduction

## 1.1 *Problem statement*

Communities living within mountainous environment may face grave danger from landslide disasters triggered both due to unsustainable anthropogenic activities such as mining, road cutting, and urbanisation and natural causes such as earthquakes and extreme rainfall. According to official figures from the United Nations International Strategy for Disaster Reduction (UN/ISDR) and the Centre for Research on the Epidemiology of Disasters (CRED), landsliding ranked 3<sup>rd</sup> in terms of number of deaths among the top ten natural disasters in 2006 and has affected approximately 4 million people (OFDA/CRED, 2006). The immediate priority after a landslide disaster is to carry out relief and rescue operations, which are often hampered by lack of timely information on the location, number and size of landslides in vastly inaccessible mountainous areas.

Remote sensing technology has been used extensively to provide landslide specific information to policy makers and emergency managers during a disaster period (Metternicht et al., 2005; Tralli et al., 2005). Recent advances in computer vision and machine intelligence have led to the development of new techniques, such as object-oriented analysis (OOA) for automatic content extraction of both man-made and natural geospatial objects from remote sensing images (Akçay and Aksoy, 2008; Holt et al., 2009). Terms similar to OOA and commonly available in literature are OBIA (object-based image analysis) and GEOBIA (geographic object-based image analysis). OOA, wherein the information content of an object is used to classify a landscape, is a step towards replicating the human interpretation process (Navulur, 2007b), and has the potential to accurately and meaningfully detect landslides by integrating the contextual information to image analysis, thereby reducing the time required for creation of landslide inventory for large areas. Figure 1.1 shows an example of the Wenchuan earthquake in 2008, which caused thousands of landslides. Mapping these landslides manually using a stereoscopic image interpretation costs many man months of time (Gorum et al., 2010). Furthermore, the landslide inventory prepared using OOA can easily be converted to GIS data, which then form an input essential for landslide susceptibility, hazard and risk analysis, and thus, can indirectly contribute to the formulation of long-term disaster mitigation strategies.



**Figure 1.1:** Cartosat-1 (2.5 m) image showing numerous landslides triggered by the Great Sichuan Earthquake in China on 12 May 2008. It shows the labour intensiveness of landslide inventory preparation using visual image interpretation technique, particularly when quick results are desirable.

## **1.2 Remote sensing for landslide inventory mapping**

Landslide inventories can make use of a variety of approaches, ranging from manual image interpretation using digital stereo images coupled with field investigations to automatic identification based either on elevation or spectral information, or a combination of both, and a complete list of landslide inventory mapping methods is provided by van Westen et al. (2008). Digital elevation models (DEM) produced from overlapping aerial photographs or stereoscopic satellite images are the major sources of elevation data for landslide studies (van Westen and Lulie Getahun, 2003). Note that the term DEM is used here as a generic descriptor; where appropriate we use the terms digital surface model (DSM) and digital terrain model (DTM) in the remainder of this thesis. A DEM was shown to be useful for estimating the volume of landslides by an elevation change analysis (Kerle, 2002; Tsutsui et al., 2007). Shaded relief images produced from a DEM obtained from light detection and ranging (LiDAR) have proven to be very suitable for generating landslide inventories under forest areas in hilly regions and to refine the boundaries of landslides prepared during field investigations. These data are not only useful for mapping old landslides but also can improve field surveys in regions with subdued morphology (van Den Eeckhaut et al., 2007). Microwave remote sensing, such as synthetic aperture radar (SAR) images are also useful for the identification of landslides, and particularly with SAR interferometry, subtle movement of landslides can be picked up from

interferograms generated from SAR image sequences (Singhroy and Molch, 2004). Another advantage of SAR data over optical sensor data is its all weather monitoring ability. Therefore, a combination of SAR imagery with high resolution optical multispectral imagery is useful for monitoring landslides in mountainous areas (Tsutsui et al., 2004). However, problems such as foreshortening and layover effects associated with SAR data in mountainous areas have to be addressed carefully.

The availability of a new generation of high resolution optical satellite imageries (e.g. WorldView, GeoEye, SPOT-5, Resourcesat, Cartosat, Formosat and ALOS-PRISM) has caused a paradigm shift in the use of Earth observation (EO) data for landslide studies. The number of such satellites is increasing year by year (van Westen et al., 2008) which reduces the revisit time, and thus has led to their increased preference over aerial photographs for landslide inventory mapping using visual interpretation technique. Previous researchers attempted to automatically identify landslides using spectral information. Change detection and image fusion are examples of such methods used to identify landslides automatically (Nichol and Wong, 2005b). However, change detection requires a minimum of two images (pre- and post-event), which are not always available from the same sensor, and the atmospheric conditions and the bandwidth of spectral channels may also be different, which makes the image standardisation difficult. Moreover, it is a pixel-based method and geomorphic processes such as landslides cannot be represented only with pixel digital number (DN) values. Therefore, objects (groups of homogeneous pixels) can better identify landslides by bringing in the landslide process information in the form of shape, size and context to image analysis. Since landsliding is a geomorphic process, using DEMs as additional data during image analysis will yield better classification result in comparison to spectral data alone (Florinsky, 1998). OOA has also the potential to include morphometric information derived from a DEM.

Object-based identification of landslides from high resolution data is more appropriate than the pixel-based methods, since with higher resolution landslides are represented by a large number of pixels in comparison to fewer pixels of coarse resolution images. Therefore, context information is more useful than the spectral information alone, when classification is attempted with high resolution images. OOA supports rule-based classification, wherein expert knowledge can also be incorporated to increase the accuracy of classification results in comparison to the traditional nearest neighbourhood classification (Daniels, 2006) (Figure 1.2). OOA for landslide studies is an emerging topic of research, since it has the potential to detect landslides rapidly for a very large area, particularly in the aftermath of a disastrous

event such as earthquake or cyclonic storms. Rapid landslide inventory will enable efficient disaster response planning. Although previous researchers, such as Barlow et al. (2006; 2003) and Moine et al. (2009), have attempted object-based detection of landslides, a comprehensive characterisation and development of a generic method for the detection of landslides is still lacking.

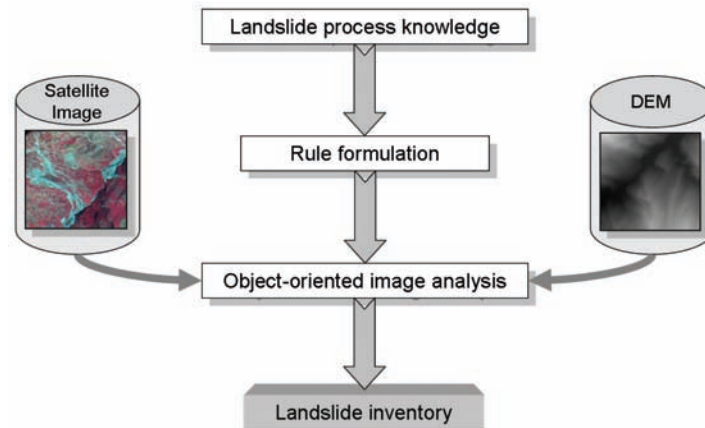


**Figure 1.2:** Conceptual diagram showing the methodology for the detection of landslides by OOA.

### 1.3 Research objectives

The main research objective is to develop a knowledge-based generic spectral-spatial-morphometric approach for the detection of landslides from high resolution satellite and DEM data using OOA. The purpose is to rapidly create a landslide inventory for planning disaster response using newly acquired post-event images, and to prepare a historical landslide database by analysing time series images from archives that can be used for landslide susceptibility and hazard mapping essential for preparing long term disaster management strategies. To do this, we first characterised the landslides from an OOA perspective using Resourcesat-1 (5.8 m) multispectral imagery and DEM derived from Cartosat-1 (2.5 m) along-track stereoscopic images. The criteria commonly used by analysts during visual interpretation (Soeters and van Westen, 1996; van Westen et al., 2008) of landslides were applied to image analysis using object-oriented method. Classification of landslide types as per the Varnes' criteria requires information on shape, context and morphometry. The aim is to use morphometric information, such as slope, flow direction, terrain curvature and stream network derived from the DEM, and spectral information such as normalised difference vegetation index (NDVI), brightness, hillshade derived from the multispectral satellite image and various shape-forms (e.g. roundness, compactness and asymmetry) to characterise landslides, and subsequently apply the process knowledge to

classify them. The methodology was tested in two active landslide areas in a steep mountainous terrain in the Indian Himalayas, where image distortion, occlusion and spectral heterogeneity are common, thereby also exploring the potential of OOA for a new class of high resolution data.

The objectives of this dissertation were to:

- assess the accuracy of multi-temporal DEMs extracted from high resolution satellite stereo images to derive elevation and morphometric information to be used in OOA for the identification of landslides.
- verify the requirement of ground truth for DEM generation from Cartosat-1 data for estimating landslide volume.
- characterise landslides using spectral, texture, shape, morphometric and contextual properties determined from high resolution satellite data and DEM, and create a knowledge-based method for the detection of landslides using OOA.
- validate the robustness and transferability of the knowledge-based object-oriented method for the detection of landslides.
- test the usefulness of semi-automatically prepared landslide inventories for landslide hazard and risk assessment.

## **1.4 Test area**

The Himalayas are one of the global hotspots for landslide hazard (Nadim et al., 2006). A test area was selected covering 81 km<sup>2</sup> in parts of the Mandakini river valley in the Western Indian Himalayas around Okhimath town (30° 30' 48" N and 79° 05' 41" E) in the Rudraprayag district of Uttarakhand state, India (Figure 1.3). This area was selected because of the occurrence of many recent landslides of different types associated with a variety of land covers and litho units. Okhimath is situated at an average elevation of 1300 m at the confluence of the Mandakini and Madhyamaheshwar rivers. In August 1998, a total of 466 landslides were triggered by a major rainfall event, which killed 103 people and damaged 47 villages in the entire Mandakini valley (Naithani, 2002). Some of the landslides in the area are as much as a century old but permanently active. The area was divided into two parts, using a watershed divide, into the Madhyamaheshwar sub-catchment (28 km<sup>2</sup>) and the Mandakini catchment (53 km<sup>2</sup>). The landslide detection algorithm was developed for the Madhyamaheshwar sub-catchment and subsequently tested in the Mandakini catchment.

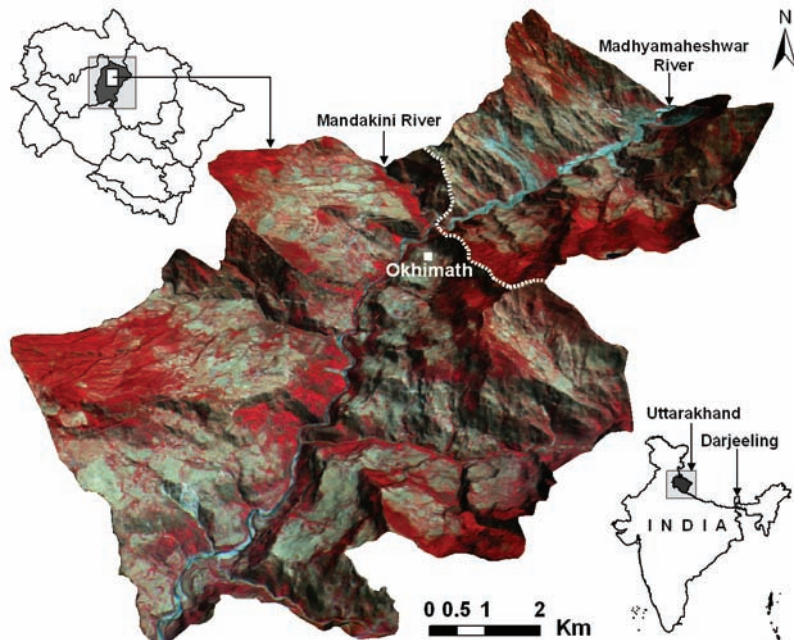


**Figure 1.3:** Location of the test area. White dotted line separates the Madhyamaheshwar and Mandakini catchments.

The area is very rugged, where the elevation ranges between 867 and 2626 m with a high relative relief. Glacial landforms dominate this region, but are frequently modified by denudational activity. Some of the glacial landforms (e.g. moraines and solifluction lobes) with relatively gentle slopes have been converted into terraces for cultivation. Being a tectonically active zone, structural landforms such as escarpments and structurally controlled valleys are also found in this area. Lithological units exposed in this area are granite gneisses, quartzite-sericite schist, quartzite, garnetiferous mica schist, marble and occasional basic intrusives (Rawat and Rawat, 1998). The foliations dip at moderate angles in NE to NNW directions. The main central thrust (MCT) dipping N to NE directions is the cause of neo-tectonic activity in this region, and has caused significant shearing of the rocks, rendering them vulnerable to landsliding. The soil in this area is transported and composed of sub-angular rock fragments with high proportion of sandy to sandy-silty matrix. However, small patches of silty and clayey soil, remnants of glacial deposits, are also present (Rawat and Rawat, 1998). The NE and SW part of the study area is covered by evergreen oak forest.

The methodology developed in the Okhimath area was also applied to another geomorphologically and geologically dissimilar area in the Eastern Indian Himalayas near Darjeeling ( $26^{\circ} 54' 06''$  N and  $88^{\circ} 15' 00''$  E) to test

its robustness and transferability (Figure 1.3). The dominant land use in Darjeeling is tea plantation and semi-urban areas compared to rocky barren land and agricultural terraces in Okhimath. The variability between the two areas offers a good opportunity to verify the generic nature of the rule set developed for the automatic detection of landslides.

## **1.5 Structure of the thesis**

The remainder of the dissertation is organised into six core chapters (2, 3, 4, 5, 6 and 7) and one synthesis chapter (8).

Chapter 2 deals with assessing the accuracy of DSMs extracted from the along-track stereoscopic Cartosat-1 data to derive morphometric information for detection of landslides. The advantages of along-track stereoscopy, such as improved image correlation between the image pairs, and disadvantages, such as poor matching in steep valleys oriented across the satellite track, are discussed in this chapter. The global accuracy of the DSMs is calculated by comparing with the check points collected using differential GPS (DGPS) survey. Drainage lines are used as a proxy for the assessment of error due to spatial auto-correlation.

Chapter 3 makes an attempt to verify the role of ground truth for creation of DSM from Cartosat-1 data for quantifying the volume of landslides. Volumetric analysis was done using pre- and post-event DTMs. This chapter shows how non-uniform vegetation correction using the tree height data is useful for accurate calculation of the landslide volume.

Chapter 4 characterises landslides using their morphometric and spectral properties derived from a high resolution DEM and multispectral satellite image, respectively. Fractal Net Evolution Approach (FNEA), a region growing technique known as multi-resolution segmentation in eCognition software, is used to derive objects/segment from the multispectral image. A knowledge-based method is presented using OOA to classify the object. Initially landslides are detected along with false positives, which are subsequently eliminated leaving only the actual landslides. Five types of landslide using Varnes' criteria (UNESCO-WP/WLI, 1993b) are identified. However, the object size and thresholds used for classification were determined by trial and error method.

Chapter 5 mainly focuses on the creation of a robust and transferable approach to detect landslides by: 1) optimising the segments: and 2) using data-driven rather than user-driven thresholds of landslide diagnostic parameters. Multi-scale classification-based segment optimisation with scale

factor determined from a plateau objective function, an indicator of intrasegment homogeneity and intersegment heterogeneity, is used to detect landslides. Multi-scale treatment of the false positives also helped in reducing the error of commission. In this chapter, the proposed methodology is tested in an independent area.

Chapter 6 presents a method for the detection of landslides from panchromatic images. The object-oriented method discussed in chapters 4 and 5 requires spectral information from NIR and Red bands, and therefore cannot be directly used to detect landslides from greyscale images. In this chapter, time-series images are analysed to create a historical landslide inventory. Local contextual-based threshold coupled with change detection is used to extract landslide candidates. We have used texture, the main information available in panchromatic images to identify false positives. Subsequently, false positives are eliminated and landslides are classified by suitably modifying the methodology explained in chapters 4 and 5.

Chapter 7 deals with the evaluation of the effectiveness of semi-automatically derived landslide inventories for landslide hazard and risk assessment, which is the ultimate goal of any landslide investigation. Multi-temporal inventories created using OOA are used to derive weights for landslide predisposing factors to prepare landslide susceptibility map, which are later integrated with elements at risk, vulnerability and temporal probability for generating a risk curve.

Chapter 8 provides a summary of the obtained results and discusses the advantages and issues of the developed algorithm to detect landslides for the creation of a routine landslide inventory mapping method that can be used operationally. It also discusses the issues related to the creation of DSM in mountainous areas from satellite stereo images using digital photogrammetric techniques.

Overall, the dissertation presents an array of objective and robust methods to create landslide inventories from high resolution EO data, both newly acquired and from the archives.

## Chapter 2: Accuracy Assessment of DSMs\*

This chapter explores the accuracy of digital surface models (DSMs) extracted from the along-track stereoscopic data from Cartosat-1 acquired under high and low sun elevation angle conditions in the High Himalayan terrain. The effect of valley orientation on the spatial accuracy of DSMs which in turn can influence the accuracy of landslide diagnostic parameters is also discussed in this chapter.

### 2.1 Introduction

A Digital Elevation Model (DEM) is one of the primary data sources for the study of earth surface processes. Contours from topographic maps, spot heights measured on the ground using a total station or GPS, LiDAR, interferometric synthetic aperture radar (InSAR) data, aerial photos and satellite images are typical sources for DEM generation (Li et al., 2005; Smith et al., 2006; van Den Eeckhaut et al., 2007; Weibel and Heller, 1991). Techniques for DEM generation have been an active area of research for decades. Over the years, these techniques have been automated and new data sources were developed, most recently based on high resolution stereoscopic data from new satellite missions. Large scale automation and the emergence of new satellite data sources for the generation of DSMs necessitate accuracy testing before the data can be used for terrain analyses. The term DEM has been used widely in the literature as a generic descriptor for digital spatial representations of altitude. In fact the terms DEM, digital terrain model (DTM) and DSM are often used as synonyms. However, when dealing with spatial digital representation of the Earth that include the objects above the surface, such as vegetation and man-made features, the term DSM should be used, whereas DTM is appropriate if the actual ground surface is represented. In this chapter we only use the term DEM in the generic discussion on elevation models.

In photogrammetric processing, the terrain elevation is computed from a satellite stereo pair by measuring the parallax between the two overlapping images. SPOT-5 HRS (high resolution stereoscopic) data have been shown to be a valuable along-track stereoscopic data source for DSM generation (Berthier and Toutin, 2008; Toutin, 2006). Cartosat-1 and ALOS-PRISM are other, more recent, sources of along-track stereoscopic data, with the potential for easier and more accurate DSM generation. They offer considerable advantages compared to across-track methods, such as

---

\* This chapter is based on the article: Martha, T.R., Kerle, N., van Westen, C.J., Jetten, V. and Kumar, K.V. (2010) Effect of sun elevation angle on DSMs derived from Cartosat - 1 data. *Photogrammetric Engineering and Remote Sensing*, 76 (4), 429-438.

employed by the SPOT 1-4 and IRS-1C/D satellites, which are frequently affected by atmospheric differences between the images. Cartosat-1, launched in May 2005 by the Indian Space Research Organisation (ISRO), is a global mission, designed to acquire high resolution stereoscopic images for cartographic application, urban development and disaster management (NRSC, 2006). It is the first satellite in the along-track category with 2.5 m spatial resolution. Cartosat-1 has several distinct features, such as unique sensor geometry, 10-bit radiometric resolution, rational polynomial coefficients (RPC), on-demand tilting capability and five days revisit period with dedicated stereoscopic cameras, making it a suitable choice for DSM generation in any part of the world. Cartosat-1 has two panchromatic cameras, PAN-Aft and PAN-Fore, with an off-nadir viewing angle of  $-5^{\circ}$  and  $+26^{\circ}$ , respectively, acquiring images of a  $900 \text{ km}^2$  area ( $12\,000 \times 12\,000$  pixels) with a gap of 52 seconds (Radhika et al., 2007), minimising radiometric differences. Images are acquired with a base to height ratio (B/H) of 0.62, which is within the suitable range specified by Light et al. (1980) for topographic mapping. Detailed technical specifications of Cartosat-1 are available in NRSC (2006).

The availability of DEMs from global datasets has given rise to new applications (Ehsani and Quiel, 2008; Murphy and Burgess, 2006) and also widened its user community. Also due to commercial off-the-shelf (COTS) software tools, the data are increasingly used by non-photogrammetrists. However, assessing the accuracy of DEMs has always been difficult (Gong et al., 2000; Gooch et al., 1999). While traditional airborne photogrammetric projects covered comparatively small areas and typically used differential GPS (DGPS) to provide needed ground control, satellite-based photogrammetry covers vast areas without the strict need for GPS observations. Particularly, but not exclusively, for non-photogrammetrist assessing the accuracy of the derived data is a substantial challenge. Unfortunately, also commercially generated DEMs contain little information on the error distribution (Holmes et al., 2000). Some standards exist for assessing the absolute accuracy of DEMs. According to FGDC (1998) a minimum of 20 check points is required for calculating the accuracy. Höhle and Potuckova (2006) of the European Spatial Data Research (EuroSDR) group suggested that DTM accuracy assessment methods should be universal, and the reference check points should have accuracies at least 3 to 5 times better than the error metrics of the DTM. Although stereoscopic data from new generation along-track satellites are able to generate high resolution DSMs in a more robust and sophisticated manner, principally through the use of RPCs, the challenge remains to assess their accuracy. DEM accuracy is typically expressed through the root mean square error

(RMSE) of the elevation, calculated by comparing sampled elevation points of the produced DEM with independent ground control points (GCP). This does not, however, result in a representative accuracy figure, as the RMSE is based on only a limited number of points, whereas the DEM contains thousands to millions of elevation points, and thus conveys nothing about the actual error distribution, and little about the accuracy in the vast parts of the DEM where no ground truth exists. In recognition of the limitations of using a small number of GCPs for accuracy assessment, a DEM with higher resolution and better quality can be used as a reference (Bolstad and Stowe, 1994; Gorokhovich and Voustianiouk, 2006). However, suitable reference DEM data are typically not available.

We selected an area in steep, mountainous terrain, where topographic shadows are likely to have a critical effect on photogrammetric DSM generation, a problem we investigate by using recently developed satellite image precision processing (SAT-PP) software (Zhang and Gruen, 2006). In addition to global accuracy assessment using independent check points, we also test the reliability of those values using the models developed by Aguilar et al. (2007).

According to Aguilar et al. (2005) and Chaplot et al. (2006), DEM inaccuracies result from errors in the source data, interpolation method, sampling density, and are also more prominent for steep terrain surfaces. However, in addition, errors in a DEM can also be a function of the viewing direction of the sensor, the valley orientation and the sun elevation angle, effects that have not been studied to our knowledge. In this chapter, along-track stereoscopic Cartosat-1 data acquired in summer and winter seasons of an area in the High Himalayas were analysed to evaluate the accuracy of DSMs as a result of different sun elevation angle conditions and variable valley orientation. Thus implicitly we also consider the effect of local sensor orientation.

Errors in elevation data can have different facets, and therefore, a comprehensive assessment of these possible errors is needed. For example hydrologists and geomorphologists may be less concerned about absolute accuracy, but more about DEM derivatives, such as slope, aspect or curvature (Wise, 2007). However, conceptual challenges persist, e.g. how to compare aspect and slope values from different resolution DEMs, or indeed how to measure those values accurately in the field. Particularly in high-relief terrain, this scale-dependency of derivatives poses immense difficulties. The importance of accuracy assessment of such DEM derivatives has been emphasized by previous workers (Bolstad and Stowe, 1994; Chaplot et al.,

2006; Wise, 2000). Wise (2000) used drainage lines to investigate the effect of different DEM interpolation methods and consequences for hydrological applications. Similarly, Holmes et al. (2000) investigated DEM error distributions in 30 m USGS elevation data using statistical measures, and how these errors propagate into derivatives such as drainage networks. Endreny et al. (2000) assessed the effect of errors in DEMs derived through satellite photogrammetric methods on entire stream networks and basin boundaries. In this chapter we invert this approach by using the drainage network as a proxy in the actual DEM accuracy assessment, a novel departure from previous studies.

### **2.1.1 Automatic DSM generation**

Stereoscopic satellite images are acquired either along or across the track. Satellite photogrammetry using multi-date across-track data first became a viable method for DSM extraction in the 1980s with the availability of SPOT-1 (Kratky, 1989) and IRS-1C/1D data (Bahuguna et al., 2004; Malleswara Rao et al., 1996). However, the difficulty in obtaining cloud free across-track stereo data over large areas prompted the development of a stereo system using along-track images acquired nearly simultaneously (Hirano et al., 2003). This reduces the radiometric variation between the two images of a stereo pair and leads to the extraction of more accurate elevation data (Radhika et al., 2007; Toutin, 2004).

Toutin (2001) gives a detailed description of the methods of DEM extraction from satellite visible and infrared data. An important step in this process is the calculation of elevation parallax for conjugate points. Image matching in mountainous areas frequently fails as a result of shadow or poor contrast in areas of snow, glaciers or homogenous vegetation. Due to different viewing angles of the two cameras in Cartosat-1, steep slopes are also frequently occluded, depending on the steepness of the slope; similarly, the extent of shadow depends upon the sun elevation angle (**Figure 2.1**). Another cause for the partial failure of image matching of along-track stereo pairs in such areas is the relative distortion of features between the two images (Eckert et al., 2005). In such cases image matching produces inaccurate, less dense and irregularly distributed match points. According to Bahuguna et al. (2008) problems in image matching due to steep terrain result in an inaccurate DEM, even with appropriate B/H ratio. Other common problems of image matching for automatic DSM generation are listed by Zhang and Gruen (2006). A list of COTS software for extraction of DSM from stereoscopic data is given by Toutin (2008). These software packages employ various matching algorithms, and should be selected with respect to the data to be used and the terrain characteristics.

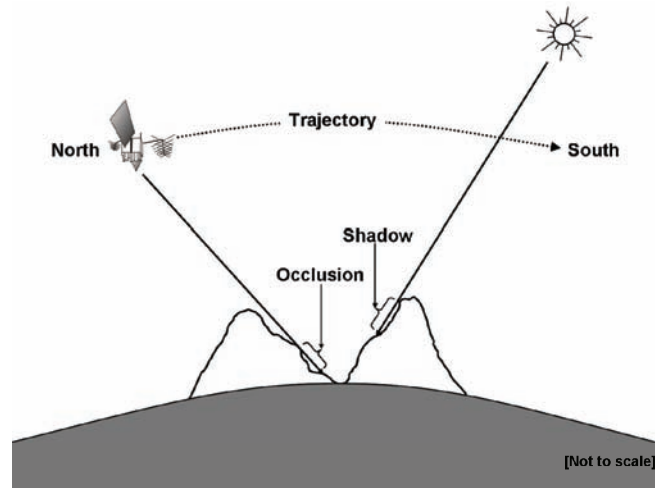


**Figure 2.1:** Schematic diagram showing occlusion on the slope facing south due to high viewing angle of the camera in along-track stereoscopy, and shadow due to steep slope facing north.

A rational function model (RFM) is an alternative to a physical sensor model that facilitates photogrammetric processing of satellite data (Tao and Hu, 2002). The RFM allows users to perform orthorectification and 3D extraction from imagery without having knowledge of the sensor model, and the accuracy of the 3D model can be increased with additional GCPs (Hu and Tao, 2002). The RFMs are generated from onboard instruments, in particular GPS and improvised star sensors, and are provided by the data vendor (Sadasiva Rao et al., 2006). RPCs are determined from RFM and provided to the end user for DSM generation. Since RPCs are terrain independent, they require refinement at scene/block level. Refinement of the orientation result obtained using Cartosat-1 RPC at scene/block level with GCPs can produce a DSM of about four meters vertical accuracy (Ahmed et al., 2007). So far there is no consensus on the optimum number of GCP(s) required for extracting a sufficiently accurate DSM from Cartosat-1 data. Sadasiva Rao et al. (2006) observed that one control point is adequate for restitution of the Cartosat-1 model. However, according to Baltsavias et al. (2007) the distribution of GCPs (planimetric and vertical) is crucial to achieve high accuracy, and they recommended that a minimum of six GCPs should be used for a Cartosat-1 scene.

## 2.2 Study area

Cartosat-1 scene used for DEM generation covers a part of the Mandakini river valley in the High Himalayas (Figure 2.2). The Mandakini river is a tributary to the Ganges river, one of the largest river systems in the world. The elevation ranges from 718 m to 4510 m with highly variable terrain relief

and land cover. The northeastern part of the area is always snow covered. This area is dominated by low altitude oak forest, which does not shed its leaves seasonally. Therefore, the vegetation surface commonly does not change, and is discarded as a potential reason for DSM differences in this chapter. The terrain is dominantly steep and rugged with few flat fluvial terrace areas along the Mandakini river. Since the rugged topography is controlled by the geological structure, there are many fault-related south facing escarpments in this area. The northeastern and western parts of the area are very difficult to access.

## **2.3 Methods**

### **2.3.1 DGPS survey**

The DGPS survey was carried out using three GPS receivers, one located at the base station, operated continuously throughout the survey period, and the remaining two used as rovers to collect ground coordinates in the study area. A Leica SR 520 dual frequency (L1 and L2) receiver was used in the DGPS survey. The DGPS survey in this steep mountainous area was challenging because of terrain inaccessibility, difficulty in identifying ground points, and narrow valleys restricting the satellite signal for the receiver. However, by taking systematic traverses along the accessible routes, 16 points were collected, with a fairly good planimetric and vertical distribution across the scene (Figure 2.2). Post processing of the data recorded in the GPS receivers was carried out using Leica Geo Office software to calculate the co-ordinates of the ground control points. The standard deviation of the errors of elevation, longitude and latitude of the points obtained from the DGPS survey range between 0.10 m to 0.46 m, 0.04 m to 0.15 m and 0.04 m to 0.21 m, respectively.

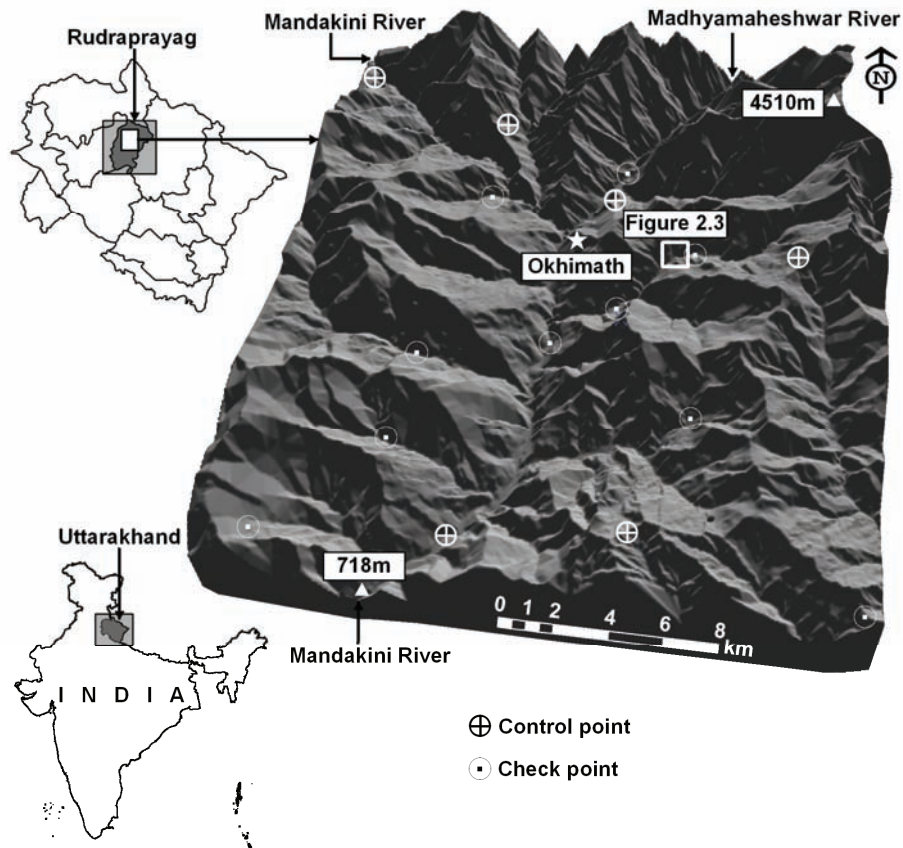


**Figure 2.2:** Location map with 3D perspective view (1.5 times vertical exaggeration) of the study area. South of Okhimath the Mandakini river valley is mainly N-S oriented, while the valleys of the tributaries have a predominant E-W orientation. North of Okhimath, the Mandakini river valley is NW-SE oriented and the Madhyamaheshwar river valley runs NE-SW. White circles represent the DGPS points. Note that the scale is variable.

### 2.3.2 Processing of Cartosat-1 data

Two sets of stereoscopic Cartosat-1 data were processed: one from a summer season (06 April 2006) with a high sun elevation angle ( $62^\circ$ ), and the other from a winter season (01 December 2005) with a low sun elevation angle ( $38^\circ$ ). We first used Leica Photogrammetric Suite (LPS) to process the data. Despite optimisation and adaptation of the extraction strategy, the resulting DSM contained spurious spikes and sinks, an artefact frequently reported in previous studies (Gooch and Chandler, 2001; Gooch et al., 1999; Kerle, 2002).

Manual removal of such spikes and sinks can be attempted, but despite being time-consuming it can only be accurately done with additional data or

extensive stereoscopic assessment of the source image data. Instead, SAT-PP photogrammetric software was used to re-process the data and the resulting DSMs were found to have virtually no spikes and sinks (Figure 2.3). SAT-PP was developed by the Institute of Geodesy and Photogrammetry of ETH Zurich for photogrammetric processing of high resolution images. Unlike LPS, it not only uses a template matching technique, but incorporates an additional edge-matching strategy. It is capable of generating DSMs and orthoimages with pixel level accuracy (Gruen et al., 2007). The general steps of SAT-PP processing of stereoscopic images are: (i) image pre-processing, (ii) multiple primitive multi image matching and (iii) refinement of matching by least square method. Details of these methods are explained in Zhang and Gruen (2006). The advanced matching approach is based on combining matching results of feature points, grid points and edges (Zhang and Gruen, 2006). The approach is robust and has been reported to result in 75% matching success for high resolution stereo pairs even in steep mountainous areas (Zhang and Gruen, 2006). It accounts for both gray scale and geometric differences of features on the ground, thus making it especially useful for mountainous terrain.

**Table 2.1:** RMSE of control point residuals after block orientation.

Elevation model	RMSE <sub>x</sub> (m)	RMSE <sub>y</sub> (m)	RMSE <sub>z</sub> (m)
AprCartoDSM	0.874	0.781	0.465
DecCartoDSM	0.599	0.392	0.972

We used six GCPs as control points to refine the orientation result of the RPC model during the processing of Cartosat-1 data from both seasons. The RMSEs of the residuals obtained after the block triangulation are given in table 2.1. We generated DSMs with 10 m grid size (Figure 2.4), and labelled them as AprCartoDSM and DecCartoDSM for 06 April 2006 and 01 December 2005, respectively.

### **2.3.3 Accuracy assessment**

We calculated the following statistical parameters for global accuracy assessment of the DSMs: RMSE (Aguilar et al., 2005), range, mean error ( $\mu$ ) and standard deviation error ( $\sigma$ ) (Li et al., 2005). Although RMSE is widely used for DEM accuracy assessment, its limitation has also been highlighted (Florinsky, 1998; Wise, 2000). Westaway et al. (2001) suggested that mean error is the true measure of global accuracy as it reflects any systematic bias

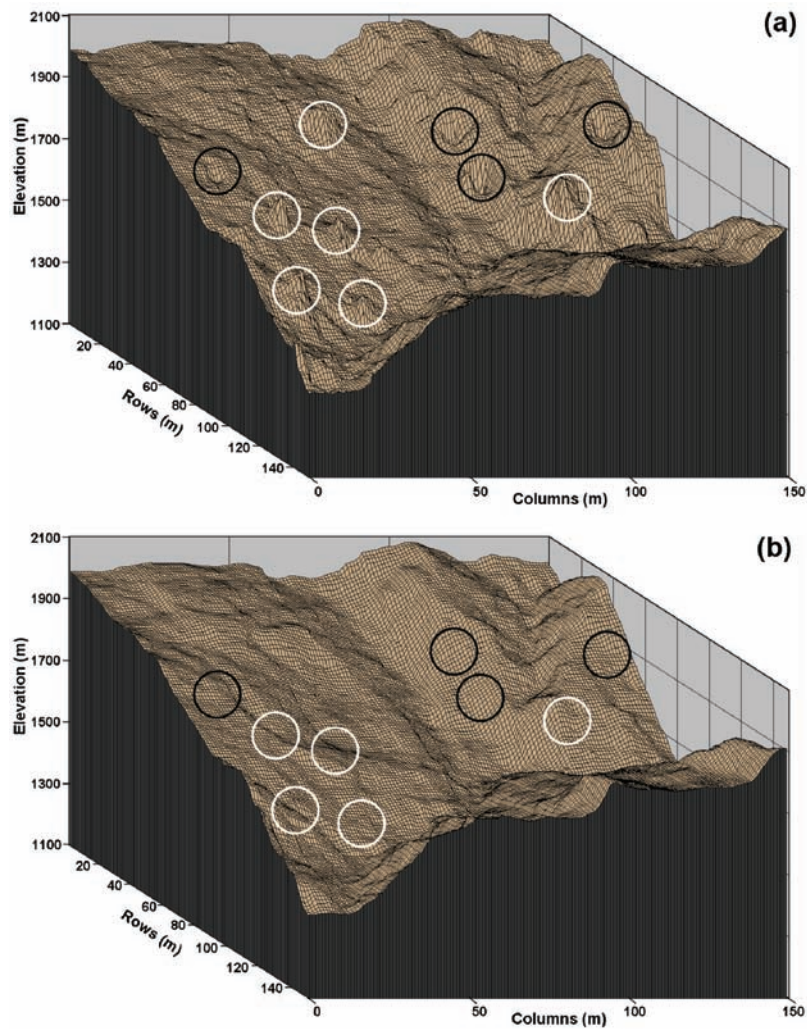


**Figure 2.3:** 3D terrain profile showing the DSM extracted using (a) LPS and (b) SAT-PP. Note the presence of spikes (white circles) and sinks (black circles) in the DSM extracted using LPS, and the absence of the same in the other DSM. Location is shown in figure 2.2.

in the DEM, with the standard deviation showing the error distribution. We calculated these parameters by comparing the check points between the produced and reference data. The check points measured on the ground by DGPS survey are used as reference for comparison. The equations to calculate these errors are given below.

$$Range = e_{\max} - e_{\min} \quad (2.1)$$

$$RMSE = \sqrt{\frac{\sum_{i=1}^n (Z_i^{dsm} - Z_i^{ref})^2}{n}} \quad (2.2)$$

$$\mu = \frac{1}{n} \sum_{i=1}^n (Z_i^{dsm} - Z_i^{ref}) \quad (2.3)$$

$$\sigma = \sqrt{\frac{\sum_{i=1}^n (e_i - \mu)^2}{n-1}} \quad (2.4)$$

where,  $Z^{dsm}$  is elevation of DSM,  $Z^{ref}$  is elevation from reference data,  $n$  is number of point, and  $e_{max}$  and  $e_{min}$  are the maximum and minimum errors, respectively, obtained by comparing the check points from the DGPS survey with the DSM.

In order to estimate the spatial pattern of errors in the DSM, and thus to address DEM accuracy in a more comprehensive way, we used drainage lines as an accuracy proxy. Drainage lines were derived manually from the Cartosat-1 data of 06 April 2006 and 01 December 2005 using a feature extraction tool in LPS. They were used as reference, and compared against the drainage lines extracted automatically from the DSMs using the FLOW ACCUMULATION algorithm of ArcView GIS. Prior to that, spurious depressions in the DSMs were eliminated with a FILL function to make it hydrologically correct (Murphy et al., 2008). During automatic drainage extraction, a 50 000 m<sup>2</sup> area threshold was selected in order to restrict the extraction of some first order drainages, as the corresponding reference drainages were difficult to demarcate through 3D visualisation.

We compared the drainage lines for their degree of mismatch, adapting a method of Carrara et al. (1992) developed to compare spatial discrepancy of two landslide inventory maps. Using this method, we compared the closeness of the automatically extracted drainage line with the standard reference drainage line. A buffer of 30 m around the drainage lines was calculated in GIS to prepare the area of influence (Figure 2.5). Since a 3x3 pixel window was used in the automatic drainage extraction algorithm, we used a buffer distance of 30 m (3 times the DSM resolution) on both sides of the drainage lines. An error index (EI) was calculated using the following formula.

$$EI = \frac{A_2 - (A_1 \cap A_2)}{A_1} \quad (2.5)$$

Where  $A_1$  is the area of the reference drainage buffer,  $A_2$  is the area of the drainage buffer extracted from the DSM, and  $A_1 \cap A_2$  is the common area between the two drainages. EI ranges between 0 – 1, with lower values signalling a higher degree of match of the drainage lines.

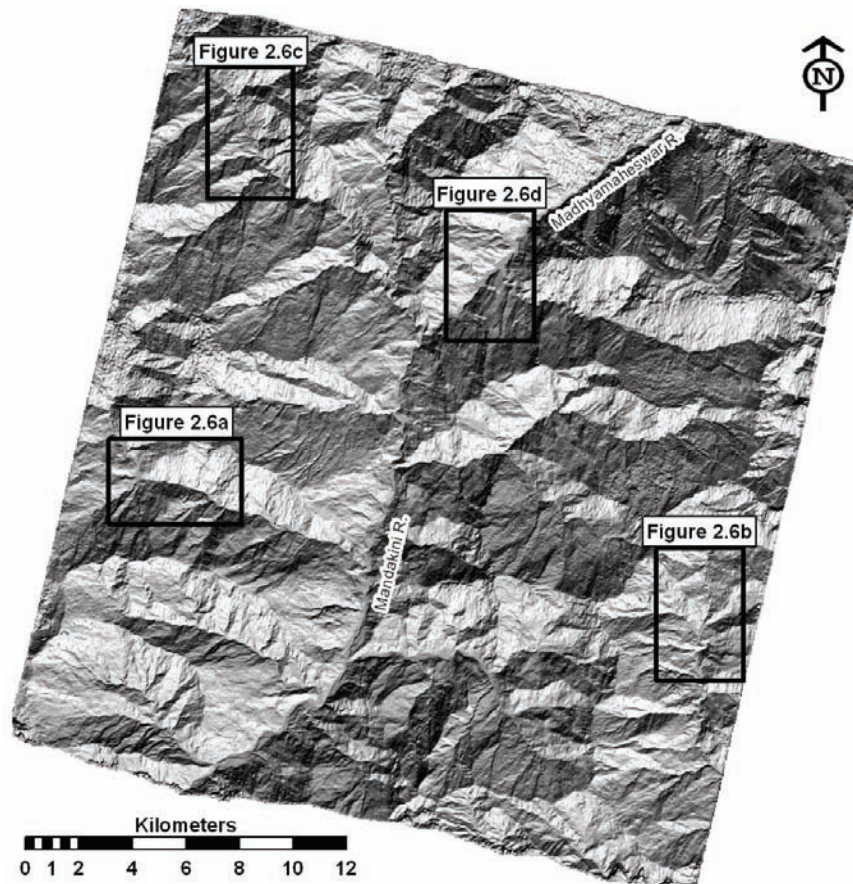
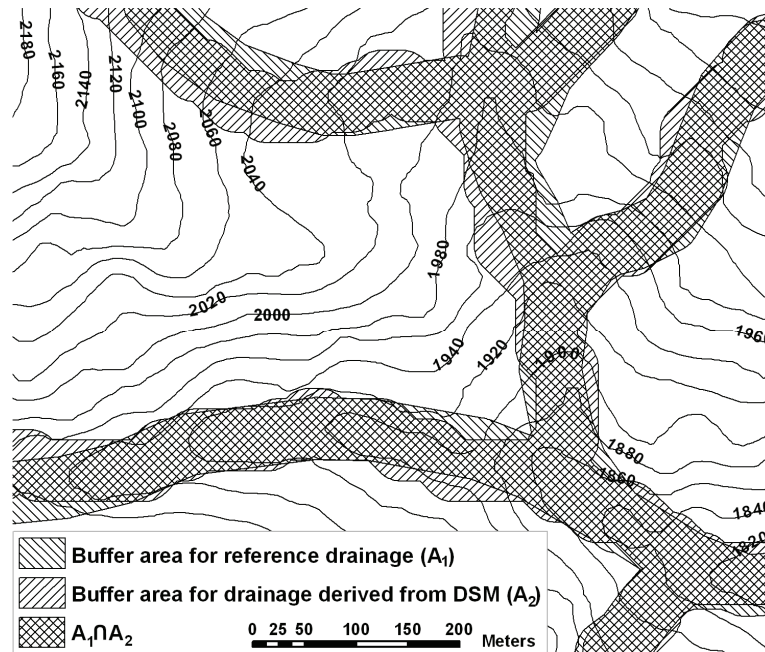


Figure 2.4: 10 m DSM extracted from the Cartosat-1 data (06 April 2006). The four boxes show the location of valleys that were analysed for the spatial accuracy assessment.

### 2.3.4 Effect of valley orientation

Although along-track stereoscopic images are increasingly used for DSM generation, similar to across-track viewing there are limitations when the DSM is generated for steep mountainous areas due to the viewing angle of the cameras. Since Cartosat-1 data are acquired in the descending mode, the PAN-Aft camera cannot view a terrain with slopes greater than  $85^\circ$  and northerly aspect, and the PAN-Fore camera cannot view a terrain with slopes greater than  $64^\circ$  and southerly aspect (Radhika et al., 2007). The relative

compression and elongation of features in the image is a function of slope of the terrain in the along-track direction of the satellite (Radhika et al., 2007). It means that in the along-track stereoscopic data this problem will predominantly occur on slopes with both south and north aspects, i.e. E-W oriented valleys, where we can expect image matching problems. Conversely, for N-S valleys, image distortion is expected to be minimal. Radhika et al. (2007) reported good image matching results for Cartosat-1 data for slopes ranging from  $-30^\circ$  (direction opposite to the satellite motion, i.e. north facing) to  $10^\circ$  (in the same direction of the satellite motion, i.e. south facing). It means that slope and orientation of the valley, with reference to the satellite track, do influence the spatial accuracy of the DSM.



**Figure 2.5:** Drainage line buffer, used for calculation of spatial accuracy. This area corresponds to the lower part of the box (figure 2.6b) shown in figure 2.4.

To evaluate this effect, an experiment was performed by considering four principal types of main valley orientation i.e. E-W, N-S, NW-SE and NE-SW. Drainage lines, an important characteristics of valleys, were used to evaluate the spatial accuracy of the DSMs. The distribution of the valleys in the study area (Figure 2.4) offers an ideal opportunity to evaluate the effect of their orientation on DSM extraction in four major directions.

## 2.4 Results

### 2.4.1 DSM Global accuracy

The vertical and planimetric accuracies of the AprCartoDSM and DecCartoDSM were estimated using 10 independent check points, resulting in vertical RMSEs for both DSMs nearly identical to the spatial resolution of the image (Table 2.2).

To verify the reliability of the DSM global accuracy values shown in table 2.2, we followed the theoretical approach developed by Aguilar et al. (2007), because of the non-Gaussian distribution of elevation residuals for this area. The two models developed by Aguilar et al. (2007) estimate the reliability of the global statistical measures as a percentage by calculating the standard deviations of  $\sigma$  and RMSE, with lower values indicating higher reliability. The models were applied to the residual dataset and the results are shown in table 2.3.

**Table 2.2:** Statistical assessment of the global accuracy of DSMs using 10 check points. X and Y show the planimetric, Z the vertical accuracy.

Variables	Statistical parameters (errors)	<i>AprCartoDEM</i> (m)	<i>DecCartoDEM</i> (m)
X	Minimum	0.02	0.02
	Maximum	1.14	1.46
	$\mu$	0.60	0.27
	RMSE	0.71	0.48
	$\sigma$	0.40	0.44
Y	Minimum	0.03	0.02
	Maximum	0.93	0.46
	$\mu$	0.46	0.15
	RMSE	0.58	0.21
	$\sigma$	0.37	0.16
Z	Minimum	0.12	0.10
	Maximum	4.98	5.80
	$\mu$	1.27	0.96
	RMSE	2.31	2.51
	$\sigma$	1.99	2.02

**Table 2.3:** Reliability of the vertical global accuracy of both the DSMs.

DSM	Reliability of $\sigma$ (%)	Reliability of RMSE (%)
<i>AprCartoDEM</i>	22.1	23.4
<i>DecCartoDEM</i>	34.2	37.5

### **2.4.2 Effect of valley orientation on DSM accuracy**

Spatial accuracy assessment of the DSMs extracted from the two Cartosat-1 datasets with high and low sun elevation angles was carried out by calculating the degree of match between the reference and automatically extracted drainage lines. Two reference drainage systems (from April and December images), when compared, showed negligible mismatch. We selected valleys for the required orientations with comparatively little topographic shadow in both datasets. It was observed that for an E-W valley, the main valley drainage lines extracted from AprCartoDSM showed significant spatial deviation from the reference drainage line (Figure 2.6a1). Surprisingly, the main valley drainage derived from DecCartoDSM showed a better match ( $EI = 0.35$ ) with the reference drainage (Figure 2.6a2) than those from AprCartoDSM ( $EI = 0.64$ ). For the remaining three types of valley orientation (N-S, NW-SE and NE-SW), no significant deviations of drainage lines were observed between both DSMs (Figures 2.6b1 and b2, c1 and c2, d1 and d2).

Steep hill slopes are the probable areas for failure of image matching in Cartosat-1 (Radhika et al., 2007). Therefore, DSM portions in those areas are more prone to error than the main valley floor. To know precisely the areas of good degree of match, we divided the drainage lines into two categories: one corresponding to the main valley (one drainage line in the central part of the valley), the other corresponding to hill slopes. The EI was calculated using equation 2.5.

### **2.4.3 Effect of shadow on DSM generation**

Shadow is a homogeneous area in the image and automatic image matching mostly fails in such areas, resulting in elevation values in these areas that are incorrect due to poor interpolation from the sparsely distributed surrounding match points. The extent of topographic shadow depends on the steepness of the terrain, valley orientation and sun elevation angle. In the area studied in this chapter, some parts with a steep slope and north aspect are under more shadow in the winter season data than the summer season. For example, the small part of the valley shown in figure 2.7 is 51% under shadow in the winter season data, compared to only 2% in the summer season data. Hence, differences in the distribution and density of match points were observed for the data of both seasons (Figure 2.7a and 2.7b). The density of match points was lower for the winter season data than the summer season data around the areas affected by shadow. A terrain profile of the area (along the transect E–F) shows significant differences in elevation (Figure 2.7c). For areas that are not under shadow the match points were

generated evenly and there was no significant difference of elevation in the two DSMs (Figure 2.7c).

## **2.5 Discussion**

DSMs for a steep mountainous area were extracted from Cartosat-1 stereo pairs of both summer and winter seasons using SAT-PP. This software proved to be robust for automatic DSM extraction due to its superior image matching algorithm (based on feature points, grid points and edges), as compared to LPS.

A high level of global accuracy was achieved due to the use of additional GCPs for refining orientation result of the RPC model (Table 2.2). It was better than previously reported for Cartosat DSMs by Ahmed et al. (2007) due to better planimetric and vertical distribution of control points used for triangulation of our datasets. No significant differences in vertical and planimetric RMSEs between the two DSMs were observed (Table 2.2). However, the reliability of global accuracy values for AprCartoDSM is better than the DecCartoDSM (Table 2.3). Reliability of global accuracy values is a function of the number of check points. For example, Aguilar et al. (2007) obtained a good reliability value of 6.3% when a sample size of 128 check points was used. The overall reliability of the two DSMs generated in this study must be considered unsatisfactory by Aguilar et al.'s (2007) measure, a result of the low number check points available. Local errors were also observed in the DecCartoDSM due to the presence of shadow (Figure 2.7c). This is due to lack of contrast in the shadow areas, which leads to absence of matched points.

Apart from the terrain steepness, orientation of valleys with respect to satellite track is another important factor in along-track stereoscopy that has a significant effect on the DSM spatial accuracy. According to Radhika et al. (2007), image matching is a function of slope along the direction of satellite track in Cartosat-1. This means that E-W valleys are problematic areas for image matching, as the variation of slope is mainly in the along-track direction. Conversely, we can expect minimum problems for image matching in N-S valleys. We found maximum EI values for the main valley and hill slope drainages along E-W oriented valleys, in comparison to the three other types of orientations (Figure 2.6). Further, in the E-W valley the spatial accuracies of the main valley drainage from both DSMs are better when

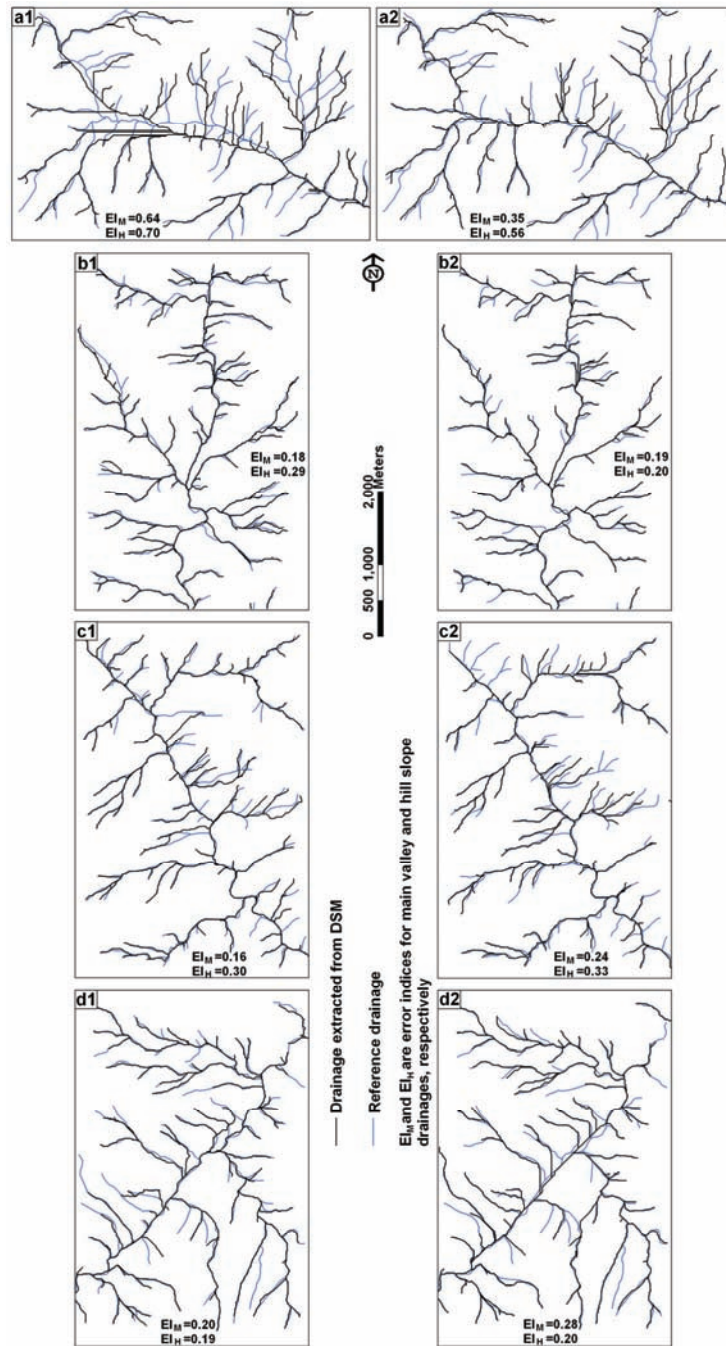


**Figure 2.6:** Drainage comparison for four types of valley orientations (E-W, N-S, NW-SE and NE-SW) with automatically derived drainage from the DSM superimposed on the manually extracted reference drainage, for the *AprCartoDSM* (a1-d1) and *DecCartoDSM* (a2-d2).

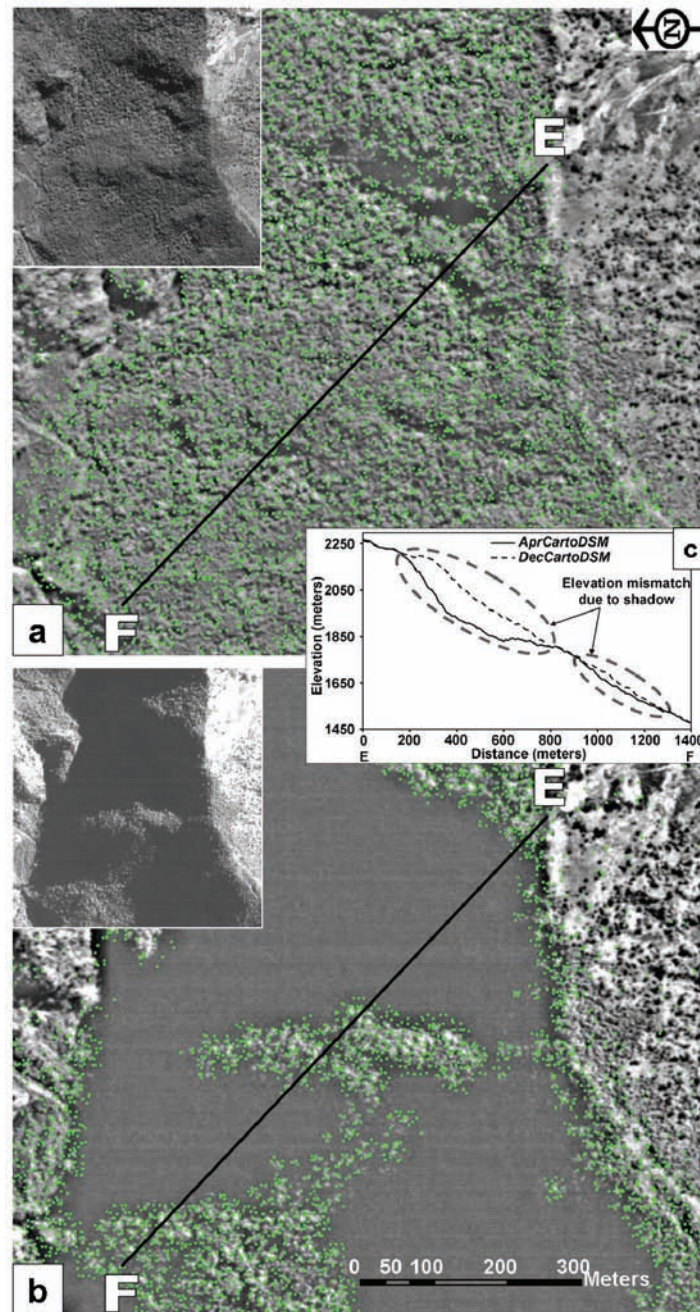


**Figure 2.7:** Difference in the distribution and density of matched points (black dots) in shadow areas from Cartosat-1 images of (a) 06 April 2006 and (b) 01 December 2005. E-F profile in (c) shows the difference of elevation in shadow affected areas. (a) and (b) have the same scale and orientation. The insets in (a) and (b) show the shadow conditions. The image contrast is reduced to highlight the distribution of points.

compared to the hill slope drainage (Figure 2.6). This difference in spatial accuracy is due to limited variation of slope along the valley floor than, as compared to high variation in the hill slopes areas. Therefore, overall lower spatial accuracy for E-W oriented valleys than for other orientations can be attributed to image matching problem.

In the Himalayas, geological structure has a strong influence on shaping the topography. The valleys and ridge lines mostly follow geological structure. We observed that the drainage lines in an E-W valley were better matched on hill slopes facing north than the drainage lines on the hill slopes facing south (Figure 2.6a1 and a2). This is due to the typical topography of this area as shown in figure 2.8, where hill slopes facing north are gentle and hill slopes facing south are steep.

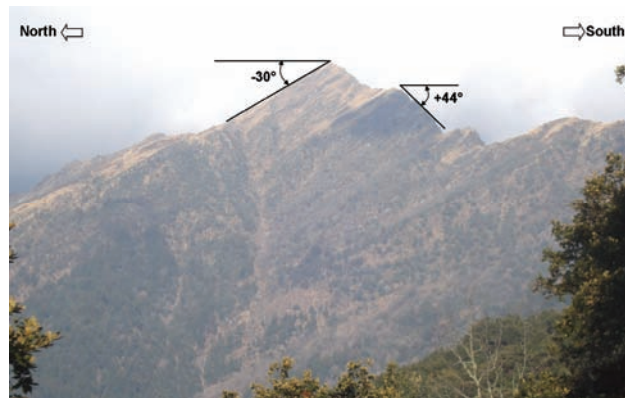


**Figure 2.8:** Field photograph showing typical topography of the study area with gentle north facing dipslopes and steep south facing faceslopes. The signs of topographic slope are with reference to the satellite motion.

The spatial accuracy of the main valley and hill slope drainages extracted from the DecCartoDSM are 45% and 20% higher than the AprCartoDSM for E-W valleys, respectively. This is a result of a higher number of match points generated in the valley floor and hill slope portions of the E-W valleys for winter season data than the summer season data. When analysing the pixel information we found a good local contrast in the winter image compared to the summer image (Figure 2.9), meaning that radiometric variation is better in the winter than the summer season data, even though land cover remains the same. The image shows a higher range and standard deviation in the winter than the summer season data (Figure 2.9), and explains the presence of more match points in the former, as most image matching algorithm rely on strong local contrast (e.g. Kerle, 2002). Better radiometric variation in the winter season data may be due to proper illumination of the hill slopes, particularly those facing south, by the sun with a low elevation angle.

Although shadow is seen in the north facing slope of the winter season image (Figure 2.9a), these are small pockets (ellipses in Figure 2.9a), embedded in less intensively but sufficiently illuminated areas for SAT-PP to identify match points, unlike in the area shown in figure 2.7b, where the DN value range within the shadow areas was too low, and the shadow area too extensive, resulting in blanket interpolation.

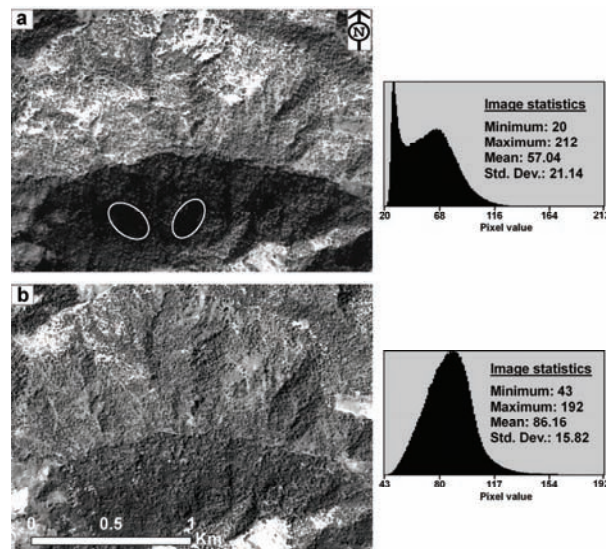


**Figure 2.9:** Cartosat-1 PAN-Aft image showing better local contrast in the winter season image (a) than the summer season image (b), for an E-W valley. This area corresponds to the box (figure 2.6a) in figure 2.4. Ellipses inside figure (a) show small shadow areas.

## 2.6 Conclusion

In this chapter we generated two DSMs using high and low sun elevation angle Cartosat-1 data for a steep mountainous area in the Himalayas, and assessed the advantages and limitations of these stereoscopic images as a source of elevation data. High resolution along-track stereoscopic data, such as from Cartosat-1, have become a major source for DSM generation. GCPs were used to refine the orientation result of the RPC model of Cartosat-1 data and resulted in a DSM with a vertical RMSE equivalent to the spatial resolution of the images, although this also reflects a relatively low number of GCPs largely confined to less steep areas that we would expect to be more accurate in the resulting DSM. The RMSEs were found to be comparable for AprCartoDSM and DecCartoDSM with 23.4% and 37.5% reliability, respectively. This is lower than previously reported results (e.g. Aguilar et al., 2007; Li, 1991), due to the lower number of independent check points

available. However, local errors exist in the DSM in shadow areas that result from low sun elevation.

Apart from the metric accuracy, spatial accuracy of the DSMs was estimated by comparing automatically extracted drainage lines from the DSM with reference drainage information. We found that valley orientation has a significant effect on the planimetric as well as vertical accuracy of a DSM extracted from along-track stereoscopic data. The minimum and maximum spatial accuracies were obtained for E-W and N-S oriented valleys, respectively. This information is of use for hydrologists and geomorphologists when anticipating potential error sources, since the inaccuracies primarily affect commonly used DSM derivatives.

Although it is commonly assumed that a high sun elevation angle (less topographic shadow) is favourable for automatic DSM generation, we found that for E-W oriented valleys the DSM extracted from low sun elevation angle data provides better spatial accuracy than the DSM from data captured under a high sun elevation angle, if the actual valley is sunlit in both datasets. This effect can be seen in the area shown in figure 2.7b, where extensive shadow resulted in blanket interpolation, vs. the slope shown in figure 2.9a where smaller shadow pockets led to spatially confined DSM errors. However, the effect of illumination needs to be studied in more detail.

Both results are important for DEM users as they show that the sun elevation angle and local valley orientation can have a pronounced effect on the accuracy of a DSM, yet the consideration of these parameters is typically neglected. Our method of spatial accuracy assessment is simple and can be adopted by a DEM user as it does not require a reference DEM, which in most cases is unavailable. It will be interesting to evaluate the effect of valley orientation and sun elevation angle on the spatial accuracy of DSMs derived from other along-track data sources with similar sensor configuration, such as ALOS-PRISM and SPOT-5 HRS.

## ***Acknowledgements***

For the DGPS survey we are thankful to Mr. Raghu Venkataraman, GM, NRSC for his support, and to Mr. Anantha Padmanabha, Mr. M. Mohan Naidu and Mr. N. Satyanarayana for the field survey. We are indebted to Prof. Armin Gruen and Dr. Devrim Akca, ETH Zurich, for providing the SAT-PP software and support for processing the stereo data.

## Chapter 3: Volumetric analysis of landslides<sup>\*</sup>

In this chapter we assess the suitability of a DSM derived from Cartosat-1 to quantify large-scale geomorphological changes. Landslide volume was estimated by elevation change analysis of pre- and post-event DEMs. Depletion and accumulation volumes estimated through this analysis can form an important part of the landslide inventory information necessary for the landslide hazard studies.

### 3.1 Introduction

Large scale anthropogenic landscape changes, such as those caused by mining and urban waste disposal, and those of natural origin, such as landslides and glacial melting, are primary topographic change drivers (Kerle, 2002; Martha et al., 2010a; Surazakov and Aizen, 2006; van Westen and Lulie Getahun, 2003). Small or subtle changes are readily quantified using techniques such as radar interferometry or, where available, laser scanning data. Volumetric analysis has the potential to monitor and quantify also large-scale events, and can be useful in implementing proper risk management strategies or to enforce environmental regulations. For example, reliable information on material volume can help government agencies to estimate the value of contract and number of days required to clear the debris from transportation routes in case of a landslide (Jaiswal and van Westen, 2009), or the amount of material required to reclaim the land in case of open-pit mining as a mandatory requirement under a mine control act (Townsend et al., 2009). In the past such assessments have typically been done through time-consuming field measurements, although those tend to suffer from difficulties in establishing accurate baseline topography. Photogrammetric techniques have been increasingly used because of their capability to rapidly reconstruct the 3D topography from aerial photographs (Dewitte and Demoulin, 2005; Käab, 2002; Kerle, 2002) and, provided such data exist for different time periods, allow objective change detection.

More recently, civilian Earth observation satellites have offered stereoscopic data with sufficient spatial resolution to allow aerial data to be effectively replaced (Martha et al., 2010c; Radhika et al., 2007; Tsutsui et al., 2007; Zhang and Gruen, 2006). In addition, new generation satellites such as Cartosat-1 have considerable advantages over airborne stereo imagery, due to their high periodicity, synoptic view, high data quality, relatively low cost,

---

<sup>\*</sup> This chapter is based on the article: Martha, T.R., Kerle, N., Jetten, V.G., van Westen, C.J. and Kumar, K.V. (2010) Landslide volumetric analysis using cartosat - 1 - derived DEMs. *IEEE Geoscience and Remote Sensing Letters*, 7 (3), 582-586.

and quick extraction of DEM using RFM (Baltsavias et al., 2008; Martha et al., 2010c). Cartosat-1, launched by the ISRO in 2005, is a global mission planned for cartographic mapping, urban studies and disaster management (NRSC, 2006). Specifications of Cartosat-1 are provided in section 2.1. Data from Cartosat-1 are 10 bits and provided with RPCs for photogrammetric processing and extraction of 3D information using RFM. In principle, therefore, Cartosat-1 data are well suited for fast and accurate 3D surface reconstruction, although in practice there can be potential problems due to shadow, occlusion and steep slopes depending on the terrain (Baltsavias et al., 2008; Martha et al., 2010c). With Cartosat-1 acquiring along-track data, image matching is less problematic than for across-track images due to reduced radiometric variation between the two images of a stereo pair (Radhika et al., 2007); however, factors such as valley orientation, sun elevation angle and poor texture frequently hinder accurate extraction of elevation data (Martha et al., 2010c). We addressed some of these problems through SAT-PP photogrammetric software, especially developed for high resolution satellite data, and which previously demonstrated the ability to process such stereoscopic data due to its superior image matching algorithm (Zhang and Gruen, 2006), compared to other COTS software types (Martha et al., 2010c).

In this chapter we tested the utility of Cartosat-1 data for quantitative volume analysis based on cut and fill assessment, an established method for estimating the volume of large landslides (Chen et al., 2005; Kerle, 2002; Tsutsui et al., 2007). We used the 2007 Salna landslide in the Indian Himalayas as a test case, which offers a great challenge to automatic DEM extraction due to steep slopes and large topographic shadows (Martha et al., 2010c). Previous studies have demonstrated the utility of DEMs extracted from satellite data for monitoring topographic changes due to glacial melting (Kääb, 2002; Surazakov and Aizen, 2006; Tsutsui et al., 2007), landslides (Tsutsui et al., 2007), and rehabilitation planning of coal mining areas (Loczy et al., 2007). The purpose of this chapter is to assess if Cartosat-1 derived DEMs are sufficiently accurate to quantify such changes and to monitor compliance with related legislation.

### **3.1.1 Landslide volume estimation**

Landslides are major mass wasting processes and landscape building factors in mountainous terrains. They are primarily triggered by seismic activity, rainfall or road construction, and cause enormous destruction to property and lives in those areas. Some of the major earthquakes that have created several deep-seated landslides in the recent past are the Kashmir earthquake in India and Pakistan in October 2005 and the Sichuan earthquake in China in

May 2008. Apart from direct damage landslides also contribute sediments to river systems and create siltation problems in reservoirs, reducing their capacity for hydro power generation. They also have the potential to create artificial lakes by blocking river courses, thus generating potential flash floods in downstream areas (Dunning et al., 2007; Wang et al., 2009). Knowledge of failure volumes is also critical for more accurate understanding of the landslide process (e.g. Scott et al., 2005) and the preparation of susceptibility maps, which show potential areas of future landslide occurrences. For example, landslide susceptibility maps will be more accurate if volume, instead of area of the landslide, is used to calculate weights of the terrain parameters. Okura et al. (2003) showed how the volume of a landslide directly affects its travel distance, while Dai and Lee (2001) demonstrated that frequency-volume relationships can be used to predict rainfall-induced landslides.

Traditionally, failure volumes have been estimated by measuring landslide dimensions (length, width and depth) on the ground, using assumptions about the shape of the landslide (Cruden and Varnes, 1996). Such ground-based methods may provide accurate volume figures, though are time-consuming, error-prone and at times not possible due to terrain inaccessibility. Pre- and post-failure topographic maps can also be used for calculating the landslide volume using change detection techniques. However, topographic maps are typically not updated immediately after the event, or lack sufficient accuracy (Kerle, 2002). In order to overcome these problems, multi-temporal aerial photographs were initially used to estimate landslide extents and volumes (Dewitte and Demoulin, 2005; van Westen and Lulie Getahun, 2003). Dewitte and Demoulin (2005) generated DEMs with a high accuracy from aerial photographs using photogrammetric techniques to estimate the volume of 13 deep-seated landslides in the Flemish Ardennes. However, with advancements in image matching techniques and increasing availability of high resolution stereoscopic satellite data, quantitative studies on landform changes using DEMs based on satellite data have become a viable option (Chandler, 1999). Recently, Tsutsui *et al.* (2007) used SPOT-5 stereoscopic data and generated five meter DEMs to calculate the volume of landslides triggered due to an earthquake and a cyclone in Japan and Taiwan, respectively. However, their estimated volume showed a mismatch with the reference volume due to inaccuracies in the DEM resulting from poor texture in 8 bits SPOT images and topographic shadow. The problems of poor texture can be reduced by the use of 11 bits images from IKONOS or QuickBird (Zhang and Gruen, 2006). However, their low swath width and high cost render those sensors impractical for routine volumetric analysis. Moreover, pre-failure images, essential for volume estimation are mostly not available

from these satellites. Kerle (2002) and Scott *et al.* (2005) showed how lack of knowledge of pre-failure topography and limited access to the site led to a ground-based volume underestimation of the 1998 flank collapse at Casita volcano, Nicaragua, of almost an order of magnitude eight.

## **3.2 Area and data analysis**

### **3.2.1 Test area**

The test area is located in one of the landslide prone areas in the Himalayas. Its centre co-ordinates are 30° 23' 38" N and 79° 12' 42" E. It is located in the Nagol Gad (River) sub-catchment in the High Himalayas in the Uttarakhand state of India (Figure 3.1). Nagol Gad is a part of Alaknanda catchment, which witnessed several major co-seismic landslides during the Chamoli earthquake in March 1999 and it lies very close to the Main Central Thrust (Barnard *et al.*, 2001). Rocks such as banded quartzite at the crown, and quartzite inter-bedded with mica schist at the toe of the landslide, belonging to Proterozoic era are exposed in this area. However, the landslide investigated for this volumetric analysis was triggered by heavy rainfall in July 2007. It occurred near the Salna village in the Chamoli district of Uttarakhand state. The landslide-affected area is completely exposed to sun in both pre- and post-landslide images (Figure 3.2a and 3.2b). The general topography is steep, with slopes ranging from 18° to 63°. The elevations of the crown and tip of the landslide are 1636 m and 1261 m, respectively. The Salna landslide is a translational rock slide, which means that the failure has taken place along a planar surface of rupture. Its length (crown to tip) is 530 m, with a maximum width at the centre of the landslide of 260 m (Figure 3.1a). Although there were no fatalities, the major road connecting the surrounding area with Chamoli town was blocked for several months, causing hardship to local population and damage to the regional economy.

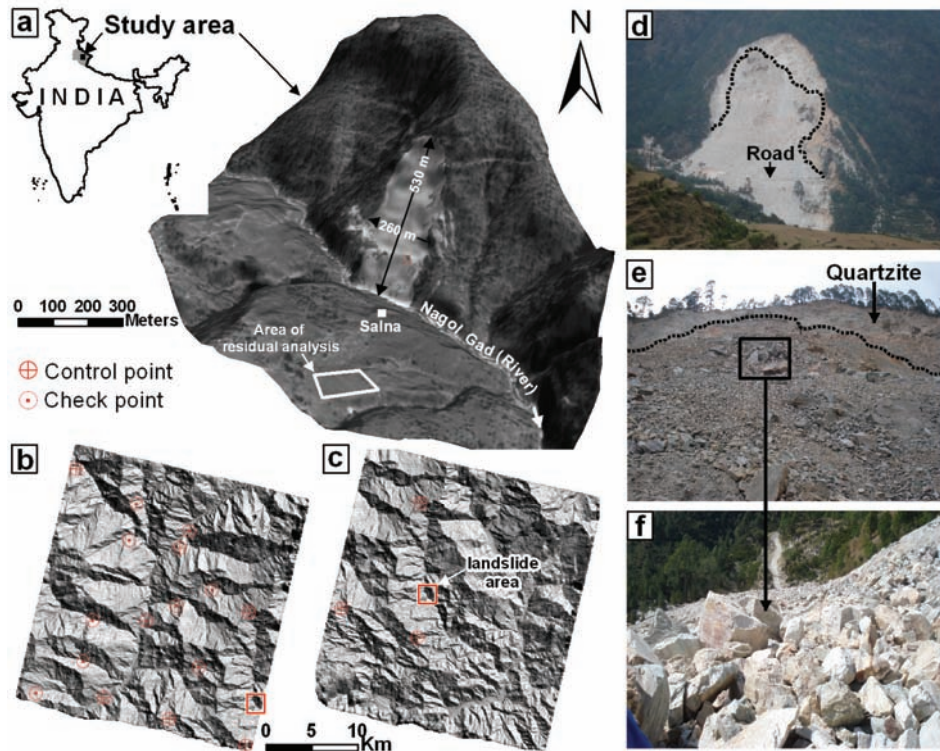


**Figure 3.1:** Location map of the Salna landslide. (a) 3D perspective view of Salna landslide with the Cartosat-1 image draped over a DEM, (b) and (c) pre- and post-landslide DEM, respectively, showing distribution of control and check points, (d) field photograph showing synoptic view of the landslide, (e) view of the quartzite bedrock exposed in the scarp (the area above the black dotted line), and a part of the zone of accumulation as seen from the temporarily constructed road, and (f) large angular boulders with large voids in between, signaling a volume increase during deposition.

### 3.2.2 DSM generation

Two sets of stereoscopic Cartosat-1 data, acquired on 06 April 2006 (pre-landslide) and 16 December 2007 (post-landslide), were processed using SAT-PP software. Compared to established COTS photogrammetric packages, SAT-PP has an improved image matching algorithm based on combined matching results of feature points, grid points and edges, leading to superior results also in steep terrain (Martha et al., 2010c; Zhang and Gruen, 2006). DSMs with 10 m grid size were generated using RPCs determined from the RFM and provided by the data vendor. RFM is a generic sensor model and is used as an alternative to physical sensor models for block orientation of the -

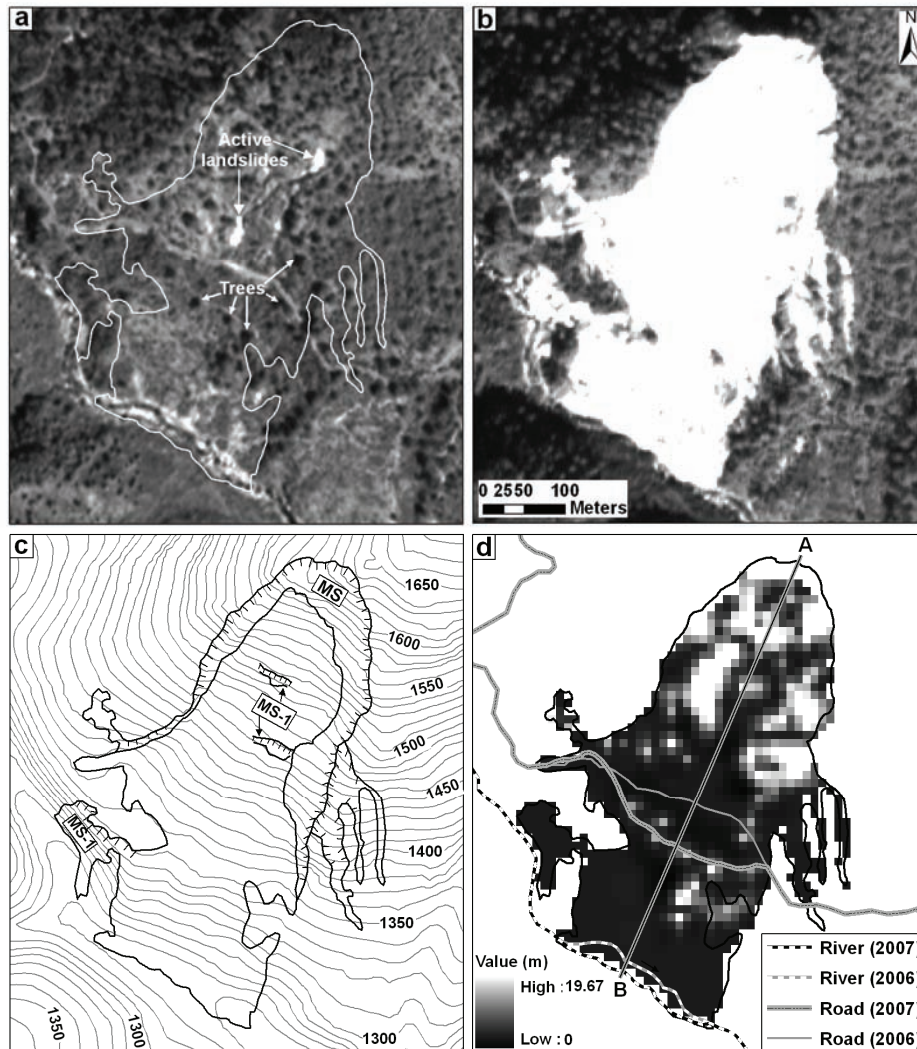


**Figure 3.2:** Salna landslide. (a) Cartosat-1 orthoimage of 06 April 2006 showing the pre-landslide area outlined in white. It was a distressed zone with presence of two minor landslides acting as a precursor to the main event, (b) Cartosat-1 orthoimage of 16 December 2007 showing the landslide that occurred in July 2007, (c) post-landslide map showing main scarp (MS) and minor scarps (MS-1), and (d) non uniform vegetation height surface created by the interpolation of heights measured from 74 trees, and post-landslide effects. The new road now has a convex outward shape, and the original river was pushed outward due to the deposition of debris at the foothill region. Profile along A-B is shown in figure 3.3.

stereo-image pair. RPCs are terrain independent, and require refinement with GCPs at block level to increase the absolute geo-location accuracy of DSMs (Baltsavias et al., 2008). Therefore, we used six GCPs with good planimetric and vertical distribution to refine the orientation result of the RFM (Figure

3.1b) (Baltsavias et al., 2008). The GCPs were collected in a DGPS survey using a dual frequency (L1 and L2) Leica 520 receiver. The standard deviation of the errors of elevation, longitude and latitude of the points surveyed range between 0.10 m to 0.46 m, 0.04 m to 0.15 m and 0.04 m to 0.21 m, respectively.

The necessity of high DEM accuracy for an elevation change analysis has been emphasized by previous researchers (Kerle, 2002; Van Niel et al., 2008). Kerle (2002) showed how especially the combination of errors in the vertical accuracy of photogrammetrically derived DSMs and the landslide thickness typically being the smallest dimension readily combine to substantial uncertainty. Errors in elevation difference can either result from mis-registration of the pre- and post-event DEMs (Van Niel et al., 2008), or from low spatial accuracy resulting from sun illumination and valley orientation with reference to the satellite track (Martha et al., 2010c). Along-track satellite data such as from Cartosat-1 offer improved results of image matching due to reduced radiometric variation between images of a stereo pair (Radhika et al., 2007). However, distortion of feature geometry due to steep terrain and variable viewing angle of Cartosat-1 has compromised some of these advantages. This problem can be overcome using SAT-PP software, which relies on a robust point, grid and feature based image matching technique (Zhang and Gruen, 2006). Topographic shadow in mountainous area is another problem that creates inaccuracies in a DEM. SAT-PP is also capable of generating the adequate number of match points required for an accurate DSM generation for relatively small shadow areas; however, large shadows still remain a problem (Martha et al., 2010c; Zhang and Gruen, 2006).

In chapter 2 we assessed the absolute accuracy of the pre-landslide DEM using 10 independent check points obtained from the DGPS survey, resulting in vertical and planimetric RMSE as 2.31 m and < one meter, respectively (Martha et al., 2010c). In addition, spatial accuracy of the pre-landslide DEM was estimated by a drainage line comparison method, wherein drainage lines were used as a proxy to estimate the error due to spatial auto-correlation in the absence of a very accurate reference DEM (Martha et al., 2010c). Subsequently, refinement of the orientation result of post-landslide RFM was done by using three GCPs common in the overlap area (Figure 3.1c). Thus both DSMs were brought into the same spatial framework. However, to verify the vertical and co-registration accuracies of two DSMs, a residual analysis was carried out between the two DSMs in an area adjacent to the landslide (Figure 3.1a). This area is unvegetated and no morphological changes have occurred during the observation period. The residual analysis showed a

vertical mean and standard deviation of errors of 0.11 m and 0.06 m, and corresponding planimetric errors of 0.09 m and 0.05 m, respectively. The low errors indicate that both DSMs are co-registered properly and have a good vertical accuracy relative to each other. Therefore, any change in height can be attributed to morphological changes, such as due to landslides, allowing volumes to be calculated.

### **3.2.3 Volumetric analysis**

As volume calculation must be based on the actual pre- and post-landslide terrain surfaces, vegetation that may have covered the area before failure, or that was possibly retained during the landslide, must be corrected for, as it forms part of the photogrammetric surfaces. Accurate estimation of vegetation height has previously been shown to be challenging (Kerle, 2002). In the area of the Salna landslide mainly chir trees, a pine variety typical in the Himalayas, are found. The height of some of the uprooted and standing trees (in the adjacent area) was measured on the ground. This height, in conjunction with the height of the trees measured through manual interpretation of stereo images was used to create a non-uniform vegetation height surface (Figure 3.2d). A total of 74 trees (7 on the ground and 67 in the stereo image) with a mean height of 11.87 m (minimum 4.29 m and maximum 19.67 m) were used for the creation of the non-uniform vegetation height surface. Subsequently, this surface was subtracted from the automatically generated pre-failure DSM, and a vegetation-corrected DTM was created. Vegetation correction was not required for the post-failure DSM since trees were completely uprooted. After vegetation correction the area and volume of the Salna landslide were calculated by subtracting the post-landslide DTM from the pre-landslide DTM, using the cut and fill operation in ArcGIS. This operation summarizes areas and volumes of change using surfaces of a given location at two different time periods, and identifies regions of surface material removal, addition and no change.

## **3.3 Results and discussion**

The Salna landslide was triggered due to excessive rainfall, and the pre-landslide Cartosat-1 image already showed the existence of small active landslides in the area (Figure 3.2a). The slope length of the main scarp below the crown of the landslide is approximately 50 m (Figure 3.2c). The landslide completely buried the road with material displaced from the crown part. The new road (Figure 3.1d), which was temporarily constructed to allow traffic to resume is now positioned 62 m outward from its previous location, and the shape of the road is convex outward (Figure 3.2d), indicating the deposition of a large amount of material and development of a hummocky structure. Similarly, the Nagol Gad (River) was pushed 25 m to its right bank by the

landslide (Figure 3.2d). Fortunately, no damming of the river occurred due to the landslide. Debris mainly composed of boulders of banded quartzite is seen in the zone of accumulation (Figures 3.1e and 3.1f).

From the profile (Figure 3.3) and from the extent of the volume gain (Figure 3.4b) it is clear that the area of the zone of depletion is smaller than the area of the zone of accumulation, indicating expansion, or bulking, of material after the displacement due to fragmentation of the bed rock. The elevation change map shows that maximum deposition of material has taken place at a height of approximately 1420 m (Figure 3.4a). The cut and fill volumes, i.e. the volumes of depleted and accumulated material, were estimated as  $0.55 \times 10^6 \text{ m}^3$  and  $1.43 \times 10^6 \text{ m}^3$ , respectively (Table 3.1).

**Table 3.1:** Quantitative comparison of volume.

DEM type	Volume loss ( $10^6 \text{ m}^3$ )		Volume gain ( $10^6 \text{ m}^3$ )		Bulking
	Before vegetation correction	After vegetation correction	Before vegetation correction	After vegetation correction	
DEM (with GCP)	0.77	0.55	1.34	1.43	2.60
DEM (without GCP)	0.76	0.54	1.31	1.41	2.61
DTM (spot height)		0.67		1.26	1.88

So far we have estimated the landslide volume from DEMs derived with the use of additional GCPs. However, the need for field-measured control points, a strictly required in traditional photogrammetry, severely undermines the utility of satellite data for rapid and independent post-landslide assessment. To assess the dependency of accurate volume estimation on additional field-mapped GCPs, we also created DEMs only with the RPCs provided with Cartosat-1 data. Such a step is reasonable, as additional GCPs primarily affect the absolute accuracy of the DEM, and less the relative elevation value distribution. Nevertheless, the effect of integrating two such relative surfaces for accurate change assessment was unknown. Table 3.1 shows that the estimated volume values based on RPC-only DEMs fall to within 1–3% of the GCP-supported DEM values, indicating that the volume figures are less sensitive to GCPs support than expected.

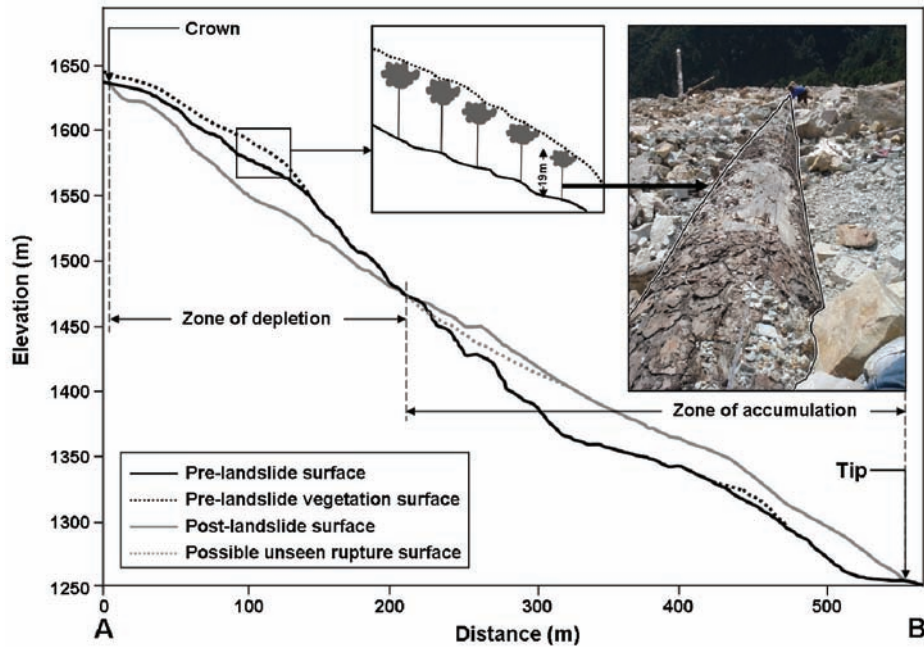


**Figure 3.3:** Pre- and post-failure surface profile from the crown to tip of the landslide. Grey dotted line shows the possible extension of surface of rupture over which debris is temporarily deposited. Height of some of the chir pine trees were measured on the ground (e.g. an uprooted tree in the inset photograph).

The bulking factor (ratio of volume gain to volume loss) of 2.60 (Table 3.1) is comparable to previously reported values for similar events, such as the bulking following the flank collapse of Casita volcano, Nicaragua studied by Scott et al. (2005). The bulking of Salna landslide is due to two factors: 1) incomplete separation of loss area from gain area, due to which material is still lying at the bottom of the hidden rupture surface (van Westen and Lulie Getahun, 2003), which is impossible to be reconstructed from post-failure stereo data (Figure 3.3), and 2) poor sorting of large and angular broken quartzite rock fragments (Figure 3.1f) created by the translational rock slide, leading to a possible overestimation of the gain volume. However, the estimated volume can be considered realistic, since the post-landslide surface was generated shortly (approximately five months) after the occurrence of the landslide, suggesting limited deposition material loss due to surface erosion and further remobilization.

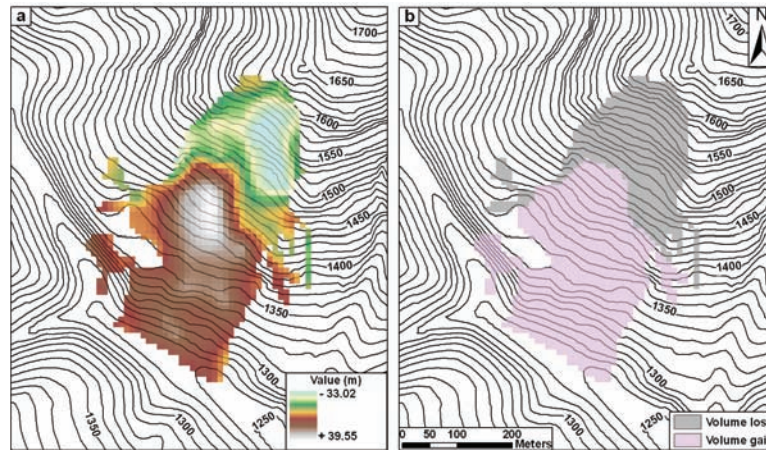


**Figure 3.4:** Volumetric analysis of the Salna landslide. (a) elevation difference due to landslide with negative values showing lowering of surface and positive values showing rising of the surface after the event, and (b) extent of the volume loss and volume gain, which corresponds to the zones of depletion and accumulation, respectively.

### 3.3.1 Accuracy assessment of volume

The global accuracy of the DSM has been verified by independent check points, although previous studies have shown that digital photogrammetry with low global errors can still lead to substantial local errors, especially in areas of low contrast (e.g. uniform vegetation, landslide failure flanks). Volume accuracy assessment in such small, local areas is thus a challenge, particularly with only limited reference data, i.e. without a dense network of ground check points for both pre- and post-landslide affected area. Due to the absence of detailed verification data for the relatively small landslide area (i.e. part of the large DEMs for which accuracy has been checked), we manually extracted spot heights (Kerle, 2002), identifying 85 and 129 points from the pre- and post-failure datasets, respectively, using StereoAnalyst in ERDAS Imagine, and compared the volume obtained from spot height data with the automatic results (Table 3.1). The number of points is sufficient for a reliable comparison since they were collected with particular emphasis on break-in-slope and scarp areas, leading to a surface that models the actual failure area well. Spot heights from the pre-failure image were collected by selectively measuring ground elevations in between trees, thus eliminating the need for further vegetation correction, and directly on the failure and deposition surfaces in the post-failure image. These points were interpolated using the TOPOGRID algorithm in ArcGIS to derive reference DTMs (Wise, 2007).

### **3.4 Conclusion**

Updated elevation data are essential for identifying areas of large-scale topographic changes for disaster management or enforcement of environmental legislation. The purpose of this study was to assess the potential of a new generation of space-borne sensors to provide DEMs for the quantification of landscape changes. In this study, DSMs with 10 m grid size corresponding to two different time periods, generated from Cartosat-1 data using digital photogrammetric methods, were used to quantify large-scale topographic changes resulting from a landslide. Following photogrammetric conventions, we generated DSMs with a grid size equivalent to 3–4 times of the ground sampling distance. With some data types, such as from SPOT-5, higher resolutions can be achieved, for example the 2.5 m resolution DEMs produced by Tsutsui et al. (2007), using super resolution processing (Latry and Rouge, 2003). Interestingly, the previously reported requirement for additional GCPs (Baltsavias et al., 2008) was found to be of lesser importance, allowing us to create surfaces with comparable relative accuracy also without such field-based measurements. This requires actual co-registration of pre- and post-failure DSMs rather than use of absolute coordinates. This means that RPCs alone are sufficient for the estimation of volume, thus freeing rapid post-failure volume assessment entirely from field data requirements, although refinement of the RFM orientation result is required to improve the absolute geo-location accuracy necessary for cartographic applications. Knowledge on pre-failure topography is crucial for accurate estimation of volume (Kerle, 2002). Cartosat-1 was launched in 2005, and its data were systematically acquired, providing substantial archives of images for major parts of the world. Availability of post-failure datasets from Cartosat-1 shortly after the event then enabled us to do rapid volume estimation. The cut and fill volumes derived from automatic DEMs showed reasonably good match with the reference volume derived from DEMs generated using manually extracted spot height data. This indicates that a 10 m DSM from Cartosat-1 data can be effectively used for large scale elevation change and volumetric analysis such as for a deep-seated landslide. The information on landslide volume can effectively be used to establish magnitude-frequency relationship for quantitative estimation of landslide hazard. However, the volume values calculated based on manually extracted spot heights show deviations of about +18% and -12% for the volume loss and gain areas, respectively, resulting also in a bulking factor that is 27% lower than based on automatic DEMs with GCPs. These deviations of volume values can be attributed to the steep slope (51°) near the crown of the landslide, where automatically generated DEMs are prone to error (Tsutsui et al., 2007).

This study showed that Cartosat-1 data have the potential to derive volume information critical for disaster assessment, in principle without any additional GPS field measurement, provided that any present vegetation artifacts are removed from the DSMs used in the change assessment. It must also be noted that, with landslide thickness, i.e.  $z$ , typically being the smallest dimension, elevation errors resulting from photogrammetric artifacts or inaccurate DSM-to-DTM correction will have a correspondingly large consequence on volume calculations. Quantitative estimation of similar large-scale changes in the landscape, e.g. due to open-pit mining and urban waste disposal, although not shown in this study, can in principle also be done with Cartosat-1 derived DSMs since they require multi-temporal DEMs similar to the ones used in this study.

### ***Acknowledgements***

We are indebted to Prof. A. Gruen and Dr. D. Akca, ETH Zurich, for providing the SAT-PP software and guidance for processing the stereo data.



## Chapter 4: Characterisation and detection of landslides\*

In this chapter the use of a combination of spectral, shape and contextual information to detect landslides is discussed. This information was derived from multispectral data, DTMs and their derivatives. It uses objects derived from the segmentation of a multispectral image as classifying units for object-oriented analysis. Objects recognised as landslides were subsequently classified based on material type and movement.

### 4.1 Introduction

Landslides are a major natural hazard, causing significant damage to properties, lives and engineering projects in all mountainous areas in the world. Landslide hazard and risk management begins with comprehensive landslide detection/mapping, which serves as a basis to understand their spatial and temporal occurrences (Brardinoni et al., 2003; Carrara and Merenda, 1976; Guzzetti et al., 2000). Detection of landslides includes recognition and classification (Mantovani et al., 1996), frequently done using the systematic classification of landslides based on type of material and type of movement proposed by Varnes (1978). In Varnes' classification, the types of material are rock, debris and earth, with falls, topples, slides, spreads and flows constituting movement types (Cruden and Varnes, 1996). The classification proposed by Varnes, and consistent with the UNESCO Working Party on the World Landslide Inventory (UNESCO-WP/WLI, 1993a), is essentially a field based method, conceptualised and illustrated using block diagrams, without reference to their surrounding morphometry and contextual relationship. However, Earth observation data are increasingly used for landslide mapping, with automatic methods being preferable over manual approaches for obtaining quicker results over large area, whereby the use of spectral, spatial, morphometric and contextual properties is essential to their success (Barlow et al., 2006; Borghuis et al., 2007). A comprehensive characterisation of landslides from an automatic detection perspective is required for the extraction of fast and accurate results that will help decision makers in implementing disaster management strategies.

---

\* This chapter is based on the articles: Martha, T.R., Kerle, N., Jetten, V.G., van Westen, C.J. and Kumar, K.V. (2010) Characterising spectral, spatial and morphometric properties of landslides for semi - automatic detection using object - oriented methods. *Geomorphology*, 116 (1-2), 24-36.

Martha, T.R. and Kerle, N. (2010) The potential of object - based and cognitive methods for rapid detection and characterisation of landslides. In: 6th International Symposium on Geo-information for Disaster Management (Gi4DM), 2-4 February 2010, Torino, Italy (In CDROM).

Visual interpretation of aerial photographs, combined with field investigations, remained the major source for landslide inventory map preparation until recently (Casson et al., 2003; Kääh, 2002; van Westen and Lulie Getahun, 2003). Although aerial photographs accurately depict details of a landslide, they are often not available in a timely manner for the majority of landslide prone areas in the world. Satellite imagery has become an alternative data source since it allows a more economic assessment of larger landslide affected areas, as well as a synoptic appreciation of the context within which landslides occur, especially in terms of land cover dynamics. Limited initially by low spatial resolution, early studies focused on pure detection of large landslides. However, recent studies have increasingly made use of very high resolution imagery (e.g. QuickBird, Ikonos, WorldView-1, Cartosat-1 and 2, SPOT-5 and ALOS-PRISM) for landslide mapping, and the number of operational sensors with similar characteristics is growing year by year (van Westen et al., 2008). Other remote sensing approaches of landslide inventory mapping, though infrequent, include shaded relief images produced from LiDAR and Synthetic Aperture Radar (SAR) interferometry based DEMs (Singhroy et al., 1998; van Den Eeckhaut et al., 2007).

Preparation of landslide inventory maps using automatic methods has been attempted by previous researchers. Borghuis et al. (2007) showed how unsupervised classification could detect 63% of all landslides mapped manually. Other familiar automatic methods of landslide mapping are change detection and image fusion. Nichol and Wong (2005a) showed the use of change detection technique to successfully differentiate landslides from spectrally similar features such as bare rock and soil. However, the automatic methods described above are pixel based methods, and pixels are ill-suited to represent a geomorphic process such as a landslide. Therefore, the output gives 'salt and pepper' appearance, and are mostly not verifiable on the ground. These methods also rely only on the spectral signature, a property not unique for landslides. In addition to spectral signature, landslide diagnostic features can include vegetation, slope angle, slope morphology, drainage, tension cracks, presence of man-made features such as retaining walls, or artificial surface drainage. Previous researchers have attempted to quantify some of these landslide diagnostic features. Pike (1988) calculated the geometric signature from a DEM for a set of topographic variables that separates a landslide from its surroundings. Similarly, Iwahashi and Pike (2007) used slope gradient, terrain texture and local convexity derived from a DEM for automatic classification of topography. Previous works have also shown that an integration of remote sensing data and DEM derivatives produces better result than the standalone approach (Florinsky, 1998;

McDermid and Franklin, 1994). OOA, a platform for integration of different types of data (spectral, elevation and thematic), has already proven its ability for successful automatic classification of landforms (Dragut and Blaschke, 2006; van Asselen and Seijmonsbergen, 2006). It has the potential to detect landslides automatically in a better way than the pixel-based methods, by incorporating a multitude of landslide diagnostic features.

Object-oriented image classification is a knowledge driven method, whereby spectral, morphometric and contextual landslide diagnostic features can be integrated based on expert knowledge to accurately detect landslides (Barlow et al., 2006; Barlow et al., 2003). Since landslides occur in diverse geomorphic settings, it is crucial to address a landslide as an object embedded in its surroundings. Image segmentation, a mandatory step prior to OOA does this by grouping spectrally homogenous pixels into an object (Baatz and Schäpe, 2000). The significant advantage of OOA is the realistic outputs that can be easily verified on the ground. However, to make effective use of OOA, we need a comprehensive understanding of all potentially useful landslide characteristics, and specifically from a segmentation-based perspective. We also need to update and synthesize the criteria for the detection of landslides as per Varnes' classification scheme, using newer means of landslide inventory preparation, such as high resolution satellite data and DEMs. There have been limited attempts to detect landslides using OOA (e.g. Barlow et al., 2006). However, while they differentiated landslide types such as debris slides, debris flows and rock slides using OOA, their characterisation of different landslide types is essentially data driven by considering a very limited set of parameters. In another recent study, Moine et al. (2009) used shape, spectral, texture and neighbourhood features, but no morphometric parameters, to detect landslides from aerial and satellite images using OOA. This clearly shows that the potential of OOA for automatic landslide detection has so far not been fully exploited. Using geomorphometry tools implemented in modern GIS softwares, and with the possibility of extracting many spectral, spatial and some morphometric parameters in image processing softwares, landslide characterisation can be done efficiently in comparison to tools available to previous researchers (e.g. Barlow et al., 2006; McDermid and Franklin, 1994; Pike, 1988), also creating possibilities for less data driven approaches.

The purpose of this chapter is to update and synthesize the diagnostic features for semi-automatic detection (recognition and classification) of landslides, to provide an effective basis for researchers to develop object-based landslide mapping routines. The potential of spectral landslide diagnostic features such as NDVI, shape features such as length/width ratios, asymmetry, texture, and morphometric features such as slope, terrain

curvature and flow direction, derived from high resolution satellite data and DEM, respectively, is discussed in this chapter. OOA is effectively a combination of segmentation to derive image primitives, and their subsequent classification based on characteristics calculated from the extracted objects. This chapter focuses primarily on object classification. In a separate study we address the segmentation and achievement of complex landslide shapes. Segmentation and extraction of spectral and texture characteristics were carried out using Definiens Developer software, while ArcGIS was used to derive additional morphometric indices. A complex analysis routine was then built in Definiens Developer to test how well all available spectral, textural, morphometric and contextual information can be used to detect landslides unambiguously. We test this routine in part of the High Himalayas that suffers extensively from landslides, and where efficient remote sensing data based techniques provide a real potential for improved landslide hazard and risk analysis.

## **4.2 *Landslide characterisation from satellite data and DEM***

Characterisation of landslides and development of a knowledge base for their automatic detection are briefly discussed here. Image characteristics used for visual interpretation of landslides are equally important to the success of an automatic detection technique. Some of them, such as vegetation, drainage and morphology, were discussed by Soeters and van Westen (1996). The spectral characteristics based on DN or NDVI values have been used by previous researchers for pixel based methods of automatic detection of landslides (Nichol and Wong, 2005a; Tarantino et al., 2007). To classify landslide types using object-based methods, Barlow et al. (2006) developed landslide diagnostic features using textural characteristics. However, they omitted one important parameter, morphometry, which is critical to distinguish commonly occurring landslide types: debris slides, debris flows and rock slides. Similarly, Moine et al. (2009) translated qualitative expert knowledge into quantitative criteria for characterising landslides using shape, spectral, texture and adjacency features. Although both studies made important contributions to object-based automatic detection landslides, failure mechanisms such as translational or rotational and their diagnostic features were not included. According to Varnes (1978), it is an important aspect of landslide studies when considering future hazard and ground stability analysis. Therefore, we discuss the following types of landslides based on their frequency of occurrence, and importance to landslide risk assessment. The discussion is illustrated with schematic block diagrams with emphasis on contextual and morphometric properties of landslide types (Figure 4.1).

- **Translational rock slides**

These are defined as the “movement of rock down the slope along a planar or undulating surface of rupture” (Cruden and Varnes, 1996). The value of terrain curvature is very low, sometimes close to zero. The source area is in a rock outcrop and slope is generally steep (Figure 4.1a).

- **Rotational rock slides**

These are defined as the “movement of rock down the slope along a curved and upwardly concave surface of rupture” (Cruden and Varnes, 1996). It shows abrupt change in slope morphology, i.e. concavity in the zone of depletion and convexity in the zone of accumulation. The slope may be step-like due to backward tilting of slope facets (Soeters and van Westen, 1996). The crown shape is arcuate and located on or adjacent to the bed rock (Figure 4.1b).

- **Debris flows**

Debris flows are spatially continuous movements of debris saturated with water (Cruden and Varnes, 1996). It generally has a moderate slope and large run-out, and a scouring effect is observed along the run-out path (Figure 4.1c). The transition between slides to flows is gradual and depends on water content. Therefore, debris slides are characterised by a limited run-out length. The source area can be in a deep zone of weathering, or topographic surface with large overburden depth.

- **Shallow translational rock slides**

These landslides are surficial in nature and normally associated with first or second order drainage. They have generally very small width in comparison to length (Figure 4.1d). Therefore, the length/width ratio is high and distance of the median line to the landslide periphery is very low.

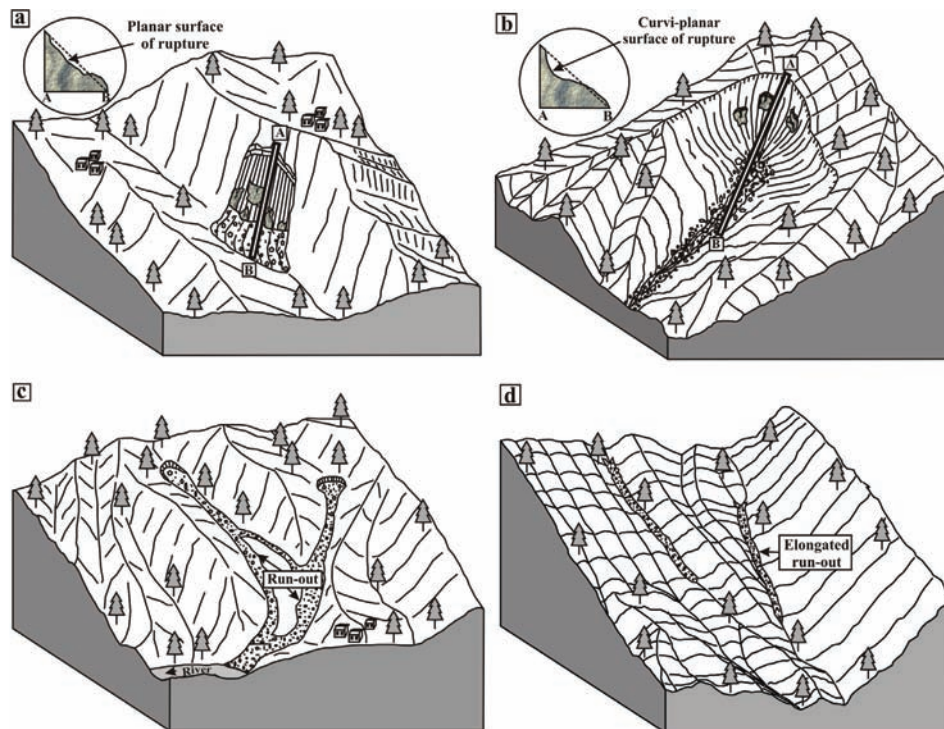


**Figure 4.1:** Schematic block diagrams of landslide types. (a) translational rock slide, (b) rotational rock slide, (c) debris flow, and (d) shallow translational rock slide. Debris slide is not shown separately since it has characteristics similar to debris flow, except less run-out.

### 4.3 Materials and methods

#### 4.3.1 Study area

The Himalayas are one of the global hotspots for landslide hazard (Nadim et al., 2006). An area covering 81 km<sup>2</sup> in parts of the Mandakini river catchment in the High Himalayas of India was selected for this study (Figure 1.3). The extent of the study area was restricted to the watershed boundary. Although direct economic damage in this area is not as high as elsewhere in the world, the limited number of transport corridors, vital life lines for 208 000 people are frequently disrupted by landslides, seriously affecting the livelihoods and development of the people. Identification of landslide events and their types can be of use for more comprehensive landslide risk modeling and mitigation. Detailed geology and geomorphology of the study area is given in section 1.4.

This area offers a good opportunity to test the applicability of the semi-automatic detection technique, not only because of the occurrence of major

and minor landslides, but also due to presence of different types of landslides associated with a variety of land covers. The landslide recognition and classification algorithm was developed for the Madhyamaheshwar sub-catchment and subsequently tested for the Mandakini catchment.

## **4.3.2 Data sources**

### **4.3.2.1 Satellite data**

Steerable sensors and an increasing number of operational satellites have led to satellite data increasingly replacing aerial photographs for landslide studies. Multispectral data acquired on 16 April 2004 by Linear Imaging Self-scanning System IV (LISS-IV) sensor onboard the Indian Remote Sensing Satellite (IRS) P6 (also known as Resourcesat-1) were used for extracting the spectral diagnostic features. These data have been shown to be useful for mapping of major and minor landslides after the Kashmir earthquake in October, 2005 (Vinod Kumar et al., 2006). They have 5.8 m spatial resolution and three spectral bands viz. green (0.52 to 0.59  $\mu\text{m}$ ), red (0.62 to 0.68  $\mu\text{m}$ ) and near infra-red (0.76 to 0.86  $\mu\text{m}$ ). The Resourcesat-1 LISS-IV image was orthorectified using the 10 m DTM created from a 2.5 m resolution stereoscopic Cartosat-1 data acquired on 06 April 2006. The multispectral image was used to calculate the spectral characteristics of landslides, such as NDVI and brightness.

### **4.3.2.2 DEM**

High DEM accuracy is crucial for correctly quantifying the topographic parameters (Dewitte and Demoulin, 2005; Dragut and Blaschke, 2006). We used ground control points obtained from DGPS survey to improve the orientation result of the RPC model during block/scene triangulation of Cartosat-1 data (Baltsavias et al., 2008; Sadasiva Rao et al., 2006), and could achieve a vertical RMSE of 2.31 m. DEMs extracted automatically from aerial photographs/satellite images occasionally contain spurious spikes and pits (Kerle, 2002), although recent technical developments in photogrammetric processing, such as implemented in the SAT-PP approach (Zhang and Gruen, 2006) used in our work, have reduced this problem (Martha et al., 2010c). Photogrammetrically derived DEMs also reflect surface features such as vegetation and man-made objects, making them effectively DSMs. We used DEM editing tools in LPS for manual height correction of isolated trees, while Erdas Imagine Stereo Analyst was used to estimate the average height of the scattered vegetation patches. Subsequently, the height of the vegetation patches was subtracted from the DSM to create a DTM. Elevation values from other potential erroneous areas, such as shadows, were also corrected manually using breaklines. Finally, the DTM was

hydrologically corrected using the FILL function of ArcGIS, and then derivatives such as slope, terrain curvature, hillshade and flow direction were calculated. These derivatives along with DTM were used as input layers for OOA.

### **4.3.3 Segmentation technique**

An important step before characterising diagnostic attributes of features of interest, such as landslides, is the creation of objects/segments that alone or in a group demarcate the boundary of the given feature. This is done using image segmentation, which is a process of dividing the image into objects or regions based on the homogeneity of the pixel values. Image segmentation can be done in different ways, using techniques such as density slicing, and split and merge (Kerle and de Leeuw, 2009). Our analysis was carried out in Definiens Developer software environment, which has different type of algorithms for the image segmentation, multiresolution, quadtree and chessboard being the most efficient ones (Definiens, 2007). These algorithms can be combined effectively to obtain realistic and accurately classified outputs.

Landslides pose a particular challenge to segmentation, as land cover variability (e.g. partial vegetation), and illumination variations as a function of terrain characteristics, often result in spectrally diverse features. It is not practical to attempt outlining landslides as single segments, and some post-segmentation merging or multi-scale processing is needed also due to the typical size variability of landslides in an image. In this study, we initially attempted multiresolution segmentation, a process controlled by scale, shape, colour, compactness and smoothness parameters (Batz and Schäpe, 2000; Definiens, 2007), for delineating landslide candidate objects. After the assignment of a landslide class to qualified objects, we merged them for refinement of landslide object boundaries using a chessboard segmentation technique. OOA supports combining explicit and implicit feature identification, meaning that we can look for features for which unambiguous discriminators are known (explicit), but also remove background features that are not of interest (implicit), iteratively approaching an appropriate label of the sought features, such as landslides (Kerle and de Leeuw, 2009). Research on optimizing the use of OOA to achieve proper landslide segmentation, particularly with a spatial cluster analysis and multi-step segmentation technique, is carried out in a separate study. Once objects are appropriately outlined, Definiens Developer calculates a vast number of parameters for each derived object, such as layer mean, shape, texture, and relationship, based on the available data layers, to be used as class discriminators in OOA.

In Definiens Developer, these attributes of image objects are referred to as object features (Definiens, 2007).

#### **4.3.4 Approach for landslide recognition and classification**

The approach for recognition and classification of landslides is mainly derived from the knowledge developed by experts for detection of landslides during image interpretation. It, therefore, mimics the cognitive approach a landslide expert would employ in visual image analysis. Figure 4.2 shows the methodology adopted for the semi-automatic detection of landslides. The approach for landslide recognition and classification is described in the following three steps.

##### ***4.3.4.1 Identification of landslide candidates (Step-1)***

Bare rock or debris is exposed after a landslide event, giving a bright appearance to landslide affected areas in an image, although at times mixed with remaining or dislodged vegetation. This characteristic of a fresh landslide is very well captured by the remote sensing data and is used as a first criterion for recognition during visual image interpretation. This change to the land cover can be best represented in terms of NDVI, which is sensitive to low levels of vegetation cover. NDVI has been successfully used by previous workers (Barlow et al., 2006; Schneevoigt et al., 2008) to discriminate landslides from vegetated features. Therefore, we used NDVI as a first criterion to identify landslide candidates, and separate them from other areas such as forest land, orchards and crop land.

##### ***4.3.4.2 Separation of landslides from false positives (Step-2)***

Since NDVI is used as a cut-off criterion, objects with similar or lower NDVI values, such as rock outcrops, roads, water bodies and river beds, are likely to be misclassified as landslides. In this step, these false positives are sequentially eliminated from the landslide class by integrating their spectral, morphometric and contextual information in OOA. Potential landslide false positives and the knowledge base for their classification are provided in table 4.1, and the implementation of these criteria in Definiens Developer for OOA is described in section 4.4.2.

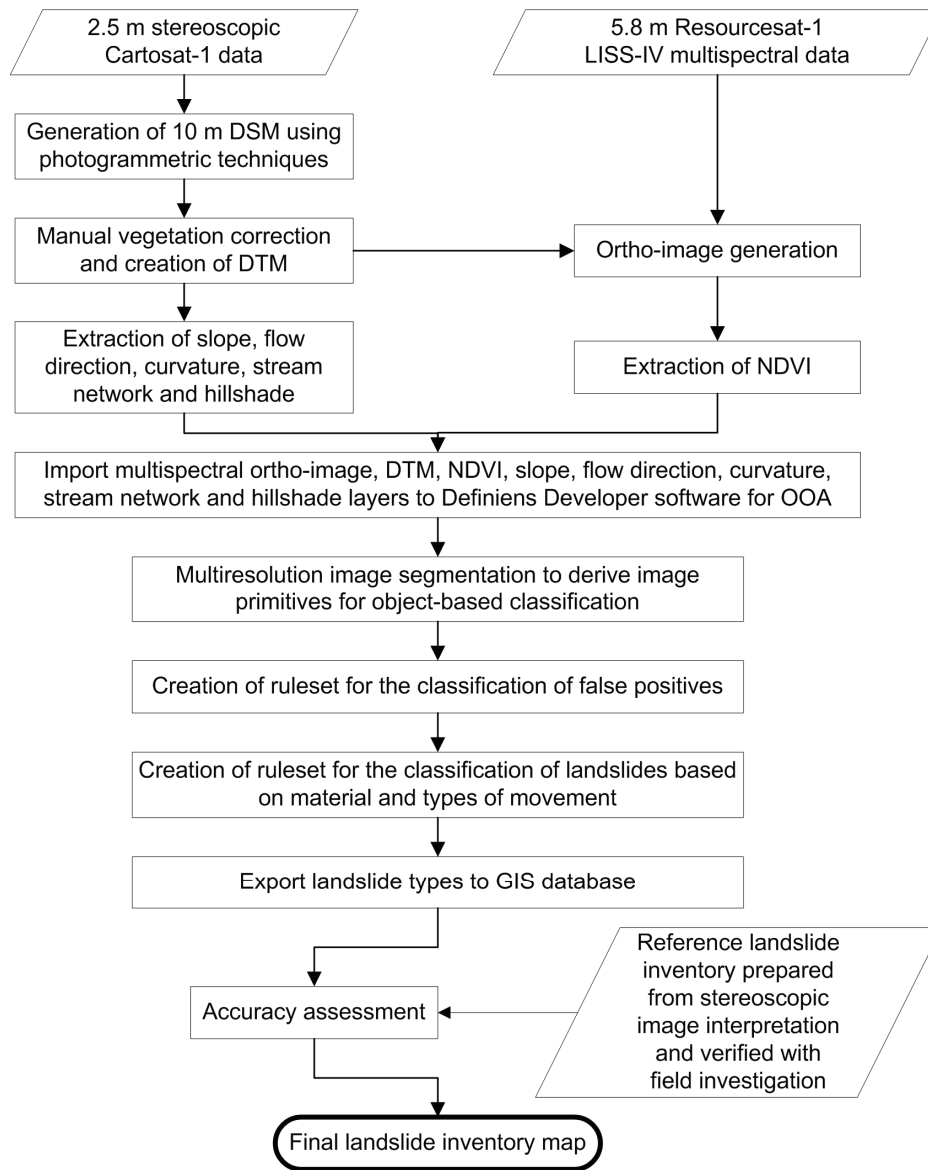


**Figure 4.2:** Generalised methodology flowchart for semi-automatic detection of landslides using object-based methods.

**Table 4.1:** Landslide false positives and their logical classification criteria.

False positives	Criteria
Shadow	Hillshade, a hypothetical image created from DTM for shadow condition using the sun position at the time of acquisition of the multispectral image, gives better information of shadow areas than lower DN values in the multispectral image.
Water body	Spectral information from the near infra-red (NIR) band, which shows lower values due to absorption of electromagnetic radiation (EMR) by water. Topographic information, such as very gentle slope and adjacency to high order drainage carrying perennial flow of water, is also useful.
River sand	High brightness, gentle slope and low relief. Contextual information, such as adjacency to water bodies, is useful. Relief is used to differentiate it from debris flow, which also shows gentle slope, but high relief as the source area is in the mountains.
Built-up area	Large standard deviation values with neighbours (Navulur, 2007), typical texture due to the building pattern and gentle slope.
Non-rocky (e.g. agricultural land)	Low to moderate slope, low to moderate NDVI and typical texture due to the terraced pattern of topography.
Rocky (barren land )	Moderate slope (between 30° to 45°) and medium brightness.
Rocky (escarpment)	Steep slope (> 45°) and medium brightness.
Road	Orientation is across the general flow direction. Contextual information such as high contrast to neighbours, e.g. roads within a forest in the mountains, is helpful.
Quarry	High brightness, and anomalous local depression due to excavation obtained from up-to-date DEM. Contextual information, such as sudden truncation of road, is also useful.

#### **4.3.4.3 Identification of landslide types (Step-3)**

The Classification of landslides based on material and types of movement (Cruden and Varnes, 1996) was developed using the adjacency condition for source area. Morphometric criteria, quantified from Varnes' definition and local field knowledge, were used to classify landslides according to their

failure mechanism. Shape criteria, such as length/width ratio and asymmetry (Barlow et al., 2006), were found to be useful for classifying shallow landslides. The knowledge base developed for classification of landslides from an semi-automatic detection perspective is explained in table 4.2, and their implementation in Definiens Developer for OOA is described in section 4.4.3.

**Table 4.2:** Landslide types and their logical classification criteria.

Landslide type	Criteria
Shallow translational rock slide	Source area is in rocky land with shallow depth, and relatively narrow and elongated shape.
Debris slide	Source area is in a weathered zone or thickly covered soil, moderate slope and low length.
Debris flow	Source area is in a weathered zone or thickly covered soil and moderate slope, but has a long run out zone.
Rotational rock slide	Source area is in rocky land with steep slopes, and terrain curvature is concave upward.
Translational rock slide	Source area is in rocky land with moderate slope and planar terrain curvature.

## **4.4 Results**

### **4.4.1 Extraction of landslide candidate objects**

We carried out multiresolution image segmentation in Definiens Developer using Resourcesat-1 LISS-IV multispectral data for extracting landslide candidates. This process can be guided through the use of scale and shape parameters, the former being used to constrain maximum allowed heterogeneity in a segment. Given the natural landslide size and form variability, there is no single set of segmentation parameters that can delineate all landslide candidates accurately. Figure 4.3 illustrates how sensitive results are to parameter changes. In principle over-segmentation is preferred to under-segmentation, as later merging is possible, but small image features subsumed into a larger segment cannot be resolved later on. Therefore, a small scale factor, although leading to a large number of objects (Figure 4.3b), was necessary to depict the relevant spectral, spatial and contextual properties of landslide.

Even though multiresolution segmentation initially produced sufficiently accurate landslide defining objects for analysis, they were occasionally found to contain impurities such as barren lands and small patches of vegetation. These landslide impurities were detected and removed by a resegmentation process, explained in section 4.4.2.

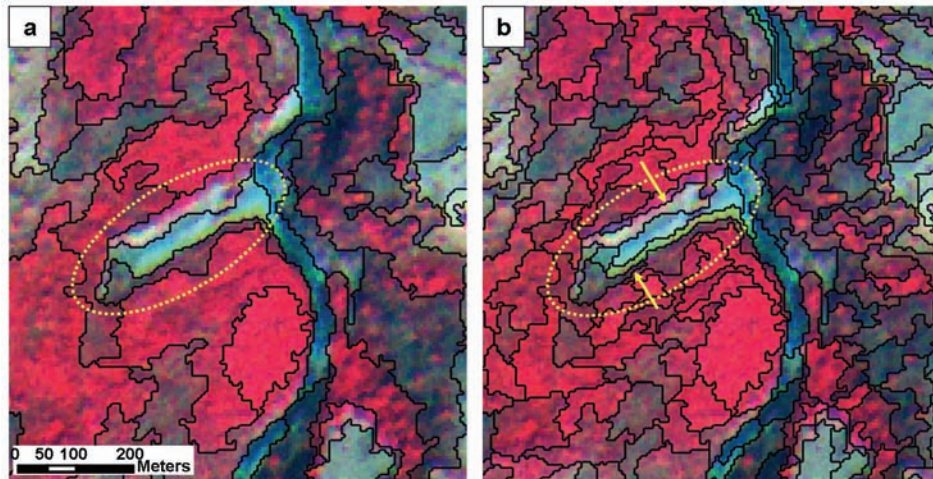


**Figure 4.3:** Multiresolution segmentation of Resourcesat-1 LISS-IV multispectral image. (a) with scale parameter 30, the left and right flanks of the landslide (highlighted with dotted ellipse) are not correctly represented by image objects (with black outline), and (b) with scale parameter 10, objects are fully part of the landslide. Shape of 0.1 and compactness of 0.9 was used for both.

#### 4.4.2 Landslide recognition

An NDVI of 0.18, a value close to the statistical mode of the image NDVI, was found to be useful for discriminating landslide candidates from vegetation cover. From the landslide candidate class all false positives were sequentially eliminated using the criteria provided in table 4.1, ultimately only retaining landslides. The classification sequence and the object features with their values used to classify the false positives are provided in figure 4.4. False positives such as shadow, river water bodies and roads, whose classification needs special attention, are explained below.

Even though detection of shadow areas is possible to some extent, using the low brightness values from multispectral data, a hillshade image is more reliable since other potential sources of low brightness such as water bodies and weathered rocks can be avoided. A hillshade image is generated from a DTM, and it shows the surface illumination for a given position of sun by calculating the illumination values for each cell of the DTM. The position of

sun, i.e. elevation and azimuth, on the date of acquisition of multispectral image is provided by the data vendor in the file header.

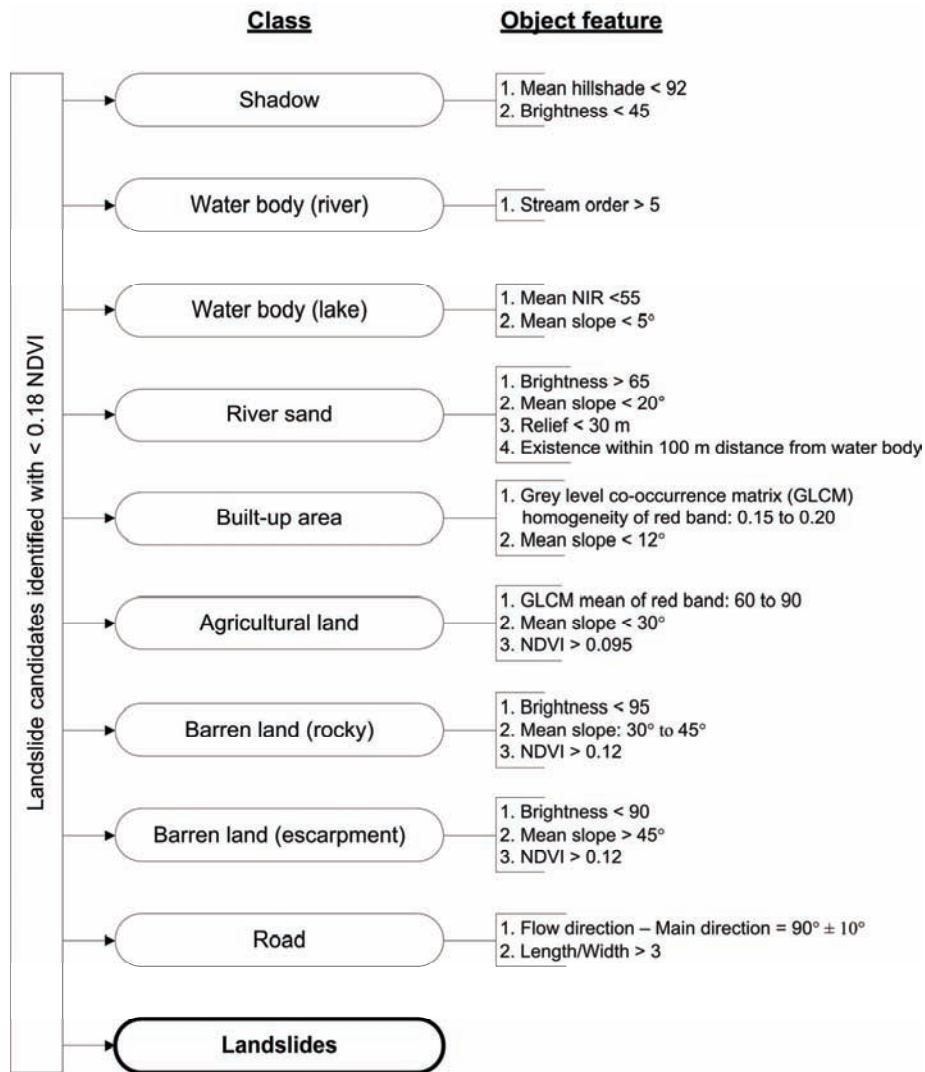


**Figure 4.4:** Quantitative classification criteria for false positives. It also shows the sequence in which false positives were detected with top being attempted first. For acronyms, refer to text.

Detection of water bodies, particularly the river water, was found to be difficult using the NIR band due to partial absorption of EMR. This is because river water in the mountains flows at a high speed carrying suspended sediment load and mostly big boulders on the river bed are exposed above water level, prohibiting complete absorption of EMR. Also, when a river flows

in a deep gorge it is either covered by trees or topographic shadow. We, therefore, used the DTM to automatically derive the stream network and ordered them using the Strahler method (Strahler, 1965). This was used as an input thematic layer during OOA. In the study area, stream order five and beyond shows perennial flow of water. Therefore, only candidate objects intersecting such high order streams were assigned river water bodies class (Figure 4.5). However, deep water bodies such as lakes were detected using low NIR values.

Moderate to gentle slopes in mountainous areas are often converted to terraces for agricultural activity (Figure 4.6). These terraces are created contour parallel, and width of such terraces is largely uniform. This feature of the terrace offers a unique texture in the image and can thus serve as a diagnostic feature. The frequency of combination of grey levels, i.e. texture in an image, is calculated using grey level co-occurrence matrix (GLCM), and in Definiens Developer software GLCM values are calculated using Haralick's method (Haralick et al., 1973). Mean GLCM of the red band discriminates the terrace pattern clearly and was thus used in combination with slope and NDVI to classify agricultural land in OOA (Figure 4.4).

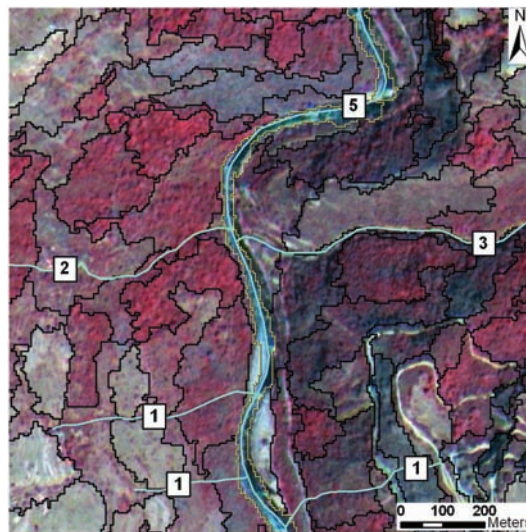


**Figure 4.5:** Image object (yellow outline) identified as river water body using automatically derived stream network. The numbers show the stream order.

Flow direction is the direction of steepest descent, and roads are oriented perpendicular to flow (Figure 4.7). Flow direction was derived from the DTM in ArcGIS using the *Dinf* (infinity direction) approach, which calculates the flow in all possible directions and assigns a value in radians counter clockwise from east between 0 and  $2\pi$ , based on steepest slope on a triangular facet

(Tarboton, 1997). The relatively orthogonal relationship between the flow direction and the main direction (longest axis direction) of false positives, combined with high length/width ratio was found to be extremely helpful for identification of roads (Figure 4.7). Candidate objects with a main direction relatively parallel to the flow direction are classified as landslides.

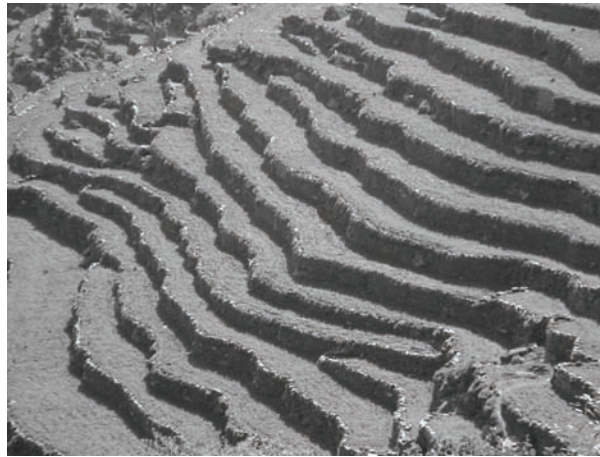


**Figure 4.6:** Field photograph of a typical agricultural terrace.

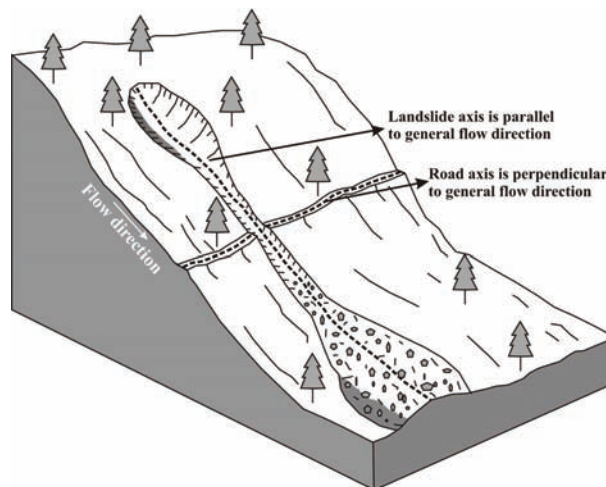


**Figure 4.7:** Relationship between landslide and road object axes with reference to general flow direction.

Finally, a clean-up operation was performed to eliminate non-landslide areas occupying either all or parts of an object. First, an object, part of which was not landslide, was resegmented using a chessboard segmentation technique (Definiens, 2007) to produce small objects in a regular grid (Figure 4.8a). Some of these small objects corresponds to vegetation patches or rocky

barren land, which could not be classified using criteria discussed so far (Figure 4.4), being part of a larger object. However, since now the object size is reduced, they were correctly classified using the same criteria as explained in figure 4.4. This left the objects fully misclassified as landslides to be eliminated (labels 'C' and 'D' in the figure 4.8b). Definiens Developer provides an opportunity to search for additional criteria based on knowledge of the terrain, to refine the results. A careful observation of the image shows that the false positives were mostly river sands, either found along a tributary river (lower order stream) that flows seasonally, or in relatively high slope areas, which, therefore, could not be classified due to non-fulfilment of the river sand criteria defined in figure 4.4. This issue was addressed using a merge option for the objects to redefine the object feature value, and by adding an asymmetry (ratio of the lengths of minor and major axis of an ellipse approximation of the object) condition to the original river sand criteria. Low relative relief of the objects calculated from DTM was also useful in identifying river sands, particularly to differentiate it from debris flow, which has a high relative relief due to the location of its source area at a high altitude in the valley (Figure 4.4). Similarly, some other isolated misclassified landslides were classified as agricultural and rocky barren lands by refining their previous criteria. Thus only landslides were retained, ready to be classified based on type of material, type of movement and failure mechanism.

### 4.4.3 Landslide classification

To apply diagnostic criteria for landslide classification, the small grids that resulted from chessboard segmentation (Figure 4.8a) were merged (Figure 4.8b). The recognised landslides were then classified by following a two-step approach. In the first step, the type of material was assigned to each landslide using contextual information, e.g. landslides adjacent to rocky land were classified as rock slide. Definiens Developer provides an opportunity to implement this knowledge (Table 4.2) by using 'relative border to' object feature (Figure 4.9). The type of movement was assigned using shape criteria (Barlow et al., 2006), with landslides categorised as debris slides, debris flows or rock slides. Rock slides with shallow depth, which is inferred based on the narrow and elongated shape of the objects, were classified as shallow translational rock slides due to their prevalence in the study area and implication on future hazard analysis.

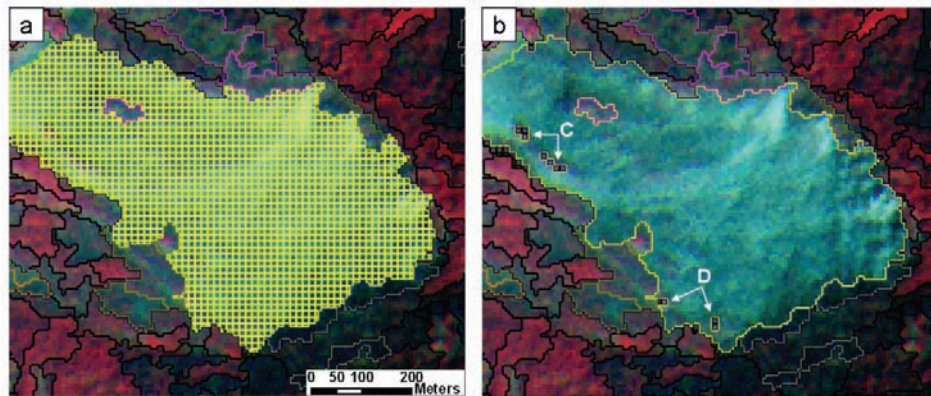


**Figure 4.8:** Resegmentation and merging of objects. (a) chessboard segmentation to create small objects to eliminate small patches of vegetation or barren land (C and D in b) within bigger landslide objects, and (b) classification and removal of smaller patches and subsequent merging of the remaining gridded objects to a single landslide object for application of adjacency condition required for classification of landslide.

Classification of landslides based on the mechanism of failure, i.e. rotational or translational, requires segmentation and classification based on terrain curvature (Table 4.2). Therefore, in the second step, objects classified as debris slide and rock slide were resegmented by multiresolution segmentation technique using the terrain curvature data instead of the multispectral data as done previously. Segmentation using curvature has an advantage that resulting objects reflect variation in concavity, convexity or planarity. Highly concave rupture surfaces thus indicate rotational failure, while planar rupture surface represent for translational failure (Cruden and Varnes, 1996). The objects with mean curvature values less than -1, and between -1 to +1 are classified as rotational and translational rock slides, respectively (Figure 4.9).

The algorithm (segmentation, recognition and classification) developed for the training area, i.e. the Madhyamaheshwar sub-catchment, was subsequently applied to the Mandakini catchment. All detected landslides were exported as a GIS layer for accuracy assessment. Figure 4.10 shows the landslides recognised for the total study area, varying in size between 774 and 291 591 m<sup>2</sup>, respectively.

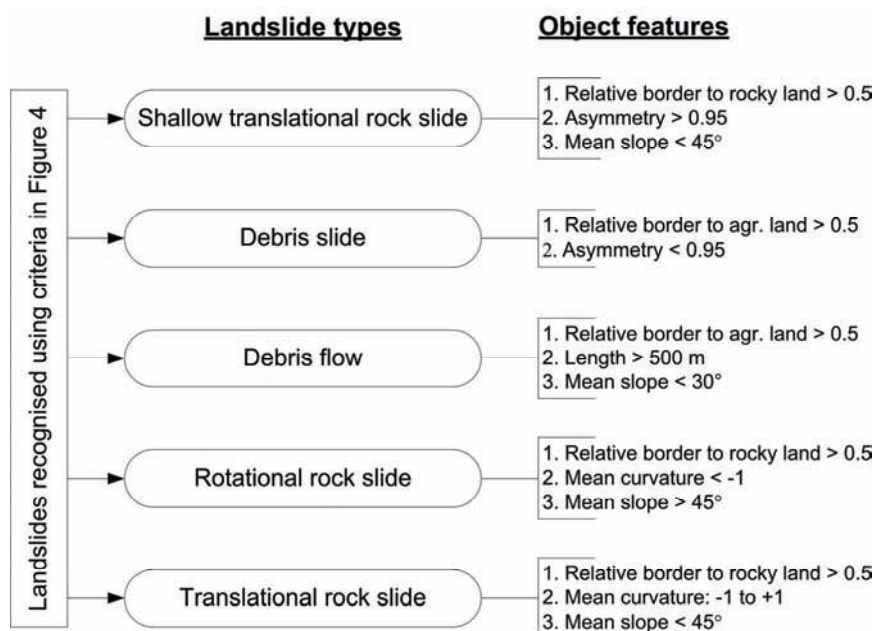


**Figure 4.9:** Quantitative classification criteria for landslide types. It also shows the sequence in which the landslides were classified with top being attempted first.

#### 4.4.4 Accuracy assessment

In total 73 landslides were detected automatically in the entire area. Accuracy assessment was carried out by comparing those against a manually prepared landslide inventory map. A detailed landslide inventory of the Okhimath area, including the watersheds analysed here, was prepared by Naithani (2002) and Rawat and Rawat (1998) after the occurrence of catastrophic landslides in August 1998. However, the inventory was not available in polygon shapes since they inventoried landslides by referring to the nearest village names. We used this information and carried out a stereoscopic analysis of satellite data to prepare a landslide inventory map. The manually drawn landslide polygons were verified during detailed field investigation.

The accuracy of semi-automatically detected landslides was addressed on three levels: (i) number of correct recognition, (ii) correct classification of landslide types (Table 4.3), and (iii) correct detection of landslide extent (Table 4.4).

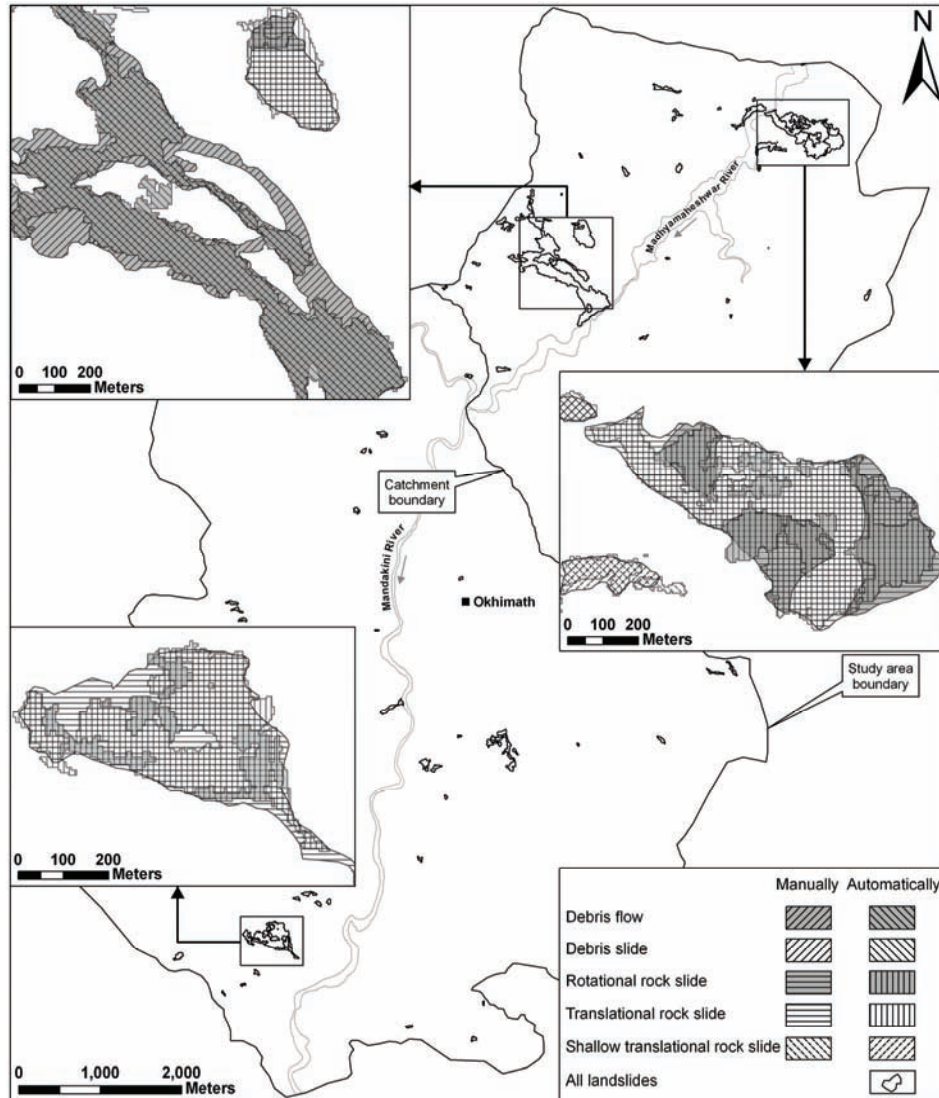


**Figure 4.10:** Landslides automatically detected for the whole study area are shown as black polygons. Three insets show the extent of major landslides detected automatically. Landslides mapped manually by visual image interpretation are shown in the background for comparison. Intersection of line symbols shows agreement.

**Table 4.3:** Accuracy assessment for the number of landslides.

		Landslide detection					
		Manually	Automatically				
			LCRC	LCRWC	TLCR	LNR	LOR
Shallow translational rock slide		31	16	4	20	11	2
Debris flow		1	1	0	1	0	0
Debris slide		4	3	0	3	1	17
Rotational rock slide		6	6	0	6	0	3
Translational rock slide		13	12	0	12	1	9
Total number of landslides		55	38	4	42	13	31
%			69.1	7.3	76.4	23.6	56.4

**Table 4.4:** Accuracy assessment for the extent (km<sup>2</sup>) of landslides.

		Landslide detection					
		Manually	Automatically				
			LCRC	LCRWC	TLCR	LNR	LOR
Shallow translational rock slide		0.220	0.103	0.005	0.108	0.039	0.007
Debris flow		0.387	0.292	0	0.292	0	0
Debris slide		0.052	0.029	0	0.029	0.003	0.043
Rotational rock slide		0.162	0.098	0	0.098	0	0.035
Translational rock slide		0.379	0.312	0	0.312	0.003	0.026
Total extent of landslide		1.200	0.834	0.005	0.839	0.045	0.111
%			69.5	0.4	69.9	3.7	9.2

LCRC: Landslides correctly recognised and classified, LCRWC: Landslides correctly recognised but wrongly classified, TLCR: Total landslides correctly recognised (LCRC+LCRWC), LNR: Landslides not recognised (i.e. error of omission), LOR: Landslides over recognised (i.e. error of commission).

## 4.5 Discussion

Landslide mapping by field investigations is a challenging task in vast and inaccessible mountainous terrain. Visual interpretation of remote sensing data is time consuming, and thus also not ideal, particularly for disaster management and decision making activities, where timely results are valued most. So far there have only been a few attempts at automating the mapping of landslides by pixel based methods (Nichol and Wong, 2005a), which must

fail as DN values alone do not characterise geomorphic processes such as landslide (McDermid and Franklin, 1994). Recently, Barlow et al. (2006) and Moine et al. (2009) started to investigate how landslides can be treated as objects in a contextual analysis. Barlow et al. (2006) achieved good detection accuracy by only considering landslides that are quite large ( $>10\,000\text{ m}^2$ ). Also, failure mechanisms, such as rotational and translational, are not addressed by them. However, Moine et al. (2009) could recognise small landslides, essentially using high resolution earth observation data, but did not use a DEM, eventually ruling out the possibilities of classifying landslide types. Use of expert knowledge to characterise landslides is crucial for semi-automatic detection in OOA. This was addressed partly by Moine et al. (2009), whereas Barlow et al. (2006) used supervised classification with object samples to classify landslide candidates. Therefore, a proper characterisation of landslide types is required for OOA. In this study we extracted objects from segmentation of high resolution (5.8 m) Resourcesat-1 LISS-IV multispectral data and 10 m Cartosat-1 derived DTM, and characterised major landslide types as per Varnes' classification scheme.

A multi-step segmentation approach was followed to recognise and classify landslides accurately. Expert knowledge was quantified using spectral characteristics of the objects such as layer mean and brightness, morphometric characteristics such as flow direction, slope and curvature, shape characteristics such as asymmetry and length/width ratio, textural characteristics such as GLCM (Haralick et al., 1973), and contextual information such as adjacency and containment, to classify a total of nine false positive classes (Figure 4.4). A stream network automatically derived from a DTM was helpful in delineating river water body with ambiguous spectral properties. GLCM texture and orthogonal relationship between flow and main directions of objects were useful for classification of agricultural terraces and roads, respectively. Classification of false positives into non-rocky and rocky lands was useful in classifying landslides based on material type. This study thus considers generic indicators based on expert knowledge to characterise landslides. However, the quantification of specific characteristic features may have to be adjusted, when our algorithm is applied to other areas or used with other image data types.

Merging and resegmentation in Definiens Developer during OOA provided an ideal solution for detecting not only landslides of complex shape and size, but also landslides with multiple failures, e.g. rotational and translational, within a landslide body. Multiresolution segmentation used for the creation of landslide candidate objects, and subsequent chessboard segmentation, successfully eliminated smaller patches of vegetation or barren land, which

later proved essential for refinement of landslide boundaries. Segmentation of landslide objects using terrain curvature data was able to classify landslides based on their failure mechanism.

We achieved 76.4% recognition and 69.1% classification accuracies for the whole study area in terms of number of landslides (Table 4.3). The recognition and classification accuracies achieved for the extent of landslides are 69.9% and 69.5%, respectively. 23.6% of the total number of landslides and 3.7% of corresponding extent could not be recognised. Shallow translational rock slides were recognised and classified with lower accuracy than other four types (Table 4.3). The reason for non-detection of 11 shallow translational rock slides was incorrect delineation of appropriate objects in the segmentation routine, due to their narrow shape and occurrence within spectrally identical land cover units, such as rocky land. Even though the number of identified debris slides was too high (17), their extent is small. These wrongly classified debris slides are actually parts of agricultural land, showing a mixed spectral response owing to their partial conversion to built-up area.

The smallest landslide correctly detected by our algorithm is 774 m<sup>2</sup>. However, to understand the detection capability of our algorithm in relation to landslide size, we applied the landslide frequency–size distribution analysis, a proven technique for landslide inventory assessment (Malamud et al., 2004). Manually (55) and automatically (42) recognised landslides were plotted against their frequencies. Since the range of landslide size is very high, we selected a logarithmic class interval (x-axis). As the class interval is not constant, we also normalised the frequency with their respective class interval to calculate the probability density (Malamud et al., 2004) and plotted it on the y-axis (Figure 4.11). Both trend lines showed good statistical correlation, meaning data resolution and algorithm are sufficient to accurately recognise the most commonly occurring landslide sizes.

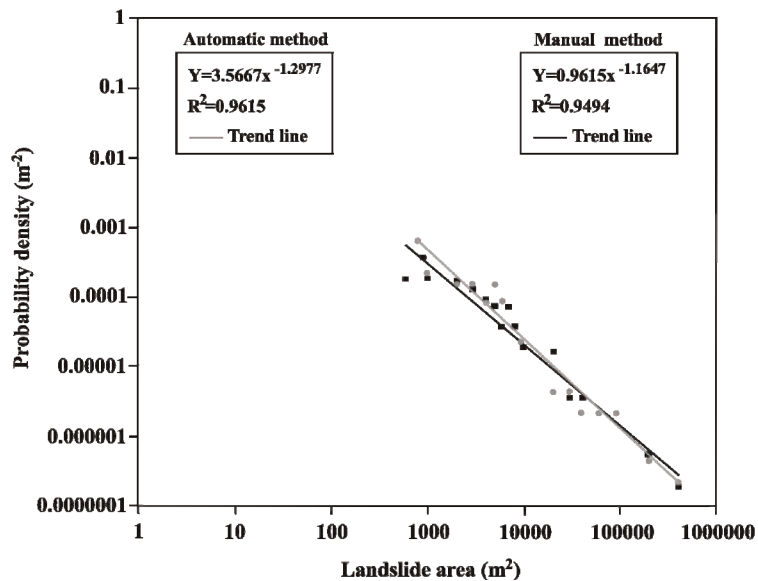


Figure 4.11: Relationship between landslide area and frequency.

## 4.6 Conclusion

In this study landslides were semi-automatically recognised and classified as per Varnes' classification scheme. Landslide diagnostic features typically used by experts during visual image interpretation were used for the characterisation. These characteristic features were updated from an automatic detection perspective, and then efficiently synthesized using OOA for recognition and classification of landslides.

The algorithm was developed in Definiens Developer software using only two primary data sources, high resolution satellite data and a DTM. It comprised 45 individual routines, such as segmentation, merging and classification, which are automatically executed in the assigned sequence. Other parameters used, such as NDVI, slope, flow direction, hillshade, terrain curvature and stream network were derived automatically using algorithms available in basic GIS and image processing softwares. Landslide candidate objects, once identified in the segmentation routine were separated from vegetation by a NDVI threshold. Nine false positive classes (Figure 4.4) were effectively removed by efficient use of DEM derivatives combined with spectral information. For the entire study area, we achieved 76.4% landslide recognition accuracy in five different landslide classes in a terrain featuring spectrally identical land use/cover units. It must also be noted that correct visual identification of these types based on image data alone would be very challenging and would also require the incorporation of elevation information. For example, the smallest automatically detected landslide (774 m<sup>2</sup>) was

missed in the visual stereo interpretation, and only verified with higher resolution Google Earth imagery. Another significant achievement of this study is detection of complex failure mechanism within large landslides. Since the algorithm uses NDVI in the beginning to identify landslide candidates, the result of the OOA, in principle, will be accurate if post-landslide satellite imagery and DTM are used. Therefore, our method has the potential to produce quick results after an earthquake or extreme rainfall event. Also, since the algorithm could distinguish between rotational and translational slides, future hazard analysis and immediate ground control measures can be planned efficiently (Varnes, 1978).

The objective here was to evaluate to what extent landslides, once outlined in a (possibly iterative or multi-stage) segmentation routine, can be correctly detected, using an OOA. The challenge of segmenting complex landslide shapes, which are frequently distorted as a result of sensor and viewing characteristics, and which become indistinct when shadows overlap or contrast is low, we address in the next chapter. The algorithm developed here is available on our website ([www.itc.nl/ooa-group](http://www.itc.nl/ooa-group)), and we welcome testing of the approach with other data types and in other areas.



## Chapter 5: Segment optimisation and data-driven thresholding\*

In the previous chapter, we have detected landslides using OOA. However, the size of the objects used to detect landslides was determined subjectively. Furthermore, a lot of hard coding was involved in the detection of landslides. This chapter presents an approach to select objectively parameters of a region-growing segmentation technique to outline landslides as individual segments, and also addresses removal of hard coding by statistical methods.

### 5.1 Introduction

Landslide inventories are essential for generating landslide susceptibility, hazard and risk maps. To be able to establish a relationship between the temporal probability of triggering events (e.g. earthquakes and rainfall) and the density of landslides caused by them, it is essential to prepare so-called event-based landslide inventories (Guzzetti et al., 2004; Lin and Tung, 2004). Those depict the landslides associated with a single triggering event and should be generated as soon as possible after the occurrence of the event. Satellite remote sensing technology has proven to be the best tool for generating such landslide inventories, especially with the availability of high resolution images (Chang et al., 2007; Chen et al., 2007; Rau et al., 2007; Voigt et al., 2007). Recent advances in computer vision and machine intelligence have led to the development of new techniques, such as object-

oriented analysis (OOA, frequently also referred to as OBIA or GEOBIA) for automatic content extraction of both man-made and natural geospatial objects (Akçay and Aksoy, 2008; Holt et al., 2009). In OOA both the information content of an object, as well as process or feature knowledge, are used to classify features in a landscape. It is a step towards replicating the human cognitive process that underpins visual image interpretation. Image segmentation, a method of dividing the image into non-overlapping regions or segments, is the first major step in OOA, and its quality controls the accuracy of image classification, such as for land cover (Laliberte and Rango, 2009). However, visible features in a landscape are multi-

---

\* This chapter is based on the articles: Martha, T.R., Kerle, N., van Westen, C.J., Jetten, V.G. and Kumar, K.V. (2011) Segment optimisation and data-driven thresholding for knowledge-based landslide detection by object-based image analysis. *IEEE Transactions on Geoscience and Remote Sensing* (In Press).

Martha, T.R. and Kerle, N. (2010) Segment optimisation for object - based landslide detection. In: GEOBIA 2010: geographic object - based image analysis, 29 June-2 July 2010, Ghent, Belgium: proceedings / editor E.A. Addink, F.M.B. Van Coillie: International Society for Photogrammetry and Remote Sensing (ISPRS), 2010. - (International Archives of Photogrammetry and Remote Sensing: IAPRS: ISPRS; XXXVIII-4/C7), 6 p. (In CDROM).

dimensional, and each feature is best represented at a certain scale. Therefore, a single scale factor, the principal segment size controlling parameter, for the generation of optimum segments/objects (group of homogeneous pixels) in such situations does not exist (Blaschke et al., 2006). This is especially the case for features such as landslides that not only vary in shape and size, but also are embedded within different land cover and lithological units. Another challenge is how to classify segments using suitable thresholds for each landslide diagnostic parameter with a minimum level of human intervention, thereby reducing the processing time to provide landslide specific information.

In OOA, classification is carried out on segments rather than on single pixels, by incorporating a multitude of additional information (e.g. shape, texture, and context) associated with the image objects. Availability of this additional information makes OOA more suitable for the detection of geomorphic features such as landslides, compared to pixel-based methods (Blaschke, 2010; Dragut and Blaschke, 2006). OOA uses expert system rules for the classification and is best suited to exploit the spectral family of signatures for a given class and spectral overlap between the classes (e.g. landslides have spectral characteristics similar to roads, river sand or barren rock), due to limited spectral resolution and band width (Navulur, 2007b). However, key to unambiguous detection of landslides is the combined assessment of spectral, spatial, morphological and contextual parameters that help the analyst to define the expert system rules comprehensively (Benz et al., 2004; Navulur, 2007b).

Many landslide defining characteristics, such as those proposed by Varnes (1978), are not exclusively spectral in nature, but rather relate to dimensions and spatial associations, and thus can be meaningfully employed in OOA, where these characteristics are included as class discriminators to separate landslides effectively from other features. In one of the first attempts to apply OOA to landslide mapping, Barlow et al. (2006) used high resolution SPOT 5 data, a digital elevation model (DEM) and image segmentation to classify landslides into debris slides, debris flows and rock slides. However, they did not characterise landslides using landslide process knowledge, instead conducting a supervised classification using spectral, shape and textural properties derived from a limited set of parameters to identify landslides. Only recently, Martha et al. (2010b) comprehensively characterised the spectral, spatial and morphometric diagnostic features of landslides using landslide process knowledge, and identified landslides by OOA using a hierarchical approach similar to (Barlow et al., 2006). Their approach was implemented using three sub-modules: 1) identification of

landslide candidates; 2) separation of landslides from false positives; and 3) classification of landslides. Although OOA for landslide detection has been attempted by previous workers (Barlow et al., 2006; Martha et al., 2010b), several critical issues have not been addressed. These concern: 1) finding reliable procedures to segment landslides of different shape and size, which are also internally strongly heterogeneous; 2) incorporation of relative rather than absolute contextual criteria, in addition to spectral, textural and morphometric criteria to eliminate false positives; 3) extracting suitable object characteristics that allow landslide-type specific identification; and 4) minimising user-driven thresholding of the landslide diagnostic parameters. All of these points are essential for the development of a robust and transferable landslide detection method.

The principal objective of this chapter is to optimise segment boundaries with a combination of different segmentation algorithms and statistical optimisation techniques to delineate automatically landslides of variable shape and size. Another objective is to apply a data-driven/unsupervised thresholding technique to the landslide diagnostic parameters to minimise human intervention. This chapter does not aim at the validation of segmentation algorithms, but rather demonstrates how segmentation algorithms are used with landslide diagnostic parameters to outline landslides as individual segments. Those subsequently allow the application of shape and anatomy-related rules, creating the basis for proper contextual and knowledge-driven analysis.

## **5.2 Segmentation and thresholding methods**

In this section we briefly discuss segmentation and thresholding methods and their main limitations from a landslide detection perspective.

### **5.2.1 Segmentation methods**

The availability of commercial software packages for segmentation-based image analysis, such as eCognition, ERDAS Objective and Envi Zoom, and high resolution Earth observation (EO) data has led to an increase in the application of segmentation techniques for automatic feature extraction (Blaschke, 2010; Haralick and Shapiro, 1985). Initial segmentation approaches aim at the creation of homogenous segments using techniques such as texture-based segmentation (Hofmann et al., 1998) and segmentation based on fusion of colour and texture information (Dubuisson-Jolly and Gupta, 2000). More recently, a multi-resolution segmentation technique, which is a bottom-up region merging technique that starts at a single pixel and continues in several steps until the fulfillment of a user-

defined homogeneity criteria, was developed and implemented in eCognition (Benz et al., 2004; eCognition, 2009). This technique segments the image at both fine and coarse scales, depending upon the scale of interest, using fuzzy set theory, and the approach was explained in detail by (Batz and Schäpe, 2000; Benz et al., 2004). It has been used in several novel applications, as diverse as automatic vehicle detection, change detection studies, extraction of information from scanned paper maps, and geomorphological process understanding (Barlow et al., 2006; Dragut and Blaschke, 2006; Holt et al., 2009; Kerle and de Leeuw, 2009; Laliberte et al., 2004), due to its capability to produce high quality segments at different scales.

An effective incorporation of process or feature knowledge to segment classification is only possible if those image primitives correspond to actual features visible in a landscape. For example, Martha et al. (2010b) showed how different landslide types can be distinguished based on geomorphometric parameters, such as slope, terrain curvature and length/width ratios. Such attributes, however, need to correspond to the entire landslide in question. However, derivation of such optimal segments, particularly with the multi-resolution segmentation used in this study, is an immense challenge, since it depends on a set of user defined segmentation parameters (Espindola et al., 2006; Möller et al., 2007). Those values constrain both the allowed internal image heterogeneity and the object size. Such an approach works well where features of interest are largely homogenous and of comparable size. However, where features are highly variable in terms of shape, size and spectral appearance, the initial segmentation is typically reduced to a trial-and-error method. Möller et al. (2007) proposed a comparison tool to assess the accuracy of image segmentation and to determine the optimal parameters for improving the reliability of a land use/cover classification. However, according to Zhang et al. (2008) an objective evaluation of segmentation quality is a preferable option since reference segments are not required, and criteria for such evaluation are application-dependant and difficult to define. Recently Dragut et al. (2010) developed an estimation of scale parameter (ESP) tool using local variance of object heterogeneity within an image. Espindola et al. (2006) proposed an objective function, to assess the segmentation quality and to determine the optimal segmentation parameter. The objective function is a good indicator, particularly for segments obtained by region-based segmentation algorithms, since it evaluates both intra-segment homogeneity and inter-segment heterogeneity (Zhang et al., 2008). Furthermore, to select parameters for the segmentation of landslides, the approach of Espindola et al. (2006) is more suitable than Möller et al.'s (2007) method, since it does not require a priori knowledge about the terrain. However, Blaschke et al. (2006) emphasised the difficulty

to define the term 'meaningful object', stating that "segments in an image will never represent meaningful objects at all scales, for any phenomena". Therefore, use of multiple scales is crucial to the success of a landscape classification method. In this chapter, we determined the multiple optimal scales objectively, and subsequently linked them to landscape fragments for image-based identification of landslides.

### **5.2.2 Thresholding methods**

The use of thresholds is a primary requirement for land cover classification using EO data. Where in typical classification methods a single threshold value may suffice, OOA is increasingly based on elaborate rule sets that can involve various segmentation, classification, shape adaptation and cleanup steps. For example, the processing routine developed by Martha et al. (2010b) comprised 45 individual steps. While such an approach affords processing flexibility and quasi-cognitive decision making, the resulting process quickly loses flexibility and transferability, as the required threshold values are determined manually from segment attributes. Objective and automated landslide detection thus requires a dynamic or data-driven thresholding approach.

Sezgin and Sankur (2004) categorised thresholding methods into six groups according to the information they exploit. Among those methods, histogram-based thresholding is a standard practice for classification of images (Rosin and Hervas, 2005). Unlike in bimodal histograms, where thresholds are easily calculated using the minimum value between the data population (Rosin, 2001), thresholding in unimodal histograms generally pose a substantial challenge. Clustering methods, such as proposed by Otsu (1979), which are based on nonparametric unsupervised automatic thresholding, are effective for processing images with such unimodal data distribution. Other potential approaches to derive thresholds with cluster analyses for unsupervised land cover classification are K-means and fuzzy C-means. K-means cluster analysis finds natural cluster centers in continuous data, such as spectral class discriminators (normalised difference vegetation index (NDVI), brightness and hillshade) used for elimination of false positives from landslide candidates by Martha et al. (2010b), and is vital for the robustness of a landslide detection method.

## **5.3 Data set, area and methodology**

In this study, Resourcesat-1 LISS-IV multispectral data, which are now available for most parts of the world, were used for image segmentation and derivation of spectral characteristics of landslides. They are 8 bit data with a 5.8 m ground sampling distance. The multispectral channels are in the green

(0.52 to 0.59  $\mu\text{m}$ ), red (0.62 to 0.68  $\mu\text{m}$ ) and near infra-red (0.76 to 0.86  $\mu\text{m}$ ) regions. Along-track stereoscopic data from Cartosat-1, provided with rational polynomial coefficients, were used for the extraction of a 10 m gridded digital surface model (DSM) (Martha et al., 2010c). Cartosat-1 provides 10 bit data with a 2.5 m ground sampling distance. These data have also shown to be useful for mapping of landslides by visual image interpretation technique (Vinod Kumar et al., 2006). The DSM was later converted to a digital terrain model (DTM) and used for extraction of topographic parameters. We used these two primary datasets for the automatic detection of landslides in two perennially affected but geomorphologically diverse areas in the Himalayas (Table 5.1). The methodology was developed in the Okhimath area and tested in the Darjeeling area. While summer images were used for Okhimath area, winter images were used for Darjeeling area, thus, the sensitivity of landslide detection by OOA to seasonal variability in image acquisition was also explored (Table 5.1).

### **5.3.1 Knowledge-based detection of landslides**

In this chapter, we detected landslides by adapting the methodology proposed by (Martha et al., 2010b), which identifies landslides initially along with its false positives and later eliminates them sequentially. We added a new sub-module for the objective determination of parameters for optimal segmentation, and modified the existing sub-module 1 by replacing the static threshold of NDVI with a dynamic threshold obtained from K-means clustering. We also improved the sub-module 2 by: 1) using multiple scales instead of a single scale for the elimination of false positives; 2) replacing the static thresholds of brightness and hillshade with dynamic thresholds; and 3) using relative rather than absolute criteria for identification of false positives. The modified approach for the detection of landslides was separated into four sub-modules, and implemented using eCognition (Figure 5.1). The modules are described in detail below.

**Table 5.1:** Description of study areas.

	Okhimath, Western Himalayas, India	Darjeeling, Eastern Himalayas, India
Centre location (Latitude/Longitude)	30° 33' 07" N / 79° 06' 32" E	26° 54' 06" N / 88° 15' 00" E
Date of LISS-IV scene	01 April 2007	13 January 2004
Date of Cartosat-1 scene	06 April 2006	28 January 2006
Maximum and minimum elevations	2620 m and 1047 m	2024 m and 373 m
Size of study area	29 km <sup>2</sup>	35 km <sup>2</sup>
Landslide types	Shallow translational rock slide, translational rock slide, rotational rock slide, debris slide and debris flow	Shallow translational rock slide, translational rock slide and debris slide
Size of largest and smallest landslide	0.321 km <sup>2</sup> and 0.001 km <sup>2</sup>	0.086 km <sup>2</sup> and 0.001 km <sup>2</sup>
Major land use/cover categories	Barren rocky land, forest and terraced cultivation	Built-up area, forest and tea plantation
Major event	Okhimath landslide (1998) –38 fatalities	Ambootia landslide (1968) – severe loss to cash crops such as tea and oranges.

### 5.3.2 Optimisation of segments (Sub-module 1)

A typical optimisation procedure aims at minimising the under- and over-segmentation to increase the efficiency and accuracy of a classification technique. Given the natural spectral and size variability of landslides, however, a single optimal scale parameter does not exist. Therefore, we addressed segmentation as an iterative process, where an overall analysis may contain several segmentation stages of different types and for different purposes. We used the potential of eCognition's multi-resolution segmentation technique to segment an image without *a priori* knowledge.

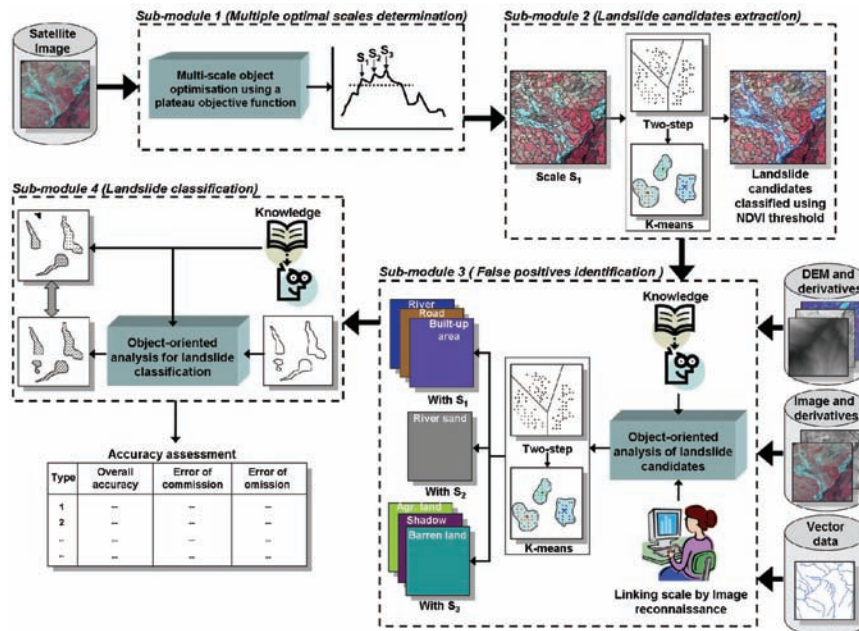


**Figure 5.1:** Concept diagram for knowledge-based detection of landslide using OOA by segment optimisation and data driven thresholding.

In eCognition, segmentation is controlled by scale, colour and shape, with the shape being composed of compactness and smoothness (eCognition, 2009). The scale parameter is a function of the image resolution and is used to control the maximum allowed heterogeneity of the objects, with a lower scale parameter yielding a higher number of segments. Similar to other object-based land cover studies with optical remote sensing data, we assigned a maximum weight for the spectral heterogeneity, i.e. colour, and a minimum weight for shape heterogeneity, since shape and size are not distinctive for natural features such as landslides, unlike for man-made features such as buildings, roads and vehicles. The weights for heterogeneity of compactness and smoothness were maintained equal for similar reasons. However, the principal uncertainty lies in the selection of a scale parameter that is suitable to represent all landslides. To find optimal multiple scales objectively we used Espindola et al.'s (2006) objective function, which is a combination of intra-segment variance ( $v$ ) and Moran's I index ( $I$ ). By varying the scale factor and maintaining uniform weights for spectral and shape heterogeneities, objects at 50 different scales were created for estimation of the objective function. Mean and variance were calculated using the brightness value of objects, which is the average of DN values of the three multispectral bands.

$$v = \frac{\sum_{i=1}^n a_i v_i}{\sum_{i=1}^n a_i} \quad (5.1)$$

where  $a_i$  and  $v_i$  are the area and intra-segment variance of segment  $i$ , respectively. Moran's I index is expressed as:

$$I = \frac{n}{S_0} * \frac{\sum_{i=1}^n \sum_{j=1}^n w_{i,j} z_i z_j}{\sum_{i=1}^n z_i^2} \quad (5.2)$$

where  $z_i$  is the deviation of the brightness value of object  $i$  from its mean ( $x_i - \bar{X}$ ),  $w_{i,j}$  is the spatial weight between object  $i$  and  $j$ , which is 1 for adjacent regions or 0 otherwise,  $n$  is the total number of objects, and  $S_0$  is the aggregate of all spatial weights:

$$S_0 = \sum_{i=1}^n \sum_{j=1}^n w_{i,j} \quad (5.3)$$

The objective function is defined as:

$$F(v, I) = F(v) + F(I) \quad (5.4)$$

Functions  $F(v)$  and  $F(I)$  are normalisation functions:

$$F(x) = \frac{X_{\max} - X}{X_{\max} - X_{\min}} \quad (5.5)$$

### 5.3.2.1 Optimisation strategy with objective function

The maximum value of the objective function is a statistical indicator of optimal image segmentation (Espindola et al., 2006). However, a single optimal scale is insufficient to address the relationship between the spatial structure of an image and the structure of a landscape, although Gao et al. (In Press) reported the highest classification accuracy with single scale segments. To obtain multiple optimal scales instead, we created a simple plateau objective function:

$$F(\text{plateau}) = F(v, I)_{\max} - \sigma \quad (5.6)$$

where  $F(v, I)_{\max}$  is the maximum value and  $\sigma$  is the standard deviation of objective function calculated for 50 different scales, respectively.

The plateau objective function value was used to demarcate the lower boundary of the plateau in the curve created by plotting scale factors and objective functions in x and y axes, respectively. The hypothesis for the

plateau objective function is that the peak values are close to the maximum value of the objective function, therefore, the balance between under- and over-segmentation still remains. Furthermore, the peaks are distinct from each other and locally optimal with respect to their immediate neighbour. Since landslides can occupy significant portions of a post disaster image, this type of plateau pattern can usually be expected. The segments obtained with scales corresponding to these peaks can be related to landscape features according to their size.

### **5.3.3 Extraction of landslide candidates (Sub-module 2)**

The segments created with the scale factor corresponding to the first peak of the plateau were used to begin the landslide detection process. This scale factor has the highest potential to outline landslides of small size in comparison to other scales identified in the plateau function, and also captures the boundary of large landslides occurring in a contrast poor environment, such as within barren rocky land. Landslide candidates were extracted using a NDVI threshold. To standardise NDVI across image dates, pixel values were converted to top of the atmospheric reflectance by correcting for sensor gain and sun position (Song et al., 2001).

#### **5.3.3.1 Thresholding by K-means**

Data-driven thresholds derived from the landslide diagnostic features are essential for the development of an approach that is transferable to other areas and also works well with different types of EO data. The dynamic thresholds of these diagnostic features were derived by cluster analysis with K-means using SPSS software, as compared to the manually derived thresholds used by (Martha et al., 2010b). K-means identifies natural homogenous groups in a continuous variable (e.g. NDVI) and can handle a large number of cases (e.g. thousands of objects). The main objective is to identify K centroids, one for each cluster corresponding to a class.

However, one of the prerequisites for the K-means algorithm is that the number of desirable clusters, i.e. K, has to be predefined. Although an initial guess can be made about the number of existing classes by analysing the image, we used a two-step clustering algorithm to determine the existing classes in an objective manner. Two-step clustering is an exploratory data analysis method that helps in automatic selection of best number of clusters by comparing each cluster solution using a Schwarz Bayesian criterion (Schwarz, 1978). This criterion resolves the problem of overfitting, typical in maximum likelihood estimation, by introducing a penalty term. The cluster centers in NDVI data obtained by K-means algorithm were used as thresholds to identify landslide candidates.

### **5.3.4 Identification of false positives (Sub-module 3)**

Since NDVI was used as a threshold for landslide candidate class, features having lower or equal NDVI values, such as roads, river sands, built-up areas and barren rocky lands, were also detected. Accurate identification of false positives is essential for reducing the error of commission. The false positives were identified with multiple scales, in contrast to the single scale used by (Martha et al., 2010b).

#### **5.3.4.1 Linking optimal scales**

Generally, false positives are of different sizes and, therefore, need to be linked to one of the optimal scales (Figure 5.2). This increases their chances of successful classification using texture and shape-based criteria, statistical neighbourhood conditions, such as the maximum mean difference to neighbour for the identification of built-up areas, and the minimum mean difference to neighbour for identification of barren agricultural land. Small and narrow features in hills, such as roads, built-up areas and rivers, were identified with scale factor corresponding to the first peak, while larger features, such as barren rocky lands and topographic shadows, were identified with higher scale factors corresponding to subsequent peaks. The scale to feature link was established by a quick onscreen reconnaissance of the spatial structure of the segments with respect to the landscape features (Figure 5.2). Finally, K-means cluster analysis was used to derive thresholds for the classification of false positives.

### **5.3.5 Classification of landslides (Sub-module 4)**

Detection of landslides includes recognition and classification (Mantovani et al., 1996). Once all the false positives were identified, the remaining landslide candidate objects corresponded only to landslides. These features, particularly the large ones composed of multiple segments, were merged to single segments to apply process related criteria for their classification. At this stage further segment refinement based on chessboard segmentation was applied to eliminate small patches of vegetation and barren rocky land which had not been detected in the larger segmentation scale.

Classification of landslides based on material (rock, earth or debris) was implemented using a relative border criterion. For example, landslides with high relative border to barren rocky land were classified as rock slides. Finally, landslides were segmented using terrain curvature for classification based on failure mechanism (rotational or translational). For example, rock slides with a negative curvature value represent a concave rupture surface, and thus were classified as rotational rock slides.

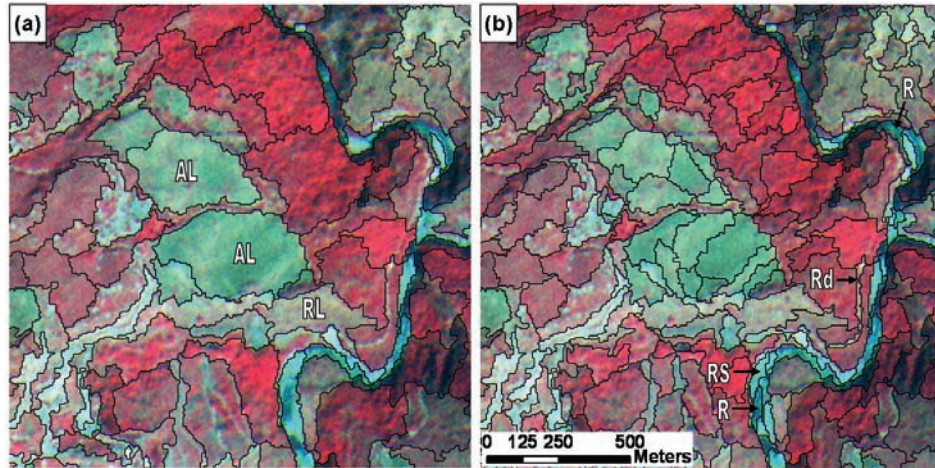


**Figure 5.2:** Spatial structure of the segments for most common landslide false positives (e.g. uncultivated agricultural terraces (AL), rocky land (RL), road (Rd), river (R) and river sand (RS)) in hilly areas. (a) and (b) show segmentation with high (23) and low (13) scale factors, respectively.

### 5.3.6 Transferability of the method

To verify the transferability of the proposed method to unknown areas, we tested the approach developed for Okhimath in the geomorphologically dissimilar Darjeeling area. We first calculated the accuracy in the Okhimath area to test the effectiveness of the proposed method to detect landslides, and then estimated the accuracy of the Darjeeling area to verify its transferability. Assessment of accuracy was carried out by comparing the manually and automatically prepared landslide inventory maps. For Okhimath the detailed landslide inventory maps prepared manually by (Martha et al., 2010b; Naithani, 2002; Rawat and Rawat, 1998) were used as reference, while the map prepared manually by (Ghosh et al., 2010) served as basis for the Darjeeling assessment. Landslides in the reference inventory maps that were affected by shadow or vegetation cover in the satellite image were not selected in the accuracy assessment. Multiple polygons of large active landslides in the reference inventory map were also merged for accuracy assessment. The accuracy of the detected landslides was assessed in terms of their total number and areal extent. Higher success of the areal extent is more desirable than the total slide number, since the former is crucial for data-driven landslide susceptibility, hazard and risk assessment.

## 5.4 Results

Using the plateau objective function value derived through eq. 6, the plateau boundaries for Okhimath and Darjeeling were determined as 1.061 and

1.078, respectively (Figure 5.3). These peaks exceeding the plateau correspond to the optimal scales in the respective images.

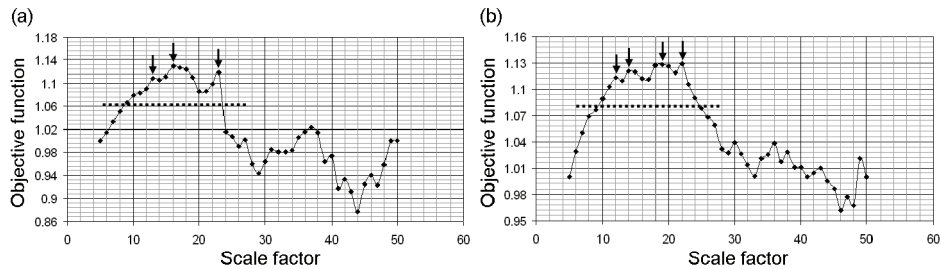


**Figure 5.3:** Objective function for Okhimath (a) and Darjeeling (b), indicating the optimal segmentation scales (the peaks shown with arrows) in the plateau area above dotted line that were used in the OOA process.

Landslides and false positives were characterised using a DEM and its derivatives (slope, flow direction, curvature and hillshade), and parameters calculated from the optical image data (e.g. NDVI, brightness). These diagnostic parameters and their thresholds obtained from K-means clustering were used to create a rule set in eCognition (Table 5.2). This rule set was developed using the data of the Okhimath area and the results are explained in the following section.

Table 5.2: Characteristic features, object properties and thresholds (O: Okhmath, D: Darjeeling) used for the identification of false positives and landslide types.

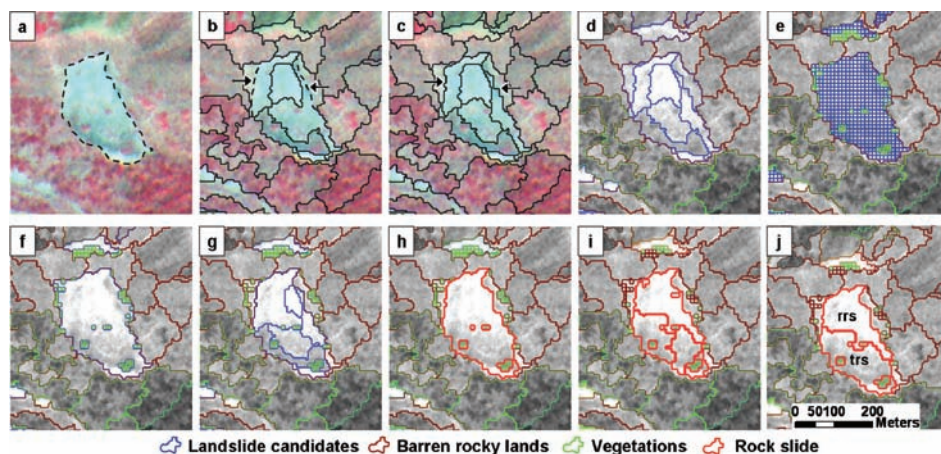
Target feature	Characteristic features	Object characteristics (Threshold value)	Object nature	Thresholding method
Landslide candidates	NDVI	Mean NDVI ( $O \leq 0.22612$ , $D \leq 0.2455$ )	Spectral	K-means clustering
False positives				
Water	Drainage	Stream order ( $O > 5$ , $D > 4$ )	Contextual	Spatial
	NIR band	Mean difference to neighbours ( $O \leq -15$ , $D \leq -10$ )	Spectral	K-means clustering
	Slope	Mean angle ( $O$ and $D \leq 10^\circ$ )	Spatial	Existing knowledge
Built-up area	Red band	Local maxima (mean difference to neighbours)	Spectral	Statistical
	Red band	GLCM contrast ( $O \geq 64$ , $D \geq 68$ )	Spatial	K-means clustering
	Slope	Mean angle ( $O$ and $D \leq 27^\circ$ )	Spectral	Existing knowledge
Road	Water class	Not close to river water ( $O$ and $D > 50$ m)	Contextual	Existing knowledge
	All three bands	Compactness (polygon) ( $O$ and $D \leq 0.2$ )	Shape	Existing knowledge
	Flow direction	Flow direction and Main direction difference ( $O$ and $D$ : between 80 to 105)	Contextual	Existing knowledge
	All three bands	Length/Width ( $O$ and $D \geq 3$ )	Shape	Existing knowledge
River sand	Red band	GLCM contrast ( $O$ and $D \geq 30$ )	Spatial	K-means clustering
	Water class	Close to river water ( $O$ and $D = 0$ m)	Contextual	Existing knowledge
	DEM	Relief ( $O$ and $D \leq 30$ m)	Contextual	Existing knowledge
Shadow	All bands	Brightness ( $O \leq 40.18288$ , $D \leq 53.91474$ )	Spectral	K-means clustering

Table 5.2 continued.....

	Hillshade	Mean Hillshade ( $0 \leq 57.92239$ , $D \leq 14.46621$ )	Spectral	K-means clustering
Agricultural land	Red band	Local minima (mean difference to neighbours)	Spectral	Statistical
	All three bands	Asymmetry (O and $D \leq 0.9$ )	Shape	Existing knowledge
	Slope	Mean slope (O and $D \leq 30^\circ$ )	Spatial	Existing knowledge
Barren land	NDVI	Mean NDVI ( $0 \geq 0.18425$ and $D \geq 0.32378$ )	Spectral	K-means clustering
Escarpment	NDVI	Mean NDVI ( $0 \geq 0.22612$ and $\leq 0.3088$ $D \geq 0.32378$ )	Spectral	K-means clustering
	Slope	Mean slope (O and $D \geq 45^\circ$ )	Spatial	Existing knowledge
Landslide type				
Shallow translational rock slide	All three bands	High asymmetry	Shape	Process knowledge
Debris slide	Agricultural land class	High relative border to agricultural land	Contextual	Statistical
Debris flow	All three bands	Large length	Shape	Process knowledge
Rotational rock slides	Barren land and escarpment classes Curvature	High relative border to barren land and escarpment Very low mean curvature	Contextual	Statistical
Translational rock slides	Barren land and escarpment classes Curvature	High relative border to barren land and escarpment Near zero mean curvature	Spatial	Process knowledge
			Contextual	Statistical
			Spatial	Process knowledge

### 5.4.1 Training area (Okhimath) result

A combination of statistical and classification-based multi-scale segment optimisation was attempted in this study. This had already been the basis for our earlier work that also focused on Okhimath (Martha et al., 2010b), though with the segment generation and subsequent landslide delineation being largely interactive. Here we used the peak scales (Figure 5.3a) from the objective function (13, 16 and 23) to segment the Okhimath image. Scale factor 13 was used to create objects to begin the landslide detection process. As illustrated in figure 5.4b, the next optimal scale factor (16) produced large size objects and was less suitable to delineate the landslide. Scale factor 13 was also used to classify false positives, such as roads, river channels and built-up areas, using the criteria given in table 5.2. The other two scales, 16 and 23, produced large size objects that were linked to correspondingly larger false positives, such as river sands, barren agricultural and rocky lands, and shadow areas.



**Figure 5.4:** Important stages towards successful landslide recognition and classification illustrated for a large landslide in Okhimath. (a) Actual boundary of landslide. (b) Segmentation with scale factor 16 was unable to delineate the left and right flanks (shown with dashed lines) of the landslide. (c) Flanks were correctly delineated with scale factor 13. (d) Detection of landslide candidates with NDVI threshold. (e) and (f) Chessboard segmentation to refine the landslide candidate objects by removing impurities such as vegetation. (g) Resegmentation with scale factor 13, and elimination of barren lands from landslide candidates. (h) Merging again into a single object after removal of all false positives, and classification into rock slide. (i) Segmentation of rock slide using terrain curvature. (j) Classification of rock slide into rotational rock slide (rrs) and translational rock slide (trs) using a curvature criteria.

Landslide candidates were identified on segment level 13 using an NDVI threshold derived from K-means clustering. This is the first and most important step in the landslide detection process, as it eliminates most of the

objects corresponding to forest and agricultural crop lands from the subsequent analysis. Using a two-step auto clustering analysis, four natural clusters of NDVI were obtained. These clusters are related to the major land cover classes of this area, and are also quite distinct (Figure 5.4d). Subsequently, K-means clustering was carried out with K=4 and cluster centers were calculated (Table table 5.3). Objects classified with the cluster center value of 0.22612 could delineate all dark areas of the NDVI image. Therefore, 0.22612 was selected as the threshold for landslide candidates (Figure 5.4d).

**Table 5.3:** NDVI (scale 13), and brightness and hillshade (scale 23) cluster center values used for the thresholding of landslide candidates and shadow, respectively, in Okhimath.

Parameter	No. of clusters	Cluster centers	No. of objects	Total objects
NDVI	4	0.22612	598	2505
		0.09487	177	
		0.39549	755	
		0.30880	957	
Brightness	2	40.18288	74	194
		55.63685	120	
Hillshade	3	223.82503	121	194
		169.47967	50	
		57.92239	23	

Shadow is another common false positive present in all hilly areas. As opposed to the single parameter threshold used for landslide candidates, they were eliminated by simultaneous thresholding of two spectral parameters (brightness and hillshade), also derived using K-means clustering. Use of these two parameters was necessary as they complement each other, i.e. landslides originating from mafic or ultramafic rocks generally have low brightness and thus similarity with shadow. However, they have high hillshade values (if they are in shadow free area), based on which they can be differentiated from shadow. Table 5.3 shows the brightness and hillshade clusters and cluster centers obtained from the two-step K-means clustering analysis.

To find out whether the clusters are sufficiently different to represent the shadow class and to establish the reliability of the combination of brightness and hillshade thresholds to detect shadows consistently, a t-statistic was performed for both parameters, which showed them to be significant and above the critical values (Figures 5.5a and 5.5b). The box plot also showed

that 99% of the cases could be assigned to one of the clusters (Figures 5.5c and 5.5d). These tests showed that the brightness and hillshade clusters are significant, and that K-means cluster analysis can effectively be used to derive thresholds for the identification of false positives even if multiple diagnostic parameters are used together.

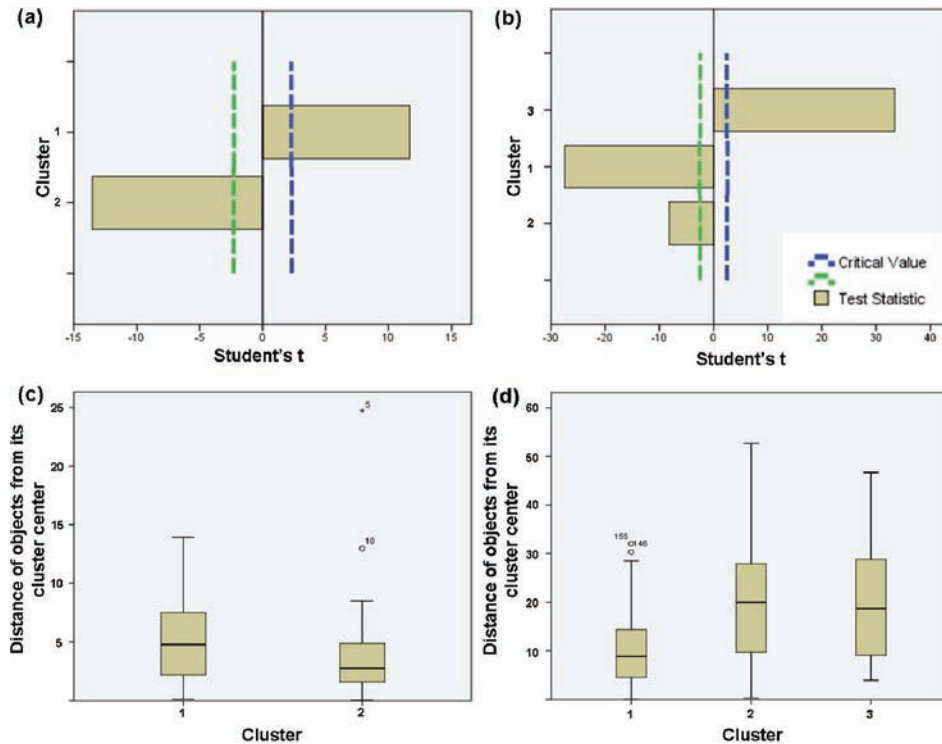


**Figure 5.5:** Statistical evaluation of clusters of brightness and hillshade derived from object level 23 for detection of shadow in Okhimath. (a) and (b) shows Student's t for brightness and hillshade, respectively. All clusters are significantly higher than the critical values. (c) and (d) shows box plots of the brightness and hillshade clusters, respectively, indicating a good allocation of the objects to one of the clusters.

Majority of the thresholds were determined objectively, however, those that are not scene specific but knowledge- or process-driven, were determined interactively (Table 5.2). It is important to classify rocky and non-rocky areas accurately, since they are used for the classification of landslides based on material type. These features were classified using texture, brightness difference to the surrounding objects, and slope. The sub-module 2 of Martha et al. (2010b) was modified, and made more generic and data-driven, by removing the necessity of a threshold, and inserting a contextual information requirement, the maximum mean difference in the red band between an

object and its neighbours for the detection of built-up areas, and the minimum mean difference to detect agricultural lands.

Finally, after removal of all false positives, landslides were classified based on their material and movement using shape and contextual diagnostic features as listed in table 5.2. A total of five landslide types were identified in the Okhimath area (Figure 5.6). Figure 5.4 illustrates the major stages of the analysis, from optimal segmentation and identification false positives to classification of landslides.

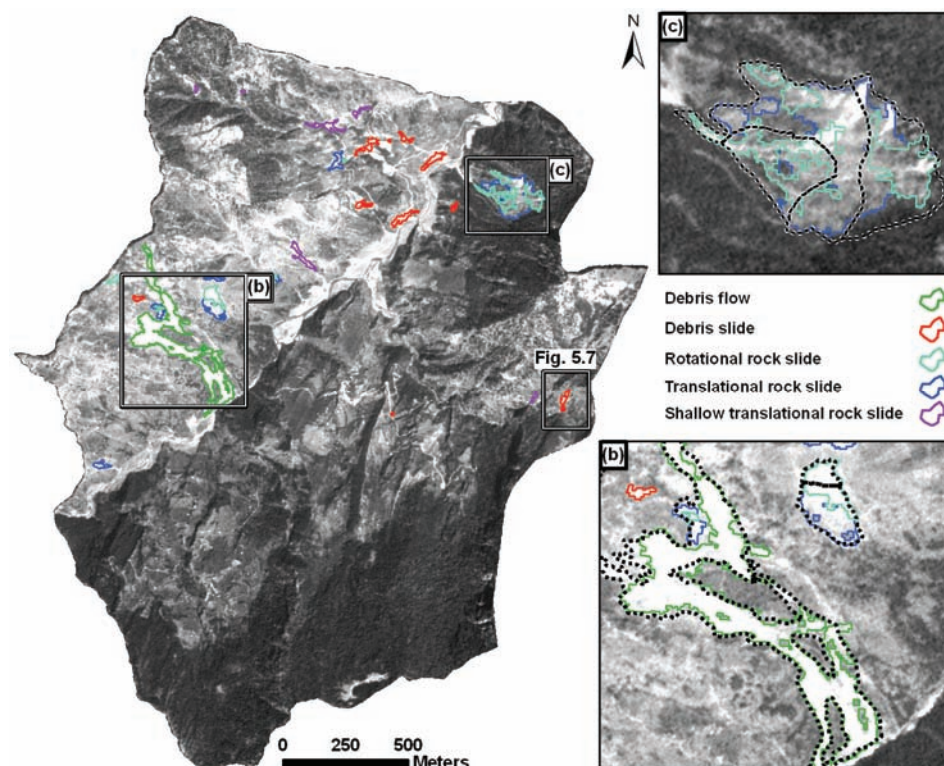


**Figure 5.6:** In total 22 landslides of five different types were correctly recognised using OOA in the Okhimath area. The dotted lines in insets (a) and (b) show the reference landslide inventory.

The major improvements of the approach demonstrated in this chapter in comparison to our previous work (Martha et al., 2010b) are: 1) multi-scale (13, 16 and 23) treatment of false positives, which helped in their improved identification in comparison to single scale (10) treatment used previously, and also eliminated the subjectivity in the selection scale factor for detection of landslides. For example, part of the landslides in the Okhimath area was incorrectly classified as barren land with single scale (10) approach, thereby

reducing its effective area (Figure 5.7); 2) thresholding using K-means, which eliminated the subjectivity in threshold selection for identification of landslide candidates and false positives; and 3) use of relative criteria in comparison to the absolute criteria, which rendered sub-module 3 more generic.

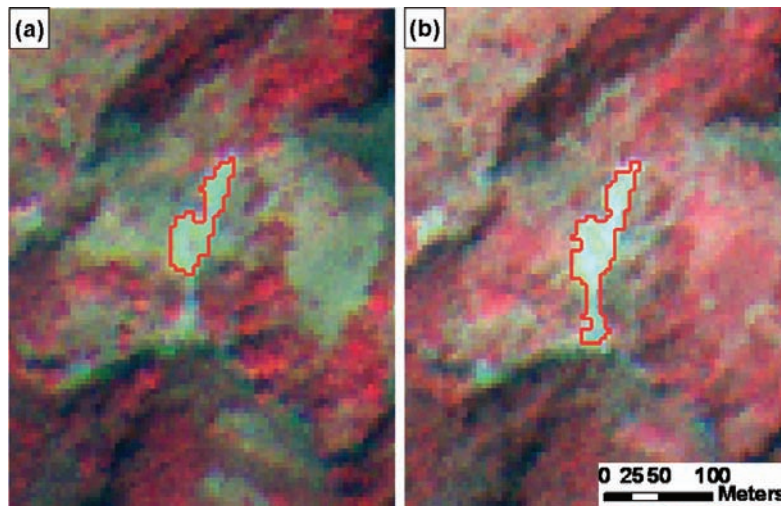


**Figure 5.7:** Effect of multi-scale classification of false positives on accurate landslide detection. (a) part of the landslide was misclassified as barren land since a low scale factor, ideal for classification of landslide, was also used for the classification of barren land. (b) the landslide was completely detected due to multi-scale delineation and classification. The location of the landslide is shown in figure 5.6.

#### **5.4.2 Testing area (Darjeeling) result**

The procedure developed using satellite data and a DEM for Okhimath was tested in the Darjeeling area without any changes to its structure. The optimal scales obtained from the plateau objective function (12, 14, 19 and 22, Figure 3.3b) were used for the segmentation. The analysis began by segmenting the LISS-IV image with the lowest optimal scale i.e. 12. Using K-means clustering, the NDVI threshold (0.2455) for the classification of landslide candidates was obtained. Similar to Okhimath, a small scale factor was able to delineate the boundary of all landslides completely, with the resulting oversegmentation subsequently being reduced by object merging based on NDVI thresholds (Figure 5.8).

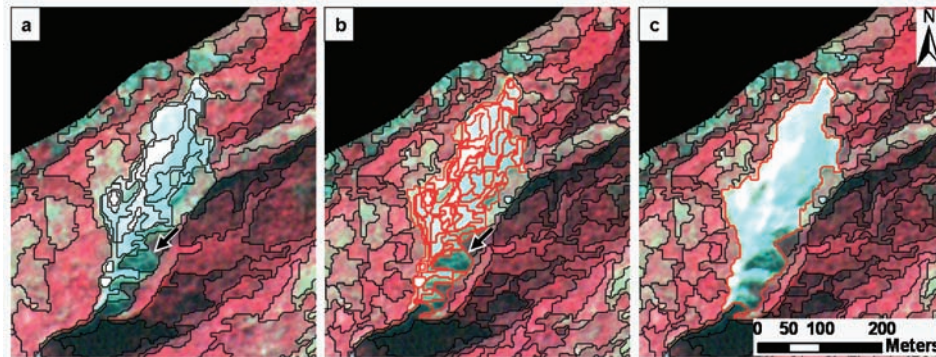


**Figure 5.8:** Effect of segment optimisation on a large landslide in the Darjeeling area. (a) objects created with scale factors 19. (b) objects created with scale factor 12 and classified using NDVI threshold (outlined in red) were able to outline the landslide. (c) merging of segments of the large landslide into a single object, and classification into translational rock slide based on morphometry and context.

Optimal scales were linked to false positives using onscreen image reconnaissance as described for Okhimath, the only subjective part left in the entire procedure. Roads and rivers were identified with scale factors 12 and 14, respectively. Scale factors 19 and 22 were used to identify river sands, shadows and barren rocky lands, respectively. All the three types of landslides present in the Darjeeling area could be detected by this procedure and are shown in figure 5.9.

## 5.5 Accuracy assessment

The overall recognition accuracies (includes correctly and incorrectly classified landslides) for total extent of landslides in Okhimath and Darjeeling was 76.9% and 77.7%, respectively (Tables 5.4 and 5.5). The accuracy in the Okhimath area is higher than that achieved (69.9%) with our previous method (refer to table 4 of Martha et al. (2010b)), where only one scale factor selected by trial-and-error was used (Figure 5.10a). The overall classification accuracy for extent of landslides in Okhimath and Darjeeling was 74.4% and 77.7%, respectively (Tables 5.4 and 5.5). The higher accuracy of the landslide extent assessment, a critical parameter in landslide susceptibility analysis, resulted from better outlining of landslides and identification false positives as per their corresponding size, using multi-scale optimisation.

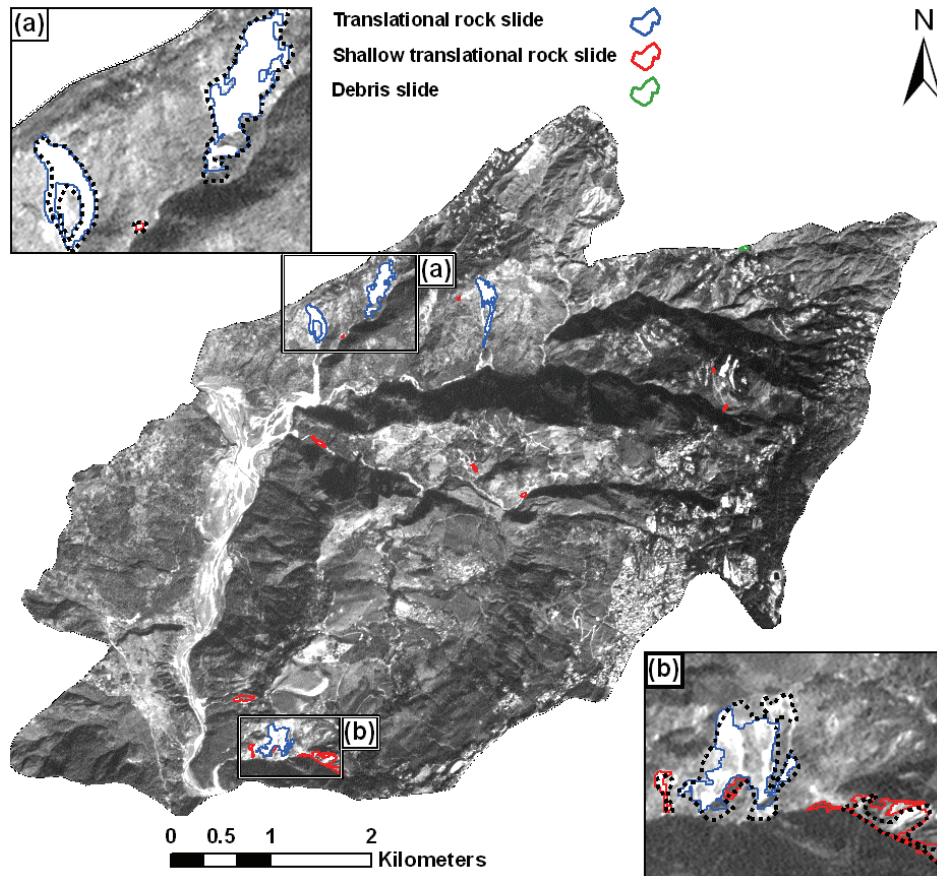
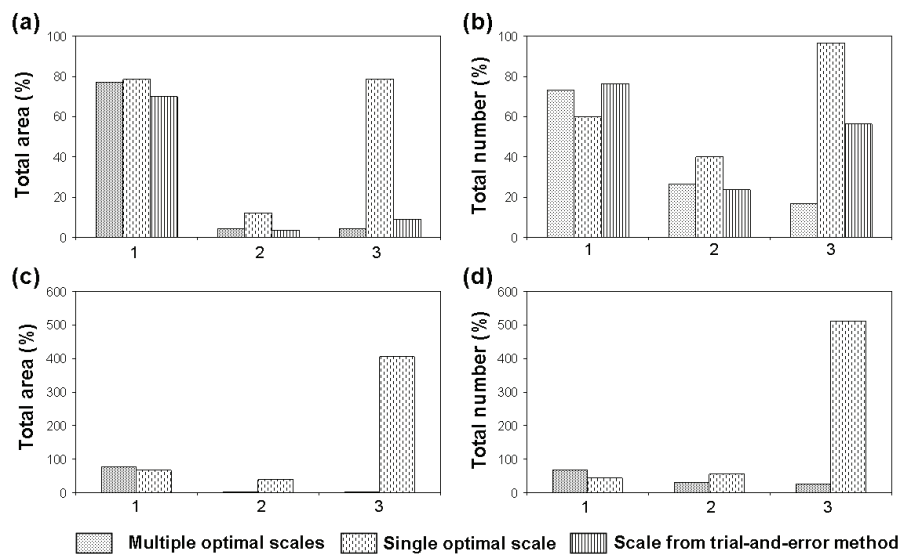


**Figure 5.9:** In total 11 landslides of three different types were correctly recognised using OOA in the Darjeeling area. Dotted lines in insets (a) and (b) show the reference landslide inventory.

The overall recognition accuracy for total number of landslides in the Okhimath and Darjeeling areas was 73.3% and 68.7%, respectively. Although the accuracy in Okhimath is lower than the overall recognition accuracy (76.4%) achieved in our previous work (refer to table 3 of Martha et al. (2010b)), it greatly reduced the percentage of incorrectly recognised landslides, i.e. error of commission (16.6%), compared to 56.4% achieved before (Figure 5.10b). The lower overall recognition accuracy of shallow translational rock slides (60% in both areas) mostly contributed to the 26.6% and 31.2% errors of omission of the total number of landslides in Okhimath and Darjeeling, respectively, in comparison to the contribution from other landslide types (Tables 5.4 and 5.5), a trend similar to what we observed in our previous study in the Okhimath area. This is due to the fact that they are small and narrow, and commonly occur in barren rocky lands, thereby offering limited local contrast that is essential for segment delineation.

So far we obtained higher accuracies from the multi-scale optimisation procedure in comparison to the single scale method used previously. However, to rule out any possibility of poor results due to a wrong manual selection of an optimal scale, and also to verify whether the higher accuracy of the present approach is actually due to the use of multiple optimal scales, we repeated the entire analysis for both areas with segments created using a single scale selected objectively. The scales corresponding to the highest objective function, i.e. 16 for Okhimath and 22 for Darjeeling were selected for the repeat analysis. Thresholds were recalculated using K-means cluster analysis for the new object levels, and landslides were recognised and classified using the same approach. The result showed that, although the overall recognition accuracy has not changed much for both areas (Tables 5.4 and 5.5), the error of commission has significantly increased for both the total number and the extent of landslides (Figures 5.10c and 5.10d). This happened mainly due to the incorrect identification of some of the false positives as landslides.



1. Landslides correctly recognised 2. Landslides not recognised 3. Wrongly recognised as landslides

**Figure 5.10:** Comparison of the accuracies obtained using segments derived from three different methods. (a) and (b) show the total area and number of landslides, respectively, recognised in Okhimath, (c) and (d) in Darjeeling.

Table 5.4: Accuracy assessment for total number and extent (km<sup>2</sup>) of landslides detected in the Okhmath area using multiscale (ms) and single scale (ss) optimisation procedures.

		Landslide inventory																			
		Automatically						Manually													
		Correctly recognised			Unrecognised landslides			Area wrongly recognised as landslides			Correctly recognised			Unrecognised landslides			Area wrongly recognised as landslides				
		I. Correctly classified						II. Wrongly classified						Total (I+II)							
		MS	SS	MS	SS	MS	SS	MS	SS	MS	SS	MS	SS	MS	SS	MS	SS	MS	SS	MS	SS
A. Shallow translational rock slide	No.	15	5	1	4	6	9	7	6	8	1	1	1	7	6	8	1	1	1	1	1
	Extent	0.065	0.030	0.002	0.015	0.019	0.054	0.021	0.018	0.028	0.005	0.005	0.005	0.021	0.018	0.028	0.005	0.005	0.005	0.005	0.005
B. Debris flow	No.	1	1	1	0	0	1	1	0	0	0	1	1	0	0	0	1	0	0	1	
	Extent	0.321	0.266	0.031	0	0.007	0.266	0.308	0	0	0	0.183	0.308	0	0	0	0.183	0	0	0.183	
C. Debris slide	No.	5	4	3	0	1	4	4	1	1	3	20	4	1	1	3	20	3	20	20	
	Extent	0.040	0.028	0.030	0	0.009	0.028	0.039	0.004	0.002	0.021	0.329	0.039	0.004	0.002	0.021	0.329	0.021	0.329	0.329	
D. Rotational rock slide	No.	3	3	1	0	1	3	2	0	1	0	2	2	0	1	0	2	0	2	2	
	Extent	0.125	0.086	0.070	0	0.005	0.086	0.075	0	0.011	0	0.008	0.075	0	0.011	0	0.008	0	0.008	0.008	
E. Translational rock slide	No.	6	4	1	1	3	5	4	1	2	1	5	4	1	2	1	5	1	5	5	
	Extent	0.167	0.124	0.092	0.003	0.029	0.127	0.121	0.009	0.046	0.005	0.042	0.121	0.009	0.046	0.005	0.042	0.005	0.042	0.042	
Total (A+B+C+D+E)	No.	30	17	7	5	11	22	18	8	12	5	29	18	8	12	5	29	5	29	29	
	Extent	% (56.6)	0.495	(23.3)	0.166	(36.7)	(73.3)	(60)	(26.6)	(40)	(16.6)	(96.6)	(60)	(26.6)	(40)	(16.6)	(96.6)	(16.6)	(96.6)	(96.6)	
	Extent	0.718	0.534	0.495	0.018	0.069	0.552	0.564	0.031	0.087	0.031	0.567	0.564	0.031	0.087	0.031	0.567	0.031	0.567	0.567	
		% (74.4)	(68.9)	(68.9)	(2.5)	(9.6)	(76.9)	(78.5)	(4.3)	(12.1)	(4.3)	(78.9)	(78.5)	(4.3)	(12.1)	(4.3)	(78.9)	(4.3)	(78.9)	(78.9)	

Table 5.5: Accuracy assessment for total number and extent (km<sup>2</sup>) of landslides detected in the darjeeling area using multiscale (ms) and single scale (ss) optimisation procedures.

		Landslide inventory												
		Automatically						Manually						
		Correctly recognised						II. Wrongly classified						
		I. Correctly classified		MS		SS		Total (I+II)		MS		SS		
A. Shallow translational rock slide	No.	10	6	3	0	1	6	4	4	6	4	6	4	56
	Extent	0.039	0.036	0.005	0	0.005	0.036	0.010	0.007	0.034	0.006	0.278	0.006	0.278
B. Debris slide	No.	2	1	0	0	0	1	0	1	2	0	2	0	2
	Extent	0.004	0.002	0	0	0	0.002	0	0.002	0.004	0	0.027	0	0.027
C. Translational rock slide	No.	4	4	3	0	0	4	3	0	1	0	24	0	24
	Extent	0.253	0.192	0.187	0	0	0.192	0.187	0	0.071	0	0.897	0	0.897
Total (A+B+C)	No.	16	11	6	0	1	11	7	5	9	4	82	4	82
							(68.7)	(37.5)	0	(6.2)	(68.7)	(43.7)	(31.2)	(56.2)
	Extent	0.296	0.230	0.192	0	0.005	0.230	0.197	0.009	0.118	0.006	1.202	0.006	1.202
							(77.7)	(64.9)	0	(1.7)	(77.7)	(66.5)	(39.9)	(406.1)

## **5.6 Conclusion**

Optimisation of segments and thresholding of diagnostic features are the major challenges in the development of a robust object-based method for fast detection of landslides. In our previous work (Martha et al., 2010b) we showed how manually guided multi-level segmentation, as well as interactively identified thresholds for the dozens of analysis steps needed in the subsequent removal of false positives and the determination of landslide types, led to an overall recognition accuracy of 69.9%. However, a ready application of such a procedure hinges on a higher level of automation and more objective value selection, a problem that is just starting to get addressed in OOA research. In this study we created a plateau objective function using Moran's I index and intrasegment variance that allowed an objective selection of the optimal scales required for identification of false positives. Dynamic parameter thresholds estimated by K-means cluster analysis were used in several classification steps of the OOA. This work showed that multi-scale based identification of false positives helped in achieving a higher overall recognition accuracy (76.9%) of landslides compared to a single scale, and significantly reduced the error of commission affecting out earlier results. Segment optimisation using the result of an intermediate classification was able to delineate small landslides and flanks of large landslides, and outline landslides as individual objects, thereby allowing the application of process-specific criteria to classify them based on material and movement characteristics. Apart from multi-resolution segmentation, chessboard segmentation was used to remove landslide impurities, and refine landslide boundaries. To summarise, the segmentation techniques that were applied to optimise segments for landslide recognition and classification, and that in combination constitute the novelty of this research, include: 1) multi-scale segment optimisation with a plateau objective function; 2) chessboard segmentation to remove landslide impurities such as vegetation within large landslides; and 3) multi-resolution segmentation with terrain curvature to classify landslides based on failure mechanism. K-means clustering proved to be effective in estimating thresholds for landslide diagnostic parameters that were used either individually or simultaneously.

The segment optimisation procedure was conceived with four sub-modules, created using eCognition software, and which proved effective and robust in delineating segments for both small and large landslides embedded in different land cover units. The advantage of the methodology demonstrated in this chapter is that optimal scales and thresholds were selected in an unsupervised manner. The approach could detect five and three types of landslides in Okhimath and Darjeeling areas, respectively. While the structure of sub-modules 1, 2 and 4 of the rule set was kept unchanged for landslide

detection in both the areas, a semi-supervised approach was adopted for sub-module 3, i.e. to link the optimal scales interactively to false positives by analysing a sample area in the image. This remains a limitation of our method, although it was substantially improved from our previous approach by incorporating relative identification criteria and automatic thresholds.

The low recognition accuracy of total number of shallow translational rock slides (60% in both areas) is another limitation of our approach. These slides are generally small and narrow (width < 3 pixels) and could not be delineated as a segment. We address this in a separate study by further refining the objects with more shape control than colour, although insufficient resolution of the satellite image could be one of the reasons for their limited detection. Good overall recognition accuracy of the method indicates that it can be of potential use for the preparation of event-based landslide inventory maps, vital for the planning of short and long term disaster management strategies in mountainous areas. More illustrations and the rule set will be available on our website ([www.itc.nl/OOA-group](http://www.itc.nl/OOA-group)).

### ***Acknowledgement***

We thank S. Ghosh, Senior Geologist, GSI for providing the imagery and validation landslide data of Darjeeling area.



## Chapter 6: Historical landslide inventories from panchromatic images<sup>\*</sup>

In chapters 4 and 5, we have shown how landslides can be detected from multispectral images using OOA. However, frequently panchromatic images are the only data available after a landslide event. Furthermore, preparation of historical inventories, an essential requirement for landslide susceptibility and hazard analysis, relies on the analysis of satellite images and aerial photographs acquired over past few decades that are also mostly available in black and white. In such cases the methodology developed in previous chapters cannot be used directly due to lack of spectral information. In this chapter, we present a new methodology that addresses some of these issues.

### 6.1 Introduction

Fast detection of landslides is vital for rapid damage assessment and supporting disaster management activities. Segmentation-based object-oriented analysis (OOA) provides an alternative to detect landslides automatically from remote sensing images in comparison to traditional pixel-based approaches that are largely limited to spectral information (Blaschke and Strobl, 2001; Townshend et al., 2000; Yan et al., 2006). OOA mimics the human interpretation process and has the potential to identify meaningful geomorphic processes, such as landsliding, using criteria based on shape, colour, texture and context, and produces results that are verifiable and can easily be converted to GIS data (Blaschke, 2010; Navulur, 2007a). Although rapid inventorisation of new landslide occurrences is crucial for planning of immediate disaster response, historical landslide inventories play an important role for the preparation of landslide susceptibility and hazard maps required for setting up long term landslide management strategies (Devoli et al., 2007; Guzzetti et al., 2005).

Previous workers (Barlow et al., 2006; Barlow et al., 2003; Lu et al., 2011; Martha et al., 2010b; Moine et al., 2009) have shown how to detect landslides from multispectral images by OOA. However, in several cases panchromatic images are the only data available after an event (van Westen et al., 2008; van Westen and Lulie Getahun, 2003), where these methodologies cannot be used directly, since they rely on thresholds derived from spectral information during the detection process. Also, satellites such as from SPOT, LANDSAT and IRS-1C/1D, all useful sources of EO data for preparation historical landslide inventory databases, have a panchromatic

---

<sup>\*</sup> This chapter is based on the article: Martha, T.R., Kerle, N., van Westen, C.J., Jetten, V.G. and Kumar, K.V. (2011) Object-oriented analysis of multi-temporal panchromatic images for creation of historical landslide inventories. *Remote Sensing of Environment* (In revision).

camera which has higher resolution than the multispectral counterpart. For example, both IRS-1C and 1D carry a multispectral LISS-III (23.5 m) camera, the data from which if used for preparation of historical landslide inventory will miss smaller landslides. Those, however, can be detected if data from the panchromatic (5.8 m) camera onboard the same satellite were used. Although pan-sharpening can help, availability of both (panchromatic and multispectral) data on the same day of acquisition, preferable for data merging, is often limited. Therefore, a knowledge-based object-oriented landslide detection method is required for preparation of historical landslide inventory from panchromatic images.

Panchromatic images have previously been used for land use / land cover classification using the tonal variation, i.e. texture, in the high resolution imagery. Grey level co-occurrence matrix (GLCM) is by far the most commonly used approach in remote sensing to derive second order texture measures (Haralick et al., 1973). For example, Rao et al. (2002) used GLCM textures in addition to tone for land cover classification from IRS-1D Pan data. Similarly, Zhang et al. (2003) identified the spatial pattern of an urban area using GLCM texture features derived from SPOT Pan data. Change detection using time-series panchromatic images is another method that has been applied successfully for target identification (Negi et al., 2002; Smits and Annoni, 2000), and can effectively be used for preparation of historical landslide inventories from multi-temporal satellite images. Image differencing, principal component analysis, and post-classification comparison are the most common methods of change detection (Lu et al., 2004). Precise geometric registration and normalisation between time-series images are the key requirement for deriving accurate results by change detection (Lu et al., 2004). Negi et al. (2002) used Pan-Pan change detection for the identification of buildings and aircrafts, whereas Nichol and Wong (2005a) used change detection to prepare landslide inventory from grey level images. However, these workers essentially used panchromatic images in pixel-based classification, which has inherent inability to address feature characteristics and context during image analysis.

Object-based land cover classification using panchromatic images has been attempted by previous workers (e.g. Elmqvist et al., 2008). However, object-based change detection technique using panchromatic images has so far not been used to its full potential. Only recently, Dissanska et al. (2009) used object-based post classification change detection technique and classified peat lands from recent high resolution black and white Quickbird images and old aerial photographs. They used GLCM textures to characterise and classify the peat lands and monitored the changes. One of the important properties

observed in the post-landslide panchromatic images is the increase in brightness of the area affected by landsliding due to loss of vegetation and exposure of fresh rock and soil (Martha et al., 2010b). This effect can be captured in an object-based environment to detect landslides by change analysis of pre- and post-landslide images. However, the increase in brightness due to land cover changes such as mining, forest fire and other anthropogenic causes have to be eliminated successfully.

In this study we extend our previous approach by applying more texture measures, the main property offered by high resolution panchromatic images, along with tone and context-based criteria to detect landslides. The methodology is developed using eCognition software. Multiresolution segmentation is used to derive image primitives with optimal segmentation parameters, determined by a plateau objective function (POF), which is a combination of intrasegment variance and spatial autocorrelation. Texture measures based on GLCM are used to identify false positives, such as roads, agricultural terraces and built-up areas. While an IRS-1D panchromatic image (5.8 m) is used for the segmentation and extraction of GLCM textures, a digital elevation model derived from along-track stereoscopic Cartosat-1 data (2.5 m) is used to extract morphometric features of landslides. A combination of these diagnostic features is used in an object-based environment with a knowledge-based approach to detect landslides. The methodology is demonstrated in the Okhimath area in the Himalayas that is severely affected by landslides (Figure 1.3). Only the preparation of a historical landslide inventory for the Okhimath area based on panchromatic images from 1998 – 2006 (except for 2004) is discussed in this chapter. From the year 2007 onwards multispectral Resourcesat-1 LISS-IV Mx data have been used, and a landslide inventory for the recent past was prepared using the methodology discussed in chapters 4 and 5.

## **6.2 Materials and method**

### **6.2.1 Data sources**

To prepare an annual historical landslide inventory by OOA, and taking the landslide super event of August 1998 as a starting point, cloud free panchromatic data (one scene per year) from 1998 to 2006 were procured from archives (Table 6.1). High sensor tilt angles during data acquisition create geometric distortion in mountainous areas and are generally problematic for change detection using time series images. Therefore, only images acquired with  $<5^\circ$  tilt angle, which are generally available in archives, were procured and used in this study. A 10 m digital surface model (DSM) derived from Cartosat-1 stereoscopic images, having a vertical and

planimetric RMSE of 2.31 m and < 1 m, respectively (Martha et al., 2010c), was converted to a digital terrain model (DTM) by applying vegetation height correction (Martha et al., 2010b). The DTM was used to extract morphometric layers such as slope, flow direction and relief. The DTM created using 2006 image forms an input to OOA with the time-series panchromatic images.

**Table 6.1:** Details of high resolution panchromatic satellite data used in this study.

Satellite data	Resolution (m)	Date of acquisition
IRS-1D PAN	5.8	14 April 1998
		02 November 1998
		21 September 1999
		28 May 2000
		24 March 2001
		14 November 2002
		13 April 2003
		13 Mar 2005
Cartosat-1 Stereo PAN-Aft	2.5	06 April 2006

## 6.2.2 Pre-processing of satellite data

### 6.2.2.1 Image geometric correction

Accurate geometric registration of satellite data to a common spatial framework is a principal requirement for image analysis involving multiple satellite images (Prenzel and Treitz, 2004). In this study, first the Cartosat-1 PAN-Aft image was orthorectified using the 10 m DTM, and subsequently used as reference for the geometric correction of IRS-1D PAN time-series images, using a projective transform model. During geometric correction, uniform projection (UTM) and datum (WGS84) were maintained. The maximum RMS error after the transformation was less than 3 pixels, and can be considered satisfactory given the problems of image registration in mountainous areas (Xu et al., 2010).

### 6.2.2.2 TOA reflectance calculation

Quantitative comparison of multi-temporal images requires conversion of DN values to reflectance (Lu et al., 2008). The conversion is essential for two reasons: i) to compensate for the brightness difference due to image acquisition under different sun illumination conditions; and ii) to adjust for the difference in DN values due to the seasonal adjustment of sensor parameters by the data provider. We calculated the top of atmosphere reflectance ( $\rho_{toa}$ ) to address these issues.

$$\rho_{toa} = \frac{\pi L_{\lambda} d^2}{E_0 \cos \theta_s} \quad (6.1)$$

$$L_{\lambda} = \left[ \left( \frac{DN}{MaxGray} \right) \times (L_{max_{\lambda}} - L_{min_{\lambda}}) \right] + L_{min_{\lambda}} \quad (6.2)$$

Where,

$L_{\lambda}$	=	Spectral radiance ( $W \text{ sr}^{-1} \text{ m}^{-2} \mu\text{m}^{-1}$ )
$d$	=	Earth – Sun distance in astronomical units
$E_0$	=	Bandpass exoatmospheric spectral irradiance ( $W \text{ m}^{-2} \mu\text{m}^{-1}$ )
$\theta_s$	=	Solar zenith angle
DN	=	Digital number of the pixel
MaxGray	=	255 (for 8-bit data)

$L_{max_{\lambda}}$  and  $L_{min_{\lambda}}$  are maximum and minimum spectral radiance of the scene, respectively.

Finally,  $\rho_{toa}$  images for all the years (Table 6.1) were calculated and then used for change detection after image normalisation.

### 6.2.2.3 Image Normalisation

Multi-temporal images listed in table 6.1 were acquired in different seasons. The histograms for each image are different due to the difference in atmospheric conditions during image acquisition. Therefore, histogram peaks have to be matched between the images before any quantitative comparison, especially change detection (Cheng et al., 2004). Bi-temporal relative normalisation using a histogram matching technique was applied to normalise the  $\rho_{toa}$  images. Since the landslide super event was in August 1998, the image acquired on 14 April 1998 was the only pre-landslide image out of all the images listed in table 6.1. To carry out image normalisation, first the reflectance of a post-landslide image was calculated, and then the histogram of the pre-landslide image was normalised accordingly. For example, to prepare the landslide inventory of the August 1998 super event by change detection, reflectance of the 14 April 1998 was normalised by matching with the histogram of the 02 November 1998 image. Similarly, to prepare the landslide inventory for the remaining years, i.e. 1999 to 2006, the reflectance of the post-landslide image was calculated and matched with the histogram of the 14 April 1998 image. Change detection was carried out using an image differencing method in a bi-temporal image pair mode to find out the brightness anomalies, which were later attributed to landsliding during a knowledge-based classification with OOA.

### **6.2.3 Detection approach**

We first prepared the landslide inventory for the year 1998 by selecting the image acquired after the landslide super event, i.e. the IRS-1D image of 02 November 1998 that showed the maximum number of landslides. Multiresolution segmentation of this image was carried out, and multiple optimal scales were determined using POF for object-based classification of landslides (Martha et al., In Press). The method to calculate POF is explained in section 5.3.2. The scale parameter corresponding to the first peak of the POF creates smaller segments than the scale parameter of subsequent peaks, and hence, has the maximum chance of capturing small landslides having good brightness contrast with surrounding pixels. Therefore, the first peak scale parameter was used to create segment for the extraction of landslide candidates.

#### **6.2.3.1 Identification of landslide candidates**

In the previous chapter, we showed how a global NDVI threshold was used to identify landslide candidates from multispectral images. Since an increase in brightness after landsliding is a universal property, we used it as a NDVI substitute for the thresholding of panchromatic images. However, instead of applying brightness as a global threshold, we adopted a two-fold strategy to identify landslide candidates; i) change detection using the difference in object brightness of pre- and post-landslide images, which can be expressed by the following equation:

$$Change = \rho_{toa(post-landslide)} - \rho_{toa(pre-landslide)} \quad (6.3)$$

and ii) local brightness threshold of the post-landslide image using a contextual criterion. Specifically, we used the high brightness contrast to darker neighbours to detect brightness anomalies, i.e. relative tonal variation between a landslide and its neighbours caused due to the landsliding process. While the first strategy was useful in the identification of large landslide candidates, the second strategy was useful to identify smaller ones. The second method of thresholding also has the potential to identify landslides in partial shadow areas or within barren lands, due to good local contrast, even where brightness is below the global threshold value. It also reduces overprediction of uncultivated agricultural and barren lands as landslide candidates, thereby reducing the total number of false positive objects to be eliminated in subsequent stages.

Performing change analysis in an object-based environment poses significant challenges in assessing changes and updating thematic maps, due to generation of small size unwanted objects (McDermid et al., 2008). In landslide change detection, the brightness of objects obtained through

segmentation of post-landslide image is compared with the brightness of the corresponding area in the pre-landslide image. Therefore, identification of large new landslides (e.g. object 'A' in figure 6.1b) in this approach is relatively easy. However, existing landslides that have expanded in subsequent years may create problem during object-based change detection. For example, the presence of bright pixels in objects 'B' and 'C' (Figure 6.1b) increases the average reflectance of objects for the pre-landslide image, and therefore may not have sufficient brightness difference to be identified as a landslide candidate using a threshold value. Therefore, we created a sub-object level below the main object level by applying multiresolution segmentation to the pre-landslide image (Figure 6.1c). This supports a better comparison of stable and landslide area of the bi-temporal image pair. For example, objects 'B3', 'C1', 'C3' and 'C5' in the sub-object level can be easily identified now as landslide candidates due to a large brightness difference between pre- and post-landslide images (Figure 6.1d). Later these landslide candidate objects in the sub-object level were used as seeds and allowed to grow using a combination of contextual criteria such as 'border to' the landslide candidates and high brightness of the post-landslide image. This process was executed in a loop until the remaining sub-objects of objects 'C' and 'D' were identified as landslide candidates. In this process, all object constituents of a large landslide in the post-landslide image were identified.

Once all landslide candidates were identified from the post-landslide image, they were merged to minimise the oversegmentation that resulted from the resegmentation using pre-landslide image.

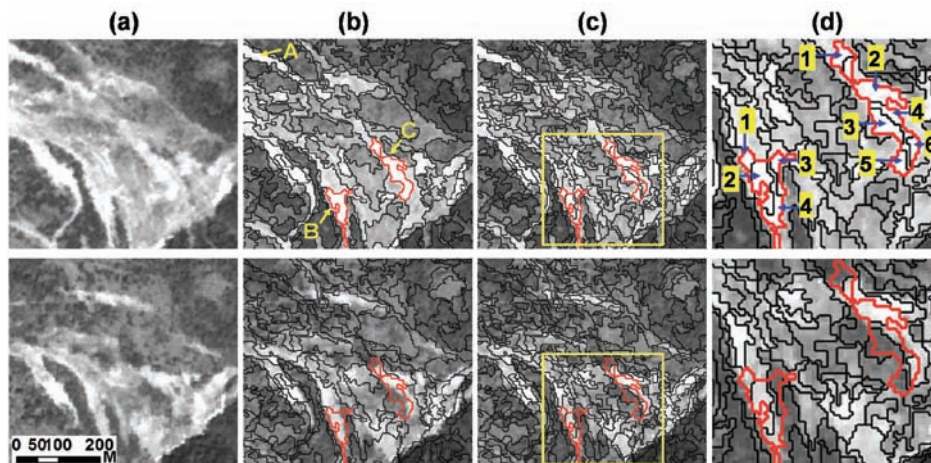


**Figure 6.1:** Top and bottom rows correspond to post-and pre-landslide images, respectively. (a) panchromatic images, (b) main level created by segmenting the post-landslide image, (c) sub-level created below the main level by segmenting the pre-landslide image, (d) sub-level objects (shown with numbers) used for change detection (area outlined in (c)).

### **6.2.3.2 Identification landslide false positives**

Since high brightness is used as a criterion for identification of landslide candidates, shadow areas are no more part of the false positives, as was the case in the previous chapters. Therefore, the use of hillshade image was avoided. Other false positives, such as barren rocky land, agricultural terraces, built-up areas and river sands, were identified in a similar manner as explained in previous chapters. More texture measures were used as a replacement for spectral information. eCognition calculates textures measures after Haralik (Haralick et al., 1973), such as GLCM homogeneity, GLCM dissimilarity, GLCM contrast, GLCM standard deviation, GLCM entropy, GLCM second angular momentum, GLCM correlation and GLCM mean. These GLCM textures are calculated for each object in eCognition, in contrast to those computed for a selected window size in pixel-based analysis. Border effects are reduced by considering pixels that surround the objects (eCognition, 2009). Studies by previous workers (Dissanska et al., 2009; Rao et al., 2002) have shown that these texture measures, when used along with tone, increase the classification accuracy significantly. Therefore, we selectively used these features along with morphometric parameters such as slope, relief and flow direction derived from the 10 m DTM to identify false positives. As discussed in chapter 5, features in a landscape are represented on different scales. Therefore, multiple optimal scales determined from POF were used to segment the landslide candidate objects of the post-landslide image during the identification of landslide false positives.

### **6.2.3.3 Classification of landslide types**

The creation of landslide inventories includes two aspects: i) recognition, and ii) classification based on failure mechanism and material type (Mantovani et al., 1996). Once all landslide false positives were eliminated, the remaining landslide candidate objects corresponded to landslides only. These objects were merged into individual single objects to apply landslide process knowledge for their classification based on movement type and material, using morphometric, shape and contextual criteria. The procedure for classification of landslide type is explained in section 4.4.3.

### **6.2.3.4 Detection from time-series images**

Preparation of historical inventories from EO data requires analysis of time series images. So far we have explained the preparation of the landslide inventory for the year 1998 using the image acquired on 02 November 1998, shortly after the super event, and by comparing the brightness with the pre-super event image (14 April 1998). For preparing inventories for the remaining years, we selected one image per year and repeated the procedure as explained before. For example, to prepare the landslide inventory for the

year 1999, we analysed another pre- and post-landslide image pair, i.e. images of 14 April 1998 and 21 September 1999. The 21 September 1999 image was segmented using the scale corresponding to the first peak of the POF, and landslide candidates were identified using the procedure explained in section 6.2.3.1. The methodology is summarised in a flow chart in figure 6.2.

For the creation of a landslide inventory from the 14 April 1998 image, the methodology was modified slightly, since extraction of landslide candidates by change detection was not possible due to the unavailability of image data prior to this date. Therefore, only the second strategy as explained in section 6.2.3.1 was used to extract landslide candidates.

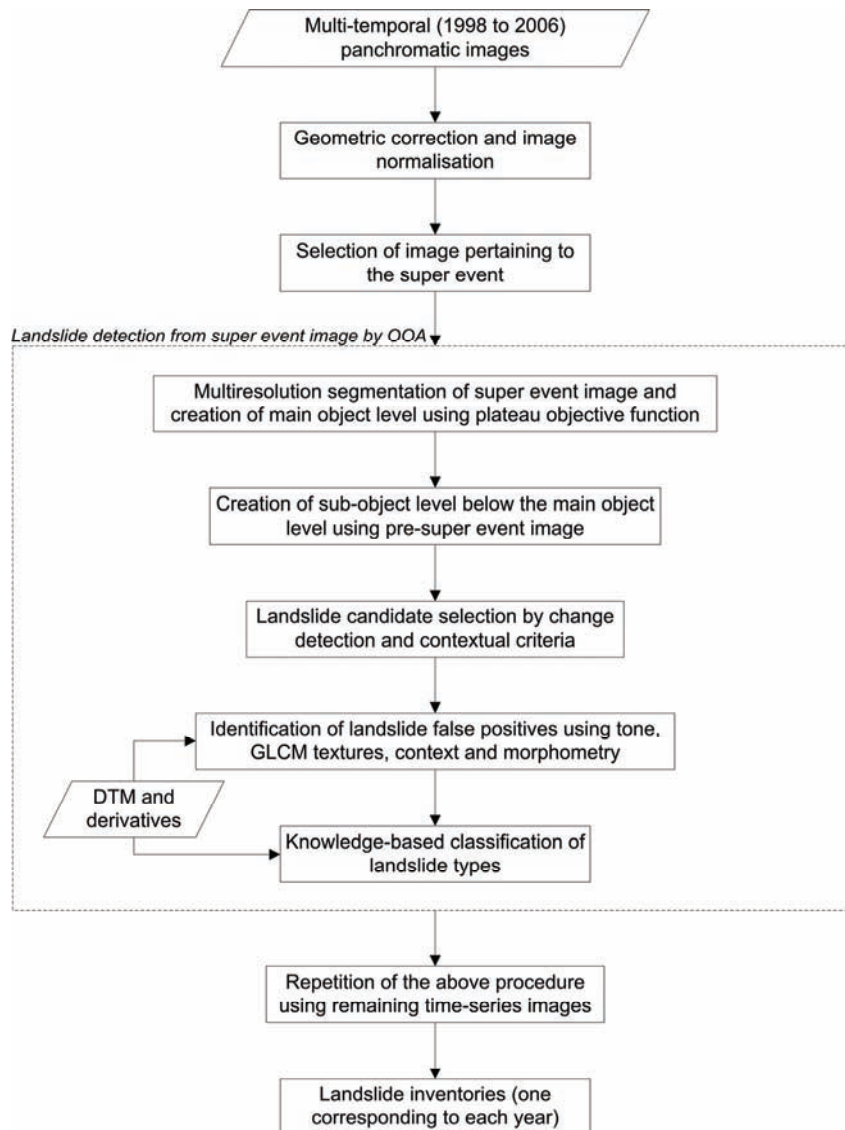


**Figure 6.2:** Methodology flowchart for detection of landslides from multi-temporal panchromatic images.

## 6.3 Results and discussion

### 6.3.1 Landslide candidates

Optimisation of segments is essential to apply criteria based on shape, texture and context for successful identification of landslide false positives since they are represented on different scales in a landscape. All the images as listed in table 6.1 were processed, and optimal scales were determined by

POF (Figure 6.3). From the POF shown in figures 6.3 and 5.3 it is clear that the pattern of the curve above the plateau line is conspicuous irrespective of the data type (panchromatic or multispectral) and spatial resolution. It indicates POF is able to bring out the inherent scales in the images, and can be used as a generic indicator for realising multiple optimal scales. Table 6.2 lists all the multiple optimal scales used for analysis of panchromatic images. The main object level was created using the first optimal scale of the post-landslide image, e.g. 21 for 02 November 1998 image, and the sub-object level was created using the first optimal scale of the pre-landslide image, e.g. 15 for 14 April 1998. Figure 6.4 shows all potential landslide areas, including small and large landslides, as part of the landslide candidates using the two fold strategy.

**Table 6.2:** Optimal scales derived using POF used for extraction of landslide candidates.

Panchromatic images	Optimal scales
14 April 1998	15, 18, 26, 40
02 November 1998	21, 34
21 September 1999	21, 42, 46
28 May 2000	15, 28, 32, 35
24 March 2001	17, 23, 26, 32
14 November 2002	25, 45, 50
13 April 2003	26, 33, 38, 47
13 Mar 2005	14, 19, 21, 29, 31, 36
06 April 2006	27, 29

### 6.3.2 Detection of landslides

For the detection of landslides, identification of all landslide false positives, such as river sand, built-up area, road, agriculture land and barren land, is necessary. We first identified rivers using the stream network (Martha et al., 2010b). Identification of rivers, although not part of landslide candidates, was required since it helps in classification of river sands using an adjacency condition to the river water bodies.

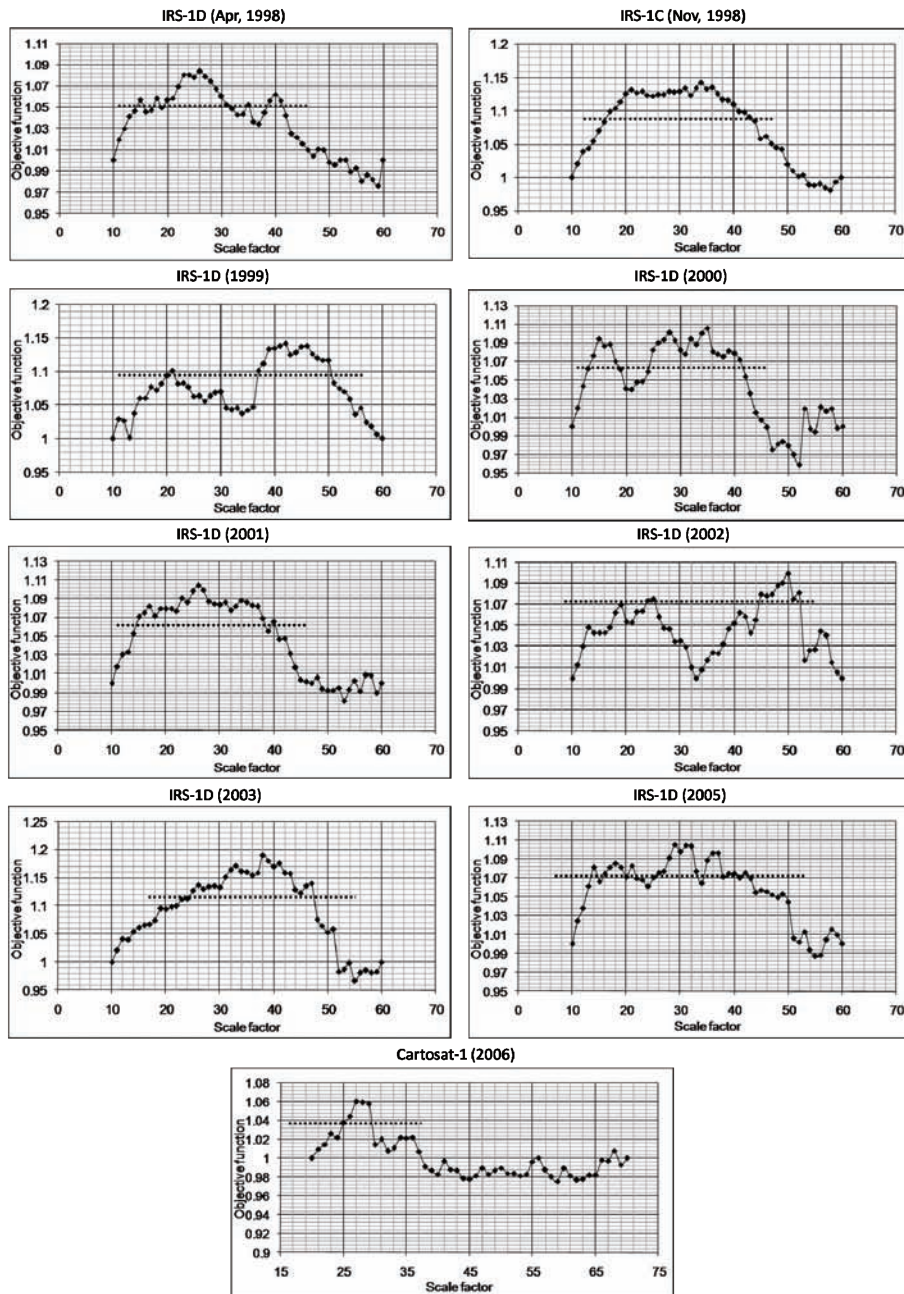


**Figure 6.3:** Objective function curves for multi-temporal panchromatic images. The dotted line corresponds to the POF value and the peaks above the dotted line were used for identification of landslide candidates, and classification of landslides. Although the plateau is almost flat for the IRS-1C (Nov, 1998) image corresponding to the landslide super event, conspicuous peaks (21 and 34) were identifiable using the POF.

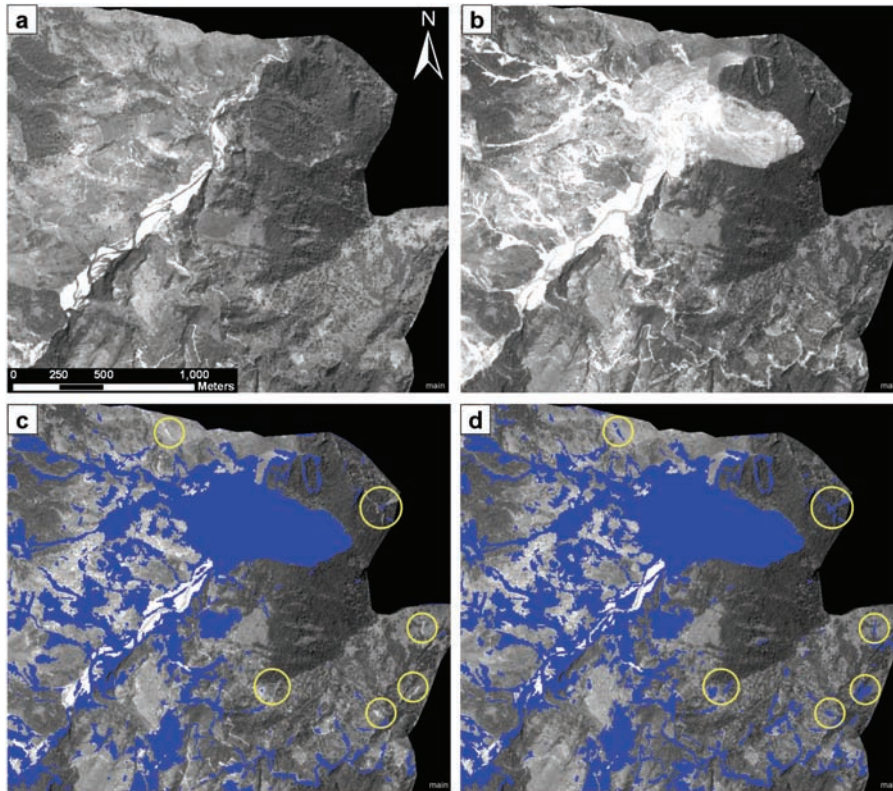


**Figure 6.4:** Extraction of landslide candidates from panchromatic images. (a) pre-landslide image (April 1998), (b) post-landslide image (September 2000), (c) landslide candidates extracted using first strategy, i.e. change detection. Note that small bright features (yellow circles), mostly translational rock slides could not be identified as landslide candidate, and (d) landslide candidates extracted using second strategy, i.e. contextual criteria. All small bright features are now part of the landslide candidates.

To assign multiple optimal scale factors (Table 6.2) to individual false positive classes, we first listed all false positives present in the study area. Then segmentation using all the optimal scales was carried out, and for a small area in the image, individual false positives were linked to that scale factor which not only generated less number of segments (i.e. internal homogeneity is maintained) but also completely outlined the false positive (i.e. heterogeneous from the surrounding). The relationship between the scale factor and false positive obtained for the small area was used for object-based classification of the whole image. For example, from the landslide candidates obtained from 28 May 2000 image, scale 15 was used for the identification of river sands, scale 28 was used for the identification of built-up areas and roads, scale 35 was used for the identification of agricultural and barren lands.

The major contribution of this study is the use of texture in absence of spectral information to identify landslide false positives. The texture measures used are listed in table 6.3. Selection of textures for the identification of false positives was done interactively by carefully analysing the object properties. Only the texture features whose values do not overlap between the false positive classes were used. These texture features were used in conjunction with tone and morphometric parameters such as slope to identify the false positives. For example agricultural terraces, although similar in tone to landslides, could be identified as a separate class using additional criteria such as GLCM dissimilarity, GLCM homogeneity, GLCM standard deviation and slope (Figure 6.5). Roads were identified using shape properties, such as high asymmetry, orthogonal relationship between flow direction and main direction, and very low standard deviation of the DTM.

**Table 6.3:** Texture measures used for identification of false positives. The following combination of textures could identify maximum false positives.

False positives	GLCM textures
Built-up area	GLCM correlation GLCM homogeneity
Agricultural land	GLCM dissimilarity GLCM homogeneity GLCM standard deviation
Barren land	GLCM contrast GLCM dissimilarity GLCM standard deviation

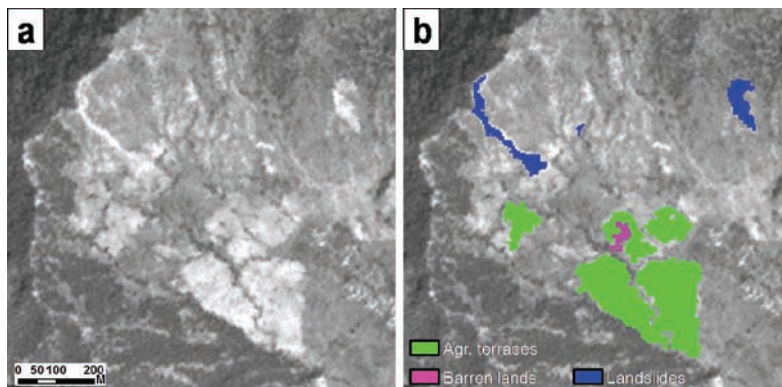


**Figure 6.5:** Usefulness of texture for identification of false positives. (a) post-landslide panchromatic image (13 April 2003), (b) agricultural terraces and barren lands, although having similar tone to that of landslides, could be identified separately using GLCM textures.

After all the false positives are eliminated, the remaining landslide candidates represented mostly landslides. The objects were then merged and classification of landslides was performed using shape and morphometric criteria. One DTM (year 2006) and the morphometric parameters such as flow direction and curvature derived from it were used in the analysis of all multi-temporal images. As long as there are no significant changes in the terrain topography, this DTM can be used for landslide detection in the Okhimath area. However, in case of occurrence of new large landslides, such as the one shown in figure 6.4, which has the potential to change the values of morphometric parameters, a new DTM has to be used. For rapid detection of landslides this causes problem, but if the focus is on inventurisation for earlier years as done in this chapter, one can afford creation of a new DTM.

A total of five types of landslides was identified in this area. Nine landslide inventories, one corresponding to each panchromatic image, were prepared (Figure 6.6). Some of the large landslides may show their presence in multiple years, but their extent will vary depending upon whether they have contracted due to vegetation growth or expanded due to reactivation. Time series analysis helps to identify those landslides that have undergone such changes, since all the objects are referenced to a common spatial framework. Figure 6.7 shows one such change wherein an active landslide is stabilised and becomes active again in subsequent years.

### **6.3.4 Accuracy assessment**

Accuracy assessment was carried out by comparing the landslide inventories created by OOA with the reference inventories, which were created manually using visual interpretation technique. Stereoscopic image interpretation of Cartosat-1 image and cross-reference to high resolution GoogleEarth image were used for the preparation of one reference inventory for each year. Since most of the landslides, e.g. landslides triggered after the super event of August 1998, were stabilised through revegetation, it was difficult to check them now in the field. However, landslide inventories and reports prepared by previous workers (Naithani, 2002; Rawat and Rawat, 1998) were referred to during the creation of reference landslide extent and type. Detection of landslides and correct identification of their extent are important for disaster damage assessment and landslide hazard analysis. Therefore, accuracy assessment was carried out for the total number and extent of landslide detected by the semi-automatic method at five levels: I) correctly classified; II) incorrectly classified and III) correctly recognised (I+II).

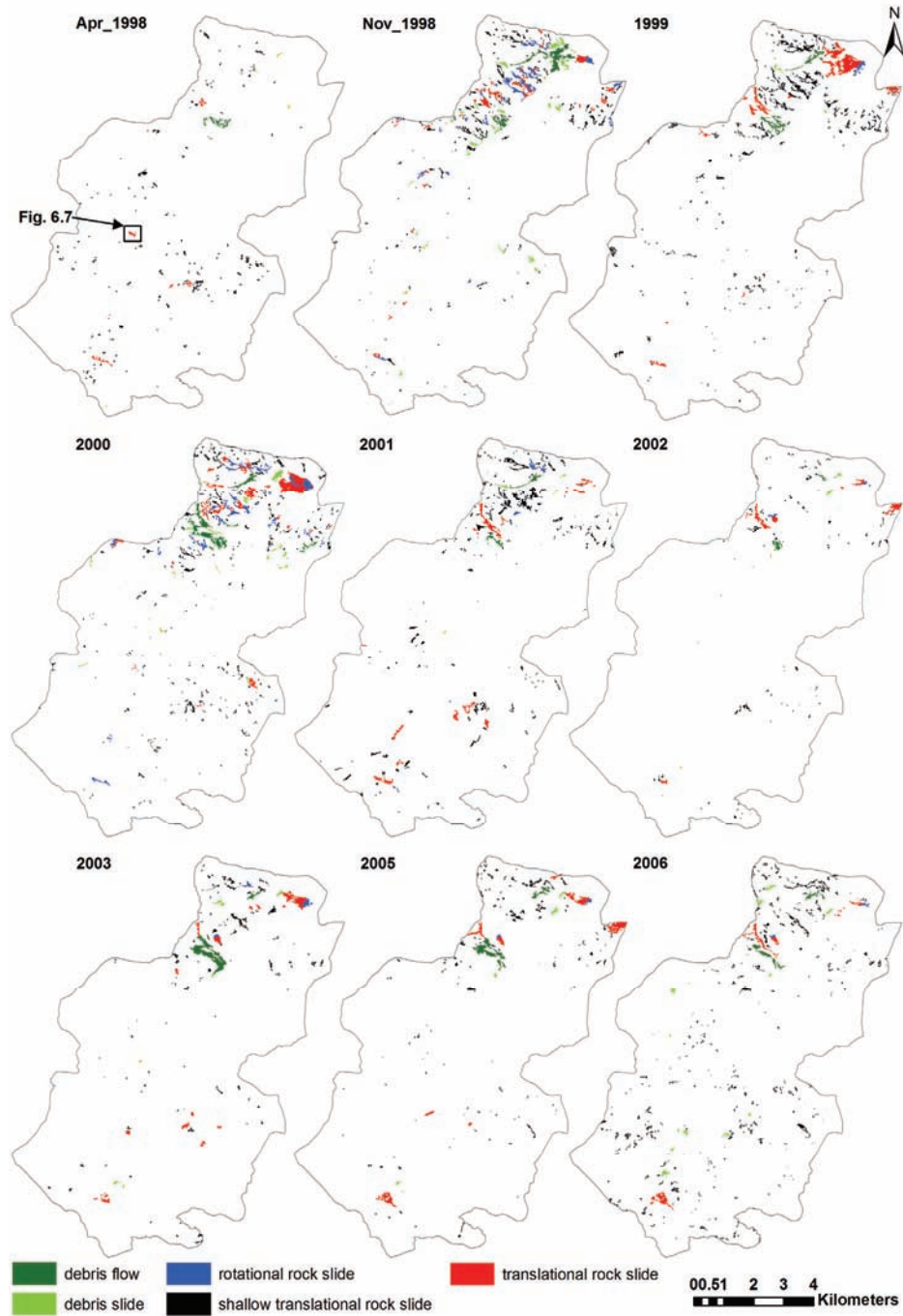


**Figure 6.6:** Independent annual inventory of landslides of five different types prepared from historical panchromatic images (1998 – 2006) in the Okhimath area by OOA.

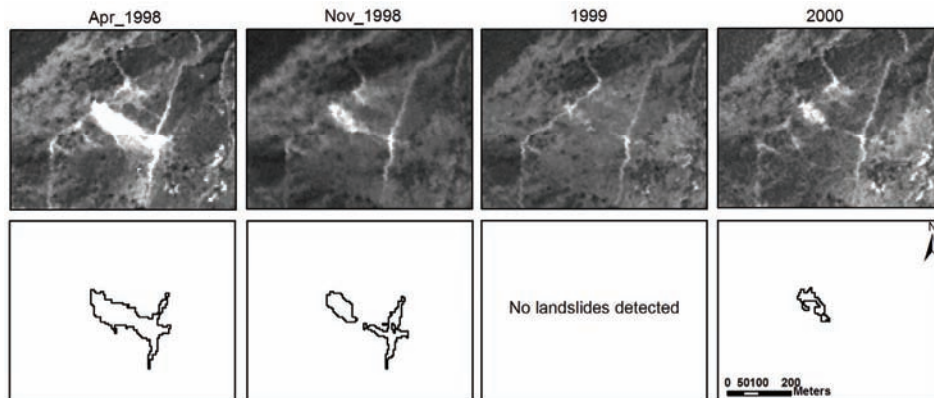


**Figure 6.7:** Monitoring of an active landslide. The location of this landslide is shown in figure 6.6. There is a decrease in the landslide-affected area from April to November, 1998, which is showing no activity in 1999. The reactivation has started again in 2000.

Accuracy figures for all five types of landslides for the years 1998 to 2006 are provided in figure 6.8. From the figure 6.6, it is evident that shallow translational rock slides are the dominant landslide types in terms of total number in all the years. In this semi-automatic method, 86.9% of the total number of shallow translational landslides that occurred after the super event of August 1998 could be recognised correctly from the 02 November 1998 image, which is the maximum in comparison to other years. The accuracy of the total extent of the correctly recognised shallow translational rock slide from the same image is 95.7%, which indicates that the inventory will be very useful for preparing landslide susceptibility map by data driven models. Accuracy of the extent of the shallow translational rock slide recognised correctly is reasonably good for all the years except for the year 2000 (60%) (Figure 6.8). Also the percentage of shallow translational rock slides incorrectly recognised is particularly high in 2006. This is due to the incorrect identification of some of the shallow translational rock slides as agricultural lands.

Translational rock slides are the second most dominant type of landslide in this area (figure 6.6). The accuracy of the total extent of translational rock slide correctly recognised from the 02 November 1998 image, i.e. those corresponding to the super event, is 64.7%. Although the accuracy of the number of translational rock slide correctly recognised is reasonably good in all the years, the accuracy of extent varies from 48% (for 2001) to 82.2% (for 2003). This is mainly due to incomplete identification of large landslides, although they occurred after the super event. The incomplete identification of large landslides can be attributed to; i) part of them being completely under shadow due to low sun position during data acquisition, and ii) large part of

*Multi-temporal inventory*

the left flank of some landslides not being illuminated sufficiently. Therefore, they were wrongly identified as agriculture and barren land (Figure 6.9b). However, this large landslide was better identified from the 28 May 2000 image due to proper illumination of the landslide under high sun position.

The performance of the methodology to correctly recognise debris flow, debris slide and rotational rock slide is moderately good. The total number and extent of these landslides incorrectly recognised, i.e. error of commission, is significantly high in comparison to those incorrectly recognised from multi-spectral images. Among all landslide types, the extent of debris slides over detected from the 28 May 2000 image is very high (827%). This is mainly due to incorrect identification of channel deposits as debris slides.

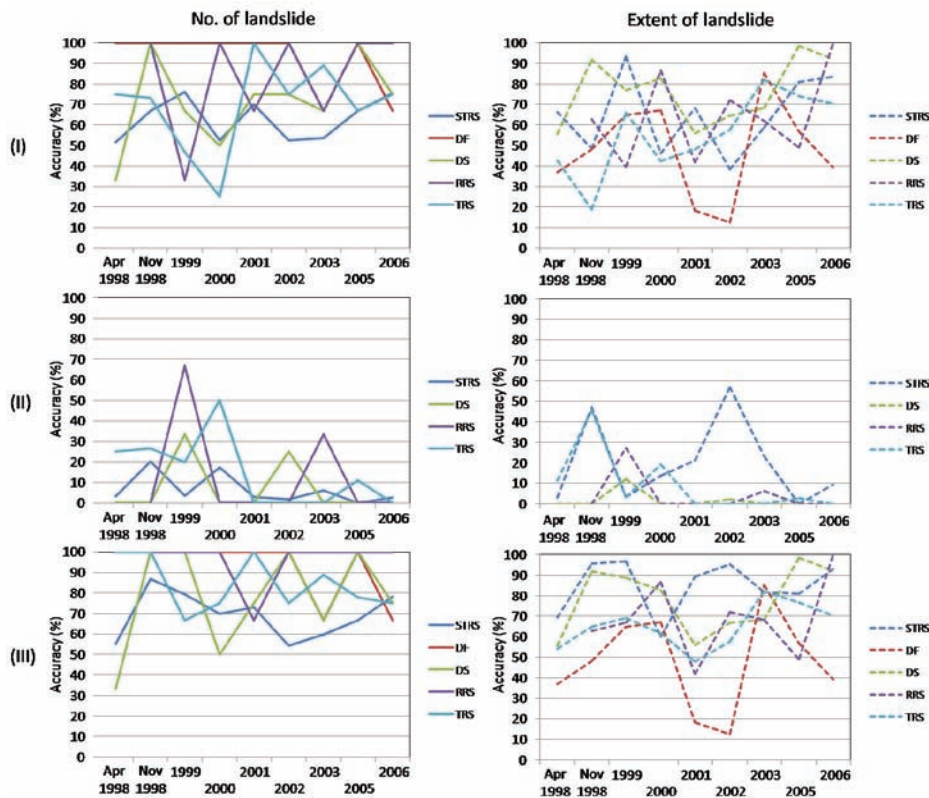


**Figure 6.8:** Accuracy assessment for number and extent of landslides of different types having correctly classified (I), incorrectly classified (II), correctly recognised (III), not recognised (IV) and incorrectly recognised (V). STRS - shallow translational rock slide; DF - debris flow; DS - debris slide; RRS - rotational rock slide and TRS - translational rock slide.

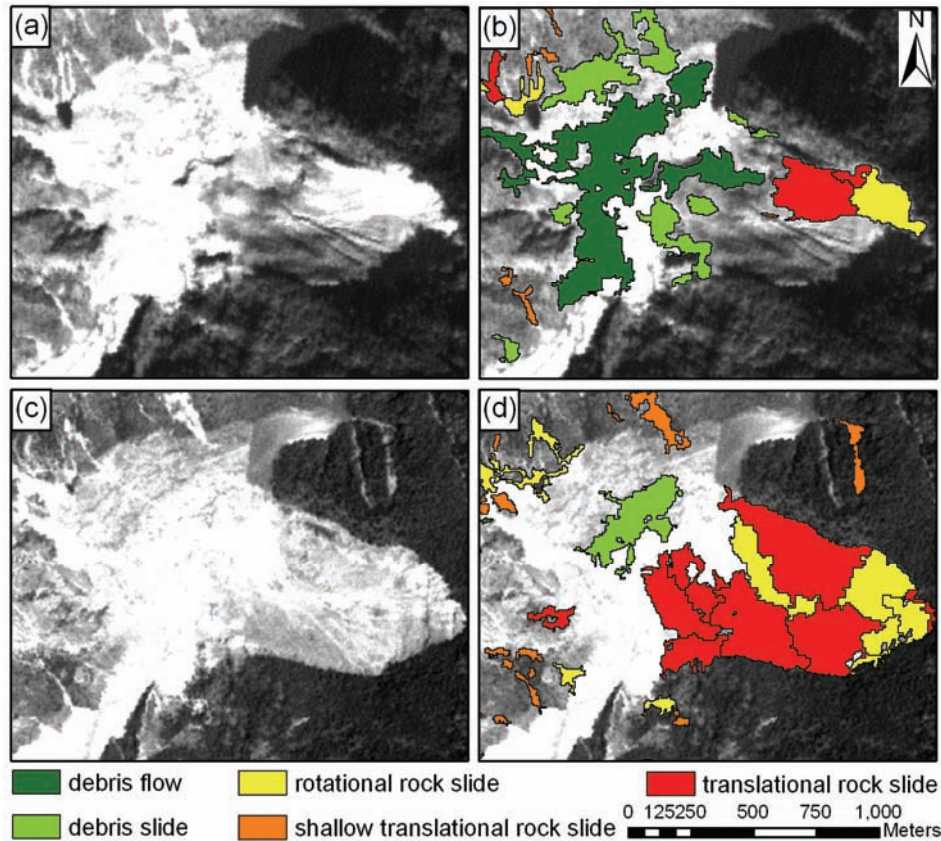


**Figure 6.9:** Detection of translational rock slide from panchromatic images. (a) post-landslide image (02 November 1998), (b) parts of translational rock slide, although correctly recognised, wrongly classified into multiple debris slides and debris flows, (c) post-landslide image (28 May 2000), and (d) translational rock slide that was better identified due to proper illumination.

#### 6.3.4.1 Comparing landslide density

Another means of assessing accuracy of multi-temporal landslide inventory is by comparing the density of slope failures in inventories (Galli et al., 2008). For this purpose the study area was divided into terrain units having similar slope conditions. Terrain units or slope facets, which have consistent slope direction and inclination, and are generally delimited by ridges, spurs and gullies (Anbalagan, 1992), were prepared manually with the help of hillshade, slope and aspect derived from the DTM. A total of 1982 slope facets was prepared and landslide density was calculated by intersecting the landslide polygons of the historical landslide inventories identified by manual and semi-automatic methods with the slope facet map. The spatial distribution of landslide density classes shown in figure 6.10 is well correlated. Slope facets with a landslide area < 3% were considered as stable (Galli et al., 2008). An

error matrix was created for comparing the two sets of landslide inventories (Table 6.4). The overall accuracy of the semi-automatically prepared landslide inventory in terms of landslide density is 93.4% with a *Kappa* coefficient of 0.842. It indicates that, although the individual semi-automatically prepared landslide inventories independently show accuracies in the range of 37 – 100% (Figure 6.8), collectively they showed a high degree of accuracy due to which the overall accuracy of the landslide density is very high.

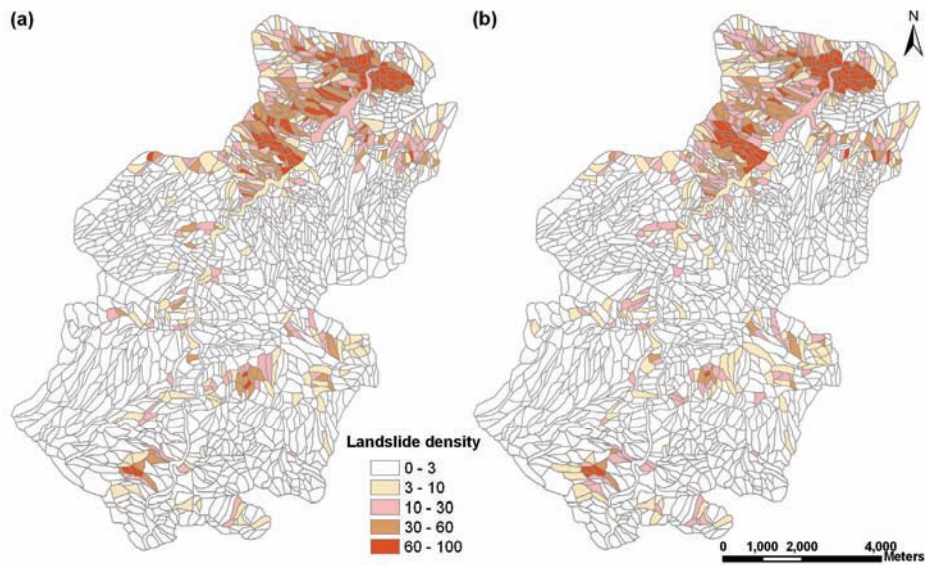


**Figure 6.10:** Comparison of landslide density (a) with semi-automatically identified landslides, and (b) with manually identified landslides.

**Table 6.4:** Comparison of stable and unstable slope facets based on semi-automatic and manual landslide inventories.

		Density map obtained from manual inventory		
		Stable	Unstable	Total
Density map obtained from semi-automatic inventory	Stable	1335	75	1410
	Unstable	55	517	572
	Total	1390	592	1982

## **6.4 Conclusion**

A historical landslide inventory is a primary requirement for the preparation of a landslide hazard map by statistical methods, for which multi-temporal satellite images or aerial photographs are mainly used. These images are often only available in greyscale. In this chapter we presented an object-oriented method to prepare historical inventories from archived panchromatic images (1998 – 2006) in the Himalayas. Recognition and classification of landslides were attempted using a knowledge-based method as discussed in the previous chapters. GLCM texture measures were extensively used to identify false positives using multiple optimal scales derived from POF. However, the number of false positive types in panchromatic images is less in comparison to what had to be eliminated during landslide detection from multi-spectral images (Table 5.2). Object-based change detection for the identification of landslides from grey scale imagery was presented for the first time in this dissertation and was found to be very useful for the identification of large landslides. Small size landslides were also recognised by change detection technique due to accurate geometric registration ( $< 3$  pixel RMS error) of the multi-temporal images, which was mainly achieved due to the use of low sensor tilt angle images. The use of a local instead of global brightness threshold was also very effective, particularly for the detection of smaller translational rock slides, and can be considered as a significant achievement of this study. The maximum (86.9%) recognition accuracy for the total number of shallow translational rock slides can be attributed to this factor.

The recognition accuracies of shallow translational rock slides and translational rock slides are reasonably good and comparable to the accuracy figure obtained from the multispectral image. However, the percentage of wrong detection is also high in comparison to the accuracy figures obtained in the previous chapters, i.e. more features, such as agricultural and barren lands, were incorrectly identified as landslides from panchromatic images. Therefore, one level of external quality checking for the identification of agricultural lands, which are relatively easy to identify by onscreen visual interpretation, is required before the landslide inventories prepared from grey scale images are used as an input for landslide susceptibility and hazard mapping. This step is reasonable, since historical inventory need not be done very quickly, compared to the preparation of current or new inventory. The landslide density map prepared from semi-automatically prepared landslide inventories showed a good spatial fit with the density map generated using manually prepared landslide inventories. Also, the overall accuracy of the stable and unstable areas derived using manually and semi-automatically prepared landslide inventories was 93.4%, which indicates a significant level

### *Multi-temporal inventory*

---

of matching between the two sets of inventories, when the multi-temporal inventories were analysed collectively.

In this approach, a knowledge about the number of false positive classes present in the study area and the assignment of scale factors to them based on a sample area analysis has worked well for identification of most of the false positives in this as well as in the previous chapter. However, this subjectivity in assignment of scale factor to a false positive can be solved by creating a standard spectral-spatial land cover database vis-a-vis scale factor for landslide susceptible areas. Once the database is created, it can be used for detection of landslides in future unless there is a major change in the land use / land cover. The main limitation of this study is the interactive selection of GLCM textures. This was required to identify and eliminate some of the false positives from landslide candidates. Another limitation is that the threshold values of the textures were also selected interactively, unlike done statistically using K-means clustering method.

### ***Acknowledgements***

Authors thank A. Lesslie and M. A. Jeelani scientists in RSGIS-AA, NRSC for discussion pertaining to landslide density and reflectance calculations, respectively.

## **Chapter 7: Use of semi-automatically derived landslide inventories in hazard and risk assessment<sup>\*</sup>**

One of the primary uses of landslide inventories is the preparation of landslide susceptibility and hazard maps. In this chapter we show how landslide inventories prepared by semi-automatic methods from post-event satellite images can be used in the assessment of landslide susceptibility, hazard and risk.

### **7.1 Introduction**

The availability of landslide hazard and risk maps is essential to identify the potential areas of landslide losses and to minimise its societal impact. One of the first steps in this direction is the preparation of a landslide susceptibility map, indicating the relative susceptibility of the terrain for the occurrence of landslides. When combined with temporal information this can be converted into a landslide hazard map, which can be used in combination with elements at risk information for estimating potential losses to landslides in future, and will aid long term landslide risk management in mountainous areas.

A landslide inventory is the basis for any landslide hazard and risk assessment (Brardinoni et al., 2003; Carrara and Merenda, 1976; Guzzetti et al., 2000). A typical landslide inventory map gives information about the type, volume, magnitude, date and place of occurrence. Landslide inventories can be used for the calculation of weights of the pre-disposing factor maps during landslide susceptibility mapping, as well as for performance and reliability analysis in prediction modelling (Carrara and Merenda, 1976; Guzzetti et al., 2000) and in magnitude and frequency analysis for the hazard mapping. However, preparation of landslide inventory by manual methods is a substantial challenge as it requires time and a team of experienced people. According to an estimate by Galli et al. (2008), preparation of a inventory took an average one month per interpreter to cover 100 km<sup>2</sup> area in the Umbria region of Italy. Alternatively, landslide inventories can be prepared by automatic methods by incorporating expert knowledge in the image analysis (Barlow et al., 2006; Martha et al., 2010b; Moine et al., 2009).

Preparation of automatic landslide inventories can be comparatively fast, unbiased and data driven, particularly with object-oriented analysis (OOA)

---

<sup>\*</sup> This chapter is based on the article: Martha, T.R., van Westen, C.J., Kerle, N., Jetten, V.G. and Kumar, K.V. (2011) Landslide hazard and risk assessment using landslide inventories created semi-automatically by object-oriented analysis. *Journal of the Geological Society of India* (In revision).

methods, the outputs are also visually consistent. Recently, Martha et al. (2010b) updated landslide diagnostic features using high resolution satellite data and a digital elevation model (DEM), and synthesised them using OOA for mass failure detection. They not only detected landslides accurately but also classified them into translational rock slide, rotational rock slide, shallow translational rock slide, debris flow and debris slide using a semi-automatic method. The recent literature shows that many attempts have been made around the globe to prepare landslide hazard maps using manually identified landslides (Guzzetti et al., 2005; Pradhan, 2010; van Westen et al., 2003). Several attempts were made for automatic detection of landslides (Barlow et al., 2006; Borghuis et al., 2007; Martha et al., 2010b; Nichol and Wong, 2005b; Rosin and Hervas, 2005). However, to the best of our knowledge, no attempt has been made to validate the effect of such inventory on landslide hazard and risk assessment. This will also demonstrate the potential of semi-automatically detected landslides for preparation of landslide susceptibility and hazard map using statistical methods, which could not be achieved so far in many developing countries due to lack of systematic landslide inventory. Although it is implicit that the automatic detection of landslides has great potential for short term goals such as damage assessment after a disaster, evaluation of such outputs to achieve long term goals, such as hazard and risk assessment, is worth doing.

The objective of this chapter is to use the multi-temporal landslide inventories, created using OOA, in assessing landslide susceptibility, hazard and risk. In chapter 6, time-series images from high-resolution Cartosat-1 (2.5 m), Resourcesat-1 LISS IV Mx (5.8 m) and IRS-1D panchromatic (5.8 m) were used to map active landslide areas in the study area (Figure 1.3). One image per year from these satellites was procured from the data archives, and processed by OOA using the methods shown in chapters 5 and 6 to prepare a landslide inventory from 1997 to 2009 period. These multi-temporal inventories in combination with historical rainfall data were used to estimate the spatial and temporal probabilities for hazard assessment. The hazard map was then integrated with elements at risk map prepared from the satellite image to assess the landslide risk.

## **7.2 Methodology and data**

The methodology adopted in this chapter for landslide susceptibility, hazard and risk assessment is briefly explained in figure 7.1. The data used and details of methodology are explained in the following sub-sections.

### **7.2.1 Preparation of multi-temporal landslide inventory**

The knowledge-based semi-automatic method as explained in detail in chapters 4, 5 and 6 was used for preparation of multi-temporal landslide inventory map. So far, we have shown landslide inventory maps for the years 2004 and 2007 in chapters 4 and 5 respectively, and for the years from 1998 until 2006 (except 2004) in chapter 6. In order to prepare the landslide inventory for the years 2008 and 2009, we additionally processed two Resourcesat-1 LISS-IV multispectral images corresponding to those years, using the method explained in chapter 5.

We used two images corresponding to the year 1998 (Table 6.1). The results obtained from the image dated 14 April 1998 can be assumed as the inventory corresponding to show the landslides triggered during the monsoon of 1997, since July and August are the wettest months in this area, where rainfall is the major triggering event (Figure 7.2). Thus we have a continuous landslide inventory with annual landslide inventories for 13 years (from 1997 to 2009). However, the landslide inventories prepared by semi-automatic methods, particularly those prepared from panchromatic images, sometimes have a high error of commission, i.e. non-landslide areas were falsely identified as landslides (Table 6.4). Therefore, such polygons were removed through an onscreen visual inspection by superimposing landslide inventory layers on respective images.

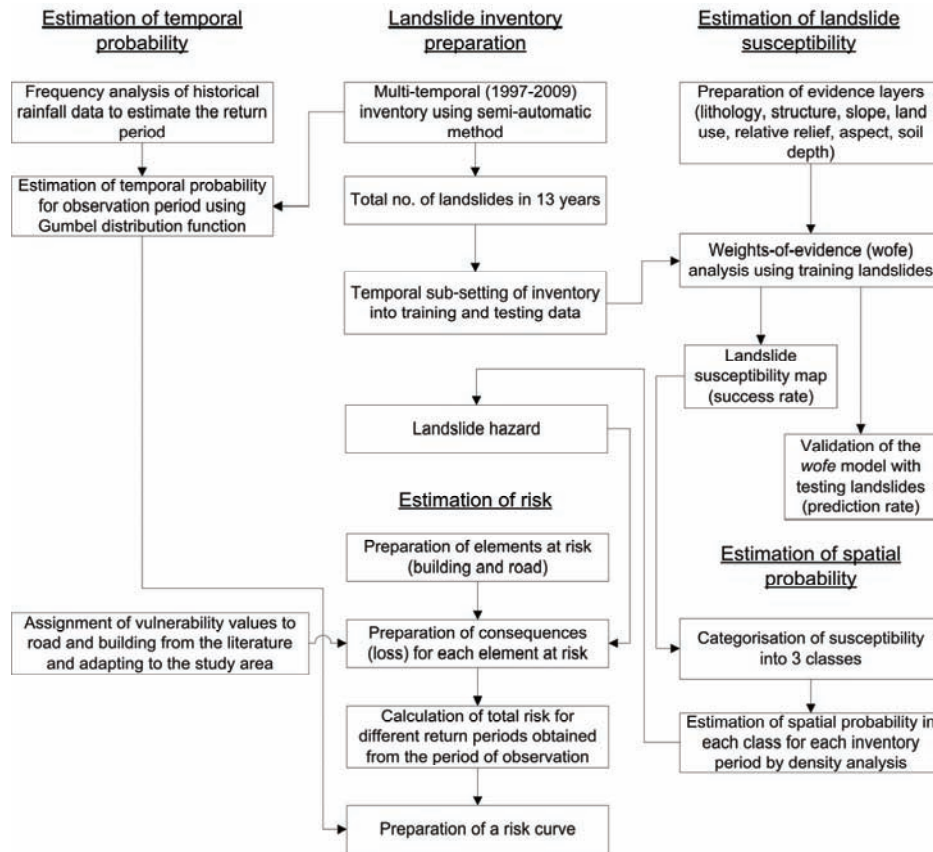


**Figure 7.1:** Procedure for landslide hazard and risk assessment using semi-automatically prepared landslide inventory maps.

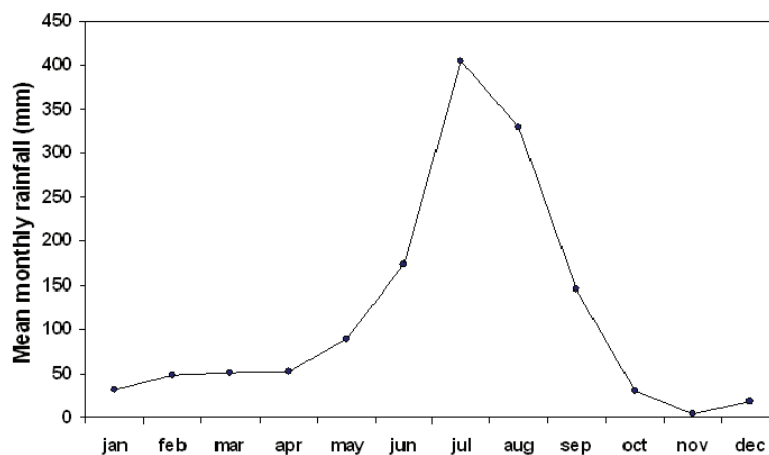


**Figure 7.2:** Mean monthly rainfall pattern in the study area for 34 years (1976 – 2009). Source: Central water commission, Dehradun, India.

## 7.2.2 Generation of landslide susceptibility map

One of the first and most important steps involved in landslide hazard mapping is the assessment of landslide susceptibility, which indicates the spatial distribution of localities that are favourable for future occurrence of landslides. The susceptibility map shows the proneness of an area to landslides. The susceptibility map can be prepared in a GIS using statistical, heuristic or physically-based methods. With heuristic methods weights are assigned to the predisposing factors also known as causative factors or evidence layers, based on the experience of the experts, whereas in data driven statistical techniques weights are obtained by correlating landslide occurrences and evidence layers, using both univariate and multivariate methods. Commonly used bivariate methods are information value and weights-of-evidence modelling in which weights for each parameter are derived from the landslide inventory (Mathew et al., 2007). Since the objective of this chapter is to verify the effectiveness of semi-automatically prepared landslide inventory in deriving weights for evidence layers, which has an implicit bivariate relationship with landslide occurrence, the proven weights-of-evidence method was preferred over other bivariate and multivariate methods.

### 7.2.2.1 Input data

Data sources used for the preparation of evidence layers, which are the most important contributing factors for the occurrence of landslides in the Himalayas, are provided in table 7.1. The available geological map was used to refine the boundary between the rock types, particularly the boundary between quartz sericite schist and quartz mica schist, gneiss and amphibolite, and between the later and streaky banded augen gneiss using the break-in-slope criteria (Figure 7.3a). The area is traversed by two major thrusts, namely the Main Central Thrust (MCT-II) that passes just south of Okhimath, and the Vaikrita Thrust (also known as MCT-I) that passes north of Okhimath (Figure 7.3a). Geologically it is a disturbed area. The MCT is a nearly 10 km wide shear zone, inclined at 20° to 45° northward. Foliations dip at moderate angles in NE to NNW directions (Naithani, 2002; Naithani et al., 2002). While thrusts and faults were derived from available geological map, lineaments were interpreted from LISS-IV Mx and hillshade images (Figure 7.3a). Finally, geological structure (lineaments, faults and thrusts), which is a line layer, was converted to a polygon layer using a variable buffer criterion, since the lineament has very narrow zone of influence on the strength of the rock in comparison to a thrust, which has larger zone of influence. Slope facets were used as zones to derive relative relief using elevation information from the DEM (Figure 7.3b). Land use and land cover in this area is not dynamic. There were also no reports of forest fire, urbanisation or major change in

agricultural practices that can have a potential impact on the change of land cover. The landslides in this area are due to excessive rainfall and not due to the change in land use / land cover (Naithani, 2002). Therefore, we selected the first multispectral image in the observation period, i.e. a LISS-IV Mx image of 2004, to prepare the land use / land cover map of this area. The soil in this area is transported and composed of sub-angular rock fragments with a high proportion of sandy to sandy-silty matrix (Naithani, 2002; Naithani et al., 2002). Soil depth, which is an important parameter for the creation of landslide susceptibility map, was prepared using an available soil map. These evidence layers were verified during the field work. The slope angle was derived from the DEM and was classified into 10 classes using a quantile classification system. Slope aspects have a significant role for the occurrence of landslides in the Himalayas. It is observed that south facing slopes are preferable among locals for development of settlement and agriculture since they are sun lit for maximum duration in a day. This results in an increase in anthropogenic activities in such areas, and sometimes results in the destabilisation of slopes. Therefore, slope aspects derived from DEM were used for the creation of susceptibility map. Relative relief is another important parameter for the initiation of landslides. It was derived from the DEM using the zonal statistics tool of ArcGIS, wherein slope facets are used as zones. Slope facets or terrain units, which have more or less similar characters of slope showing consistent slope direction and inclination, and are generally delimited by ridges, spurs and gullies (Anbalagan, 1992), were prepared manually with the help of hillshade, slope and aspect.

**Table 7.1:** List of evidence layers and their sources used to derive landslide susceptibility.

Evidence layers	Number of classes	Data sources
Lithology	4	Updated using Resourcesat-1 LISS-IV Mx and DEM
Geological structure	2	Resourcesat-1 LISS-IV Mx and Hillshade
Soil depth	4	Available soil map
Land use / Land cover	8	Resourcesat-1 LISS-IV Mx
Slope angle	10	DEM
Slope aspect	9	DEM
Relative relief	5	DEM and slope facet

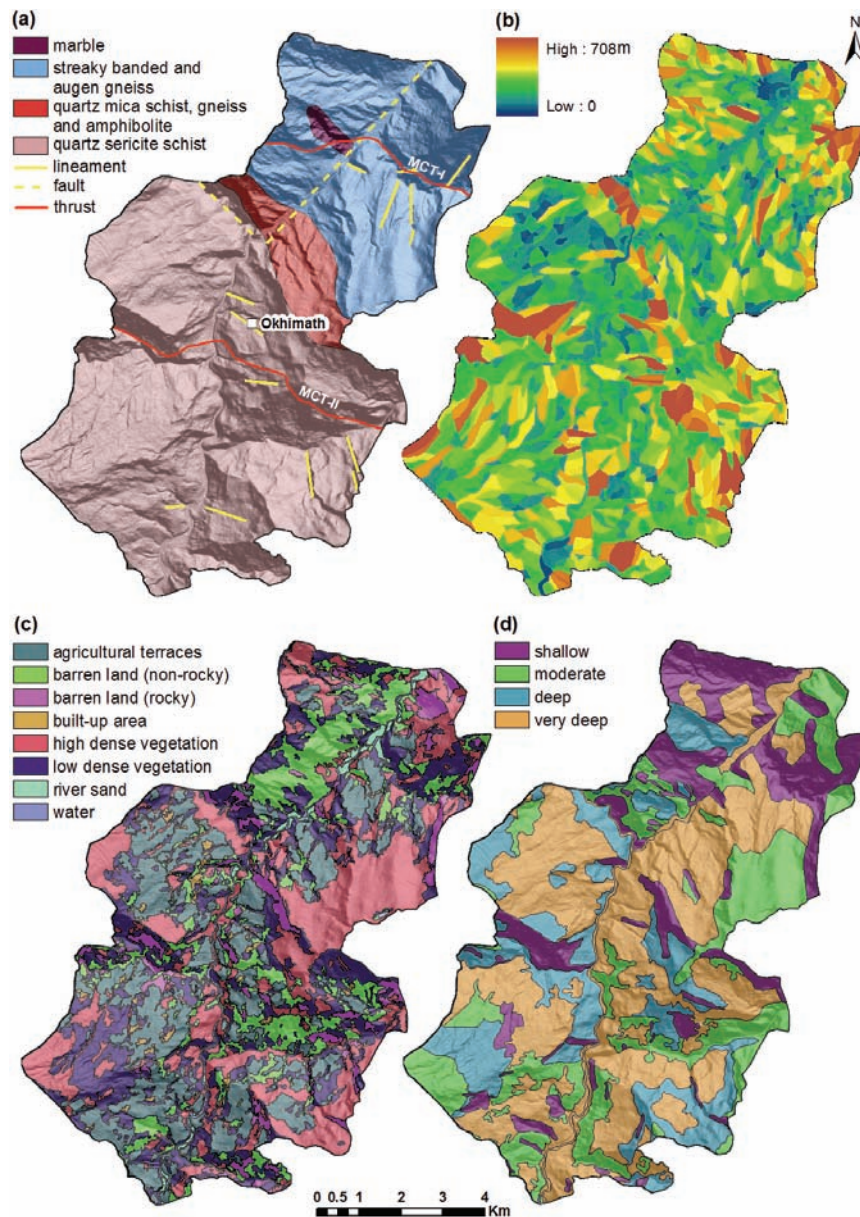


**Figure 7.3:** Some of the important evidence layers used for preparation of landslide susceptibility map. (a) lithology and structure (updated using quadrangle geological map published by GSI), (b) relative relief, (c) land use / land cover and (d) soil depth.

### 7.2.2.2 Weights of evidence (wofe) method

The method 'weights-of-evidence', or *wofe*, was initially developed for the identification and exploration of mineral deposits using borehole or geochemical data (Bonham-Carter et al., 1989; Carranza and Hale, 2003).

Many researchers, such as Mathew et al. (2007), Neuhäuser and Terhorst (2007), Poli and Sterlacchini (2007), Thiery et al. (2007) and Ghosh et al. (2009), have used it also for landslide susceptibility assessment. In this method, historical landslides are used to calculate weights of evidence layers to demarcate future areas of landslides under the assumption that similar factors will prevail in future also (Neuhäuser and Terhorst, 2007). The main assumption of *wofe* is that the evidence layers are independent of each other. Although it may not be true in all cases, *wofe* nevertheless provides relatively easy and understandable results, and is therefore often used as an exploratory tool in susceptibility assessment. *wofe* is based on the concept of prior and posterior probability. The probability determined empirically with knowledge about the occurrence of an event (e.g. landslide) in the past under equal condition is known as prior probability. When evidences such as lithology, land use, slope are integrated into calculation of probability, it is known as posterior probability (Neuhäuser and Terhorst, 2007). By overlaying landslide locations with each evidence layer, the statistical relationship can be measured between them. This will help in assessing the significance of an evidence layer for the occurrence of past landslides. A pair of weights, i.e.  $W^+$  and  $W^-$ , is calculated for each layer, which are dependent on the spatial relationship between the landslides and evidences. This calculation is done by applying likelihood ratios, which describe the probability of occurrence of landslides in the presence and absence of evidences. The end product of this analysis is a map showing the relative proneness of the terrain to produce landslides i.e. landslide susceptibility, based on certain evidences.

In this study, we used ArcSDM software, a geoprocessing tool of ArcGIS 9.3.1 for *wofe* analysis (Sawatzky et al., 2009). This software automatically calculates positive and negative weights ( $W^+$  and  $W^-$ ) depending on the association between the response variable (landslides) and each class of predictor variables (evidence layers). The contrast (C) and studentised contrast (sC) calculated by the software are useful to understand the spatial association of each class of predictor variables and response variable (Poli and Sterlacchini, 2007). Since the software accepts response variable as points, the landslide inventory created as polygons were converted to grids (50 m x 50 m) using the method applied by Poli and Sterlacchini (2007). Subsequently, the inventory grids were converted to points, resulting in representation of one landslide by a number of points depending on its size. One of the common and frequently used practices in landslide modelling is to develop a model using one time period inventory and validate it with the inventory of the next time period. Therefore, a temporal sub-setting of the landslide inventory database was made to create the training and testing

data for *wofe* analysis. Landslide inventories up to the year 2004 were treated as training data, whereas those from 2005 until 2009 were treated as testing data. While the training points were used to calculate the weights of the evidence layers, testing points were used to validate the usefulness of *wofe* model in predicting future landslides.

### 7.2.3 Landslide hazard assessment

After the susceptibility map was prepared, the next step was to assess the landslide hazard. This was done by calculating the temporal probability of landslide occurrence within the spatially favourable landslide areas. To estimate the spatial and temporal probabilities, annual landslide inventories prepared by the semi-automatic method and historical rainfall data were used.

#### 7.2.3.1 Estimation of spatial probability

Firstly, the landslide susceptibility map was classified into high, moderate and low susceptibility categories using the success rate curve of the *wofe* model. Then, the spatial probability corresponding to each inventory year and for all the three susceptibility class was calculated separately by ratioing the areas using the following equation:

$$\text{Spatial probability} = \frac{A_{\text{landslide}}}{A_{\text{susceptibility class}}} \quad (7.1)$$

#### 7.2.3.2 Estimation of temporal probability

Landslides in the Himalayas are mostly triggered by extreme events such as rainfall, and the frequency of such extreme events is inversely related to its return period. We used the annual maximum rainfall amount over 34 years (1978 - 2009) for an extreme events frequency analysis using the method described by Gumbel (1958), which is used frequently in hydrological applications (Jaiswal et al., 2011). The Gumbel extreme model can be applied to model the probability of occurrence of the number of landslides ( $N_L$ ) equal to or less than some value  $n$ . The model can be expressed as:

$$P(N_L \leq n) = e^{-e^{-(\alpha+n)/c}} \quad (7.2)$$

where  $\alpha$  and  $c$  are two parameters of the Gumbel distribution. By the method of moments, the parameters are evaluated as (Chow et al., 1988)

$$\alpha = \gamma c - c \quad (7.3)$$

$$c = \frac{\sqrt{6}}{\pi} \sigma \quad (7.4)$$

where  $\gamma=0.57721$  is a Euler's constant,  $\mu$  is the mean, and  $\sigma$  is the standard deviation. For a specified time interval in a year, equation 7.2 can be rewritten for the value ( $N_L$ ) equal to or greater than some value  $n$  as:

$$P(N_L \geq n) = \frac{1}{T} = 1 - e^{-e^{-(\alpha+n)/c}} \quad (7.5)$$

where  $T$  is the return period. Two methods are commonly used for fitting distributions to the Gumbel model for frequency analysis; i) the plotting position method, and ii) the frequency factor method. The former is a simple plotting method to obtain the distribution function by the use of certain "plotting position" formula (Chow et al., 1988). The technique used is to arrange the data in increasing or decreasing order of magnitude and to assign order number  $R$  to the ranked values. The Weibull formula is commonly used to obtain the plotting position, which for  $P(N_L \geq n)$  can be expressed as:

$$P = \frac{R}{m+1} \quad (7.6)$$

where  $R$  is the rank and  $m$  is the total number of observations. When  $R$  is ranked from lowest to highest,  $P$  is an estimate of  $P(N_L \leq n)$ ; when the rank is from highest to lowest,  $P$  is  $P(N_L \geq n)$ . Equation 7.6 can be plotted on a probability paper to represent the cumulative probability distribution. The graph is designed in such a way that it gives the return period for a magnitude of event. In this study,  $m=34$ . The rainfall values were ranked from low to high, with lowest rank (1) assigned to the lowest rainfall value and highest rank (34) assigned to the highest rainfall value. Using the plotting position method, the data were plotted on a probability paper and a curve was fitted to the plotted points. Then the return period of the rainfall event related to the landslide inventory period (1997 - 2009) was measured from the fitted curve.

#### **7.2.4 Landslide risk assessment**

Landslide risk can be defined as the expected number of lives lost, persons injured, damage to properties and disruption of economic activities due to landslides for a given area and reference period (Varnes, 1984). The concept of risk that has been applied to landslide studies can be expressed by the following generic equation (van Westen et al., 2006; Zêzere et al., 2008).

$$\text{Landslide risk} = \text{Landslide hazard} \times \text{Vulnerability} \times \text{Elements at risk} \quad (7.7)$$

In the previous section we have explained how landslide hazard can be estimated quantitatively. Elements at risk in equation 7.7 refer to the people,

buildings, civil engineering works, economic activities, public services, utilities and infrastructure that are at risk in a given area from landslides. However, elements at risk considered in this chapter include only buildings and roads, which were mapped through visual interpretation of high resolution images. Other types of damage (e.g. indirect damage, damage to population and vehicles) are very difficult to estimate, and are not considered in this study due to lack of data.

Most of the houses in the study area are confined to two localities i.e. Okhimath and Guptakashi. The houses in these two localities are reinforced with concrete and well constructed due to local business opportunities. Other parts of the study area are in a rural environment with small isolated patches of houses, which are not very well constructed. It is not possible to map the daily movement of population or the no. of people living in each house for such a large area. Therefore, the risk assessment was carried out for houses and not for population. Vulnerability is possibly the most difficult term to represent quantitatively within landslide risk analysis (van Westen et al., 2008; Zézere et al., 2008). Vulnerability depends on landslide type, magnitude and type of risk element exposed, and its estimation requires data of past damage. It varies from 0 to 1, with 1 representing total damage. Reliable estimate of vulnerability for a specific element at risk is rare and literature recommends some vulnerability for a particular condition (Bell and Glade, 2004; Glade, 2003). Considering the landslide type in this area and consulting the literature, vulnerability values between 0.3 to 1 were assigned to the different types of building (Castellanos Abella, 2008). The cost of the building and the vulnerability were assigned to each house and they were multiplied on cell by cell basis with spatial probability to estimate the risk to the building for a given return period.

This area has a good road network. The national highway (NH-109) passing through this area have maximum vehicular movement. District roads connect the highway to the settlements in the valley. All roads are tar covered. Vulnerability values of 0.5 and 0.8 were assigned to the highway and district road, respectively, based on the literature and by adapting to the study area (Castellanos Abella, 2008). Vulnerability was multiplied with the spatial probability on a cell by cell basis, the sum of which for a given return period was further multiplied with the cost to estimate the risk to the road.

Total risk for a given return period was calculated by summing up the risk to the building and road. In this manner landslide risk for the complete observation period was estimated separately. Finally, a risk curve was plotted

between the temporal probability and consequences to estimate any loss in future for a given return period.

## **7.3 Results and discussion**

### **7.3.1 Landslide susceptibility assessment**

Using ArcSDM software, *wofe* analysis was performed. A total of seven evidence layers and 2137 response variables, i.e. landslide points in a 50 x 50 grid corresponding to the inventory from 1997 to 2004, were used to calculate the weights. The evidence layers were converted to a 10 x 10 grid for *wofe* analysis, since a 10 m DEM was used in this study for derivation of the topographic layers.

Weights and contrast values represents a measure of correlation.  $W^+ > 0$  and  $W^- < 0$  indicates landslide locations are positively correlated with evidence layers, where as  $W^+ < 0$  and  $W^- > 0$  indicates negative spatial association between evidence layer and landslide location (Neuhäuser and Terhorst, 2007). Figure 7.4 shows a comparison of contrast values ( $W^+ - W^-$ ) of all evidence classes. This is an important measure of correlation between the landslide locations and evidence layers. Table 7.2 summarises only the evidence classes that are positively correlated and are important indicator of landslide occurrence. Although the slope classes from  $13^\circ$  to  $89^\circ$  have a consistent contrast, the sC values of the slope from  $21.5^\circ$  to  $41^\circ$  are relatively high compared to other classes, which show that these slopes are the most significant for the occurrence of landslides. Among the lithological units, streaky banded and augen gneiss has the highest sC value. This unit, which is mainly exposed in the Madhyamaheswar valley along with the MCT, is responsible for high occurrence of landslides. Non-rocky barren land has both the highest contrast (Figure 7.4) and sC (Table 7.2), which indicates that it is the most critical land use class for the occurrence of landslides. South facing slopes are known for their landslide proneness in the Himalayas. This was brought out clearly by the *wofe* model since it has only shown positive correlation among all other aspect classes. Areas with high relative relief in the Himalayas are mostly exposed as rocky escarpment consisting of hard rock and are mostly stable. Therefore, only low relative relief areas have shown positive correlation with landslides.

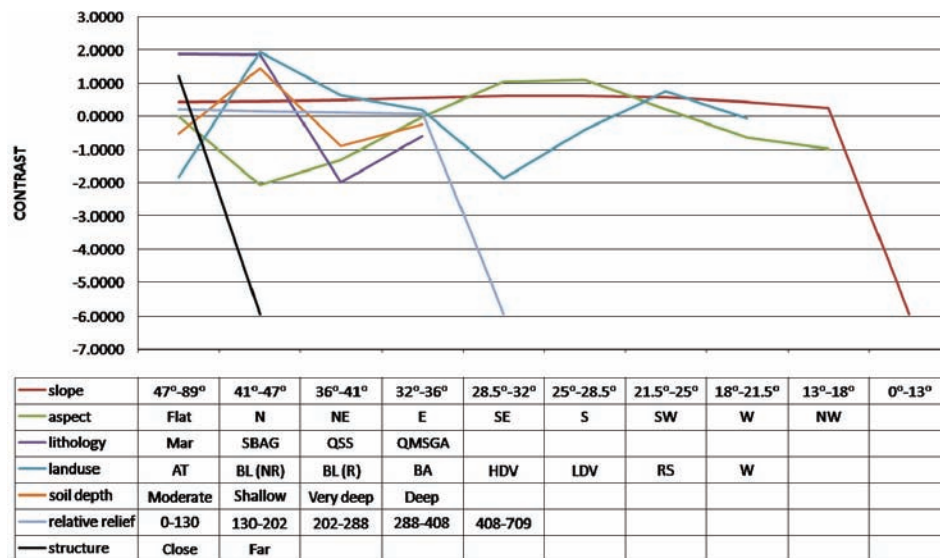


**Figure 7.4:** Contrast values for all classes of the seven evidence layers. Lithology (Mar: Marble, SBAG: streaky banded and augen gneiss, QSS: quartz sericite schist, QMSGGA: quartz mica schist, gneiss, amphibolite), Landuse (AT: agricultural terraces, BL (NR): barren land (non-rocky), BL (R): barren land (rocky), BA: built-up area, HDV: high dense vegetation, LDV: low dense vegetation, RS: river sand and W: water).

Finally, the overlay of all weighted factors and the calculation of the total posterior probability were carried out. The cumulative percentage of landslide location was plotted against the cumulative percentage of the area to create a success rate curve in order to classify the study area for landslide susceptibility. Figure 7.5 shows the success rate curve in which two inflection points were identified for classifying the area into three classes. The first inflection point is at 67.6 cumulative percentage of all landslides, corresponding to 14.7 cumulative percentage of the total study area. The posterior probability value corresponding to this inflection point is 0.007984 and was used as threshold for classification of the study area into high susceptible category. The second inflection point is at 96.9 cumulative percentage of all landslides, corresponding to 49.5 cumulative percentage of the total study area. The posterior probability value corresponding to the second inflection point is 0.000227. The grids having posterior probability values between 0.000227 and 0.007984 were classified into moderate susceptibility category. It means 67.6% and 29.3% of all landslides and 14.7% and 34.8% of the total study area are in the high and moderate susceptibility class category. Remaining part of the study area is in the low susceptibility category (Figure 7.6).

**Table 7.2:** List of evidence classes showing positive correlation. Studentised contrast (sC) is a measure of the significance of the correlation.

Evidence layer	Class	W <sup>+</sup>	W <sup>-</sup>	sC
Slope	47°-89°	0.3868	-0.0505	6.9791
	41°-47°	0.3641	-0.1099	9.7745
	36°-41°	0.3324	-0.1784	11.5885
	32°-36°	0.3064	-0.2598	13.0476
	28.5°-32°	0.2684	-0.3503	13.7068
	25°-28.5°	0.2068	-0.4170	12.7178
	21.5°-25°	0.1429	-0.4337	10.5914
	18°-21.5°	0.0758	-0.3708	7.1558
	13°-18°	0.0226	-0.2377	3.1994
Structure	Close to fault, thrust and lineament	0.5169	-0.6858	25.2137
Lithology	Marble	1.8394	-0.0405	18.2082
	Streaky banded and augen gneiss	0.9380	-0.9215	38.8269
Landuse	barren land (non-rocky)	1.2728	-0.6658	44.2759
	barren land (rocky)	0.5721	-0.0525	9.0118
	built-up area	0.1967	-0.0024	1.0450
	river sand	0.7478	-0.0113	5.0240
Soil depth	shallow	0.9930	-0.4508	33.2545
Aspect	southeast	0.8352	-0.2190	22.3148
	south	0.9127	-0.2087	23.1966
	southwest	0.2123	-0.0188	3.0571
Relative relief	0-130 m	0.1677	-0.0460	4.1723
	130 -202 m	0.0890	-0.0624	3.4611
	202 -288 m	0.0424	-0.0672	2.4466
	288 -408 m	0.0147	-0.0627	1.3851

The prediction rate curve was created using 713 testing landslide points (corresponding to landslide inventory for the period 2005 to 2009). The prediction rate curve shows a good match with the success rate curve, which indicates that the *wofe* model and the seven selected evidence layers are able to predict correctly the spatial occurrence of landslides (Figure 7.5).

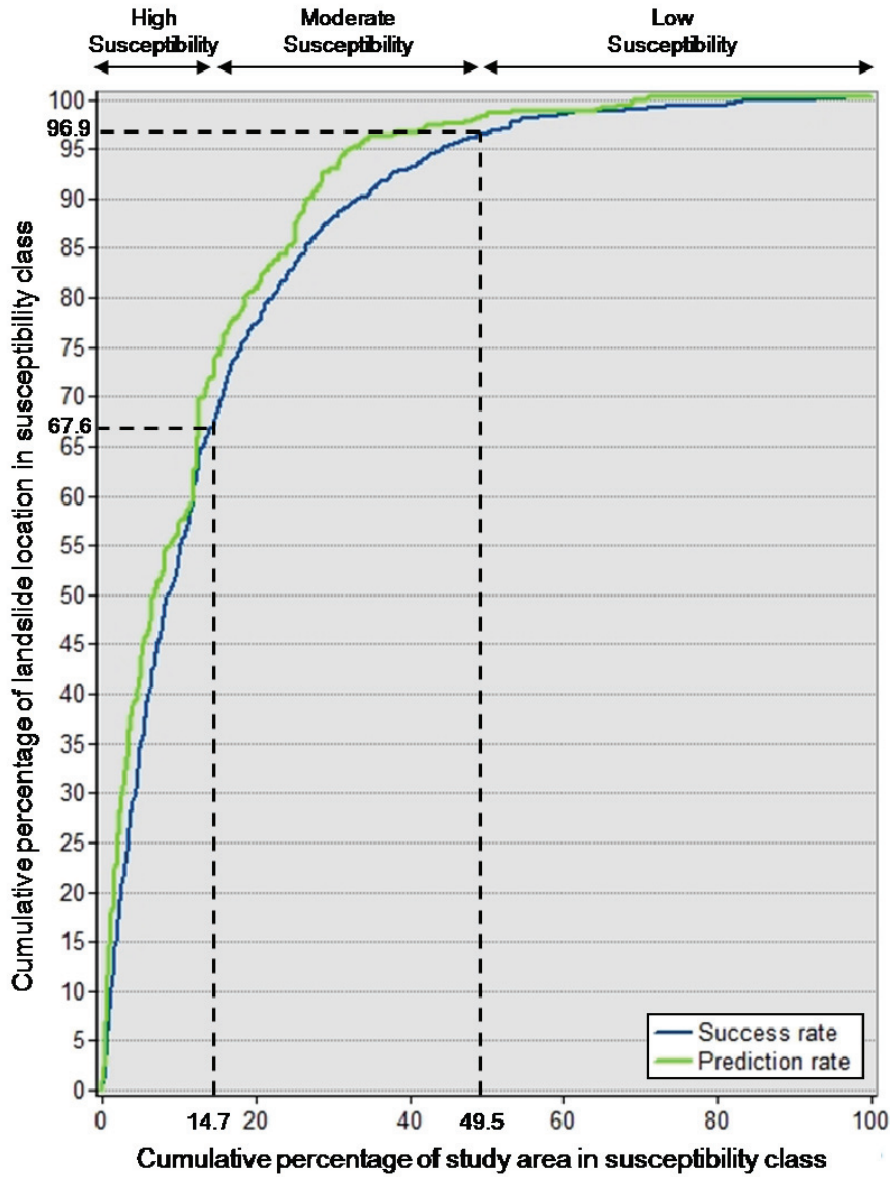


**Figure 7.5:** Analysis of wofe model for landslide susceptibility mapping showing the success and prediction rates.

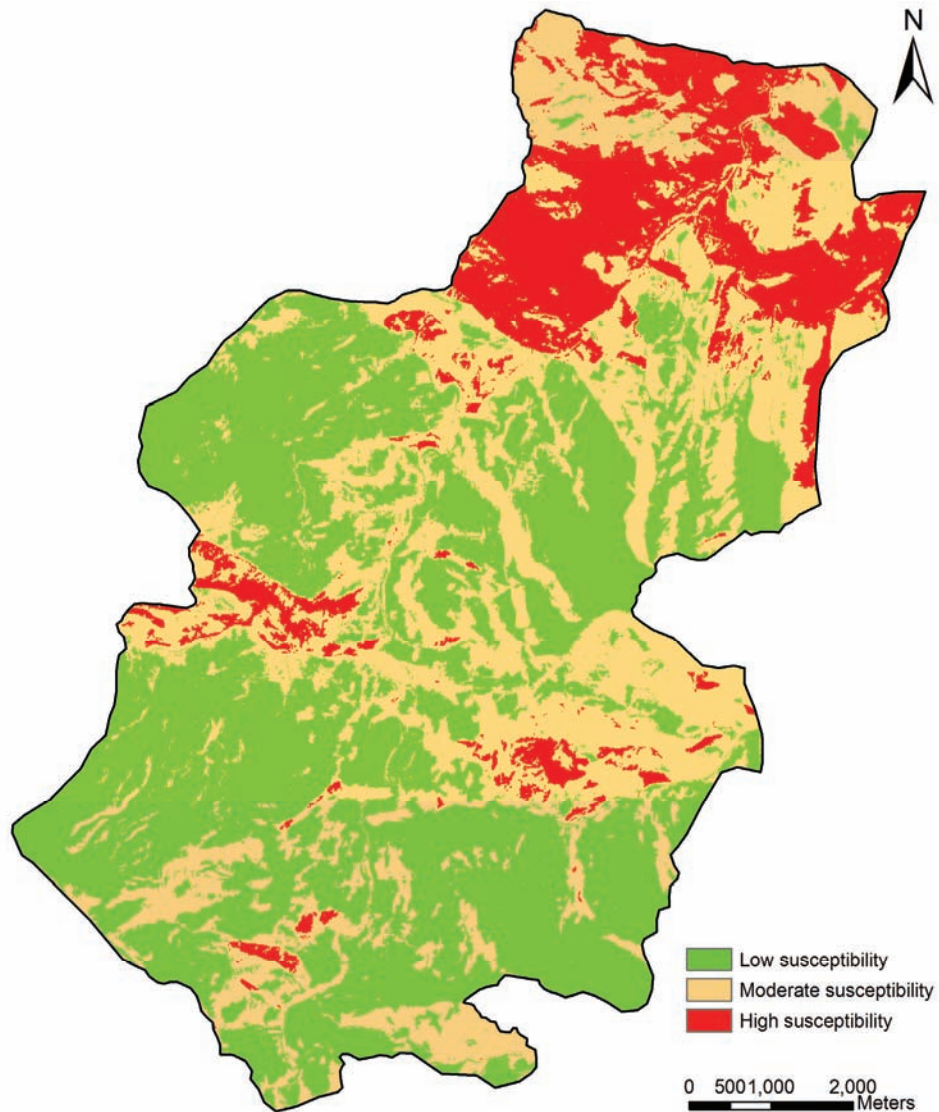


**Figure 7.6:** Landslide susceptibility map of the Okhimath area prepared by *wofe* model.

The receiver operating characteristic (ROC) curve provides a useful means to evaluate the performance of any classification scheme, and, therefore, was used to validate the *wofe* model. The ROC curve is the plot between the probability of true positive identified landslides versus that of false positive identified landslides, as the cut-off probability varies (Mathew et al., 2007). It is also a representation of the cut-off between sensitivity and specificity. The area under the ROC curve as shown in figure 7.7 is 0.651, which is relatively

high and shows the high accuracy of the *wofe* model for landslide susceptibility analysis.

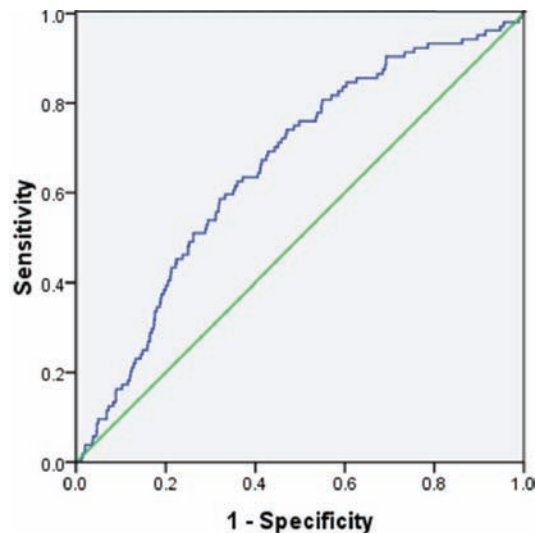


**Figure 7.7:** ROC curve of the *wofe* model developed for landslide susceptibility mapping. Green line is the reference line.

### 7.3.2 Landslide hazard assessment

The spatial probability of landslide occurrence for each observation year was estimated for the three susceptibility classes using equation 7.1. For estimating temporal probability, daily maximum rainfall for 34 years was analysed using Gumbel analysis. The result of the Gumbel plot is shown in figure 7.8. The trend line in this plot was used to estimate the temporal probability of the landslides for each observation year from 1997 to 2009.

### 7.3.3 Risk assessment

Risk assessment for buildings and roads was carried out separately and then both were added to estimate the total risk due to landslide in the Okhimath area. A total of 2211 building foot prints were mapped from the high resolution satellite data. The buildings were categorised during the field work into nine classes depending upon their utilisation. Further, each building category was classified into good, regular and bad class based on some representative building sample survey during the fieldwork. Table 7.3 lists all the category of buildings and their corresponding vulnerability values. The vulnerability values available in literature were assigned to each building category (Castellanos Abella, 2008). The average cost of the building in the hilly terrain available with border road organisation (BRO) was multiplied with

spatial probability and vulnerability for each observation year to estimate the total consequences due to the building.

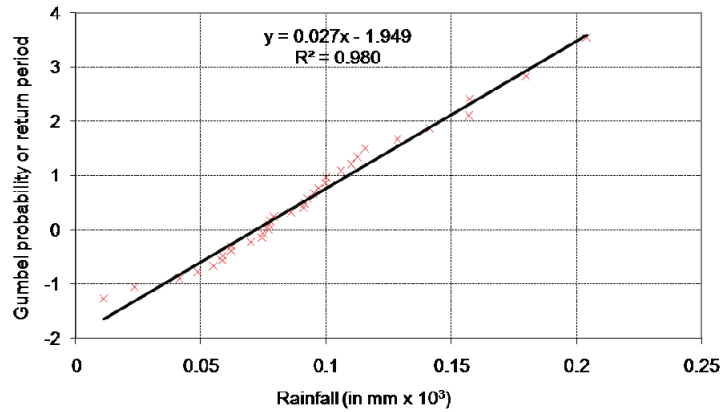


**Figure 7.8:** Gumbel plot for estimating the return period.

For the estimation of risk to the roads, interpretation of satellite data was performed, and a total road length of 105 km consisting of national highway and district road was prepared. The cost of maintenance for one km of damaged road available in the records of BRO is rupees 0.7 million Indian Rupees (Nayak, 2010). The vulnerability of each road type was multiplied on a cell by cell basis with spatial probability for the entire road length, the sum of which was subsequently multiplied with per km cost of the road, and the total risk due to landslides for each observation year from 1997 to 2009 was estimated.

**Table 7.3:** Building categories in the Okhimath area and their assigned vulnerability values.

Building category	Number	Good	Regular	Bad
Educational Institution	6	0.3	-	-
Guest House / Hotel	11	0.4	-	-
Hospital	2	0.4	-	-
Market Complex	50	0.4	0.6	0.8
Petrol filling station	1	0.3	-	-
Place of Worship	3	0.3	0.6	-
Police Station	1	0.3	-	-
Post Office	1	0.4	-	-
Residential	2135	0.5	0.8	1
Telephone Exchange	1	0.4	-	-

Finally, year-wise total loss due to landslides was calculated by summing up the building and road losses. This was then plotted against the temporal probability of occurrence of landslides, and a risk curve was prepared (Figure 7.9). The risk curve does not follow the ideal concave shape. This is due to the uncertainty in vulnerability quantification and non-consideration of all the elements at risk during the analysis. However, the graph will be useful to estimate landslide risk in the Okhimath area for any given return period.

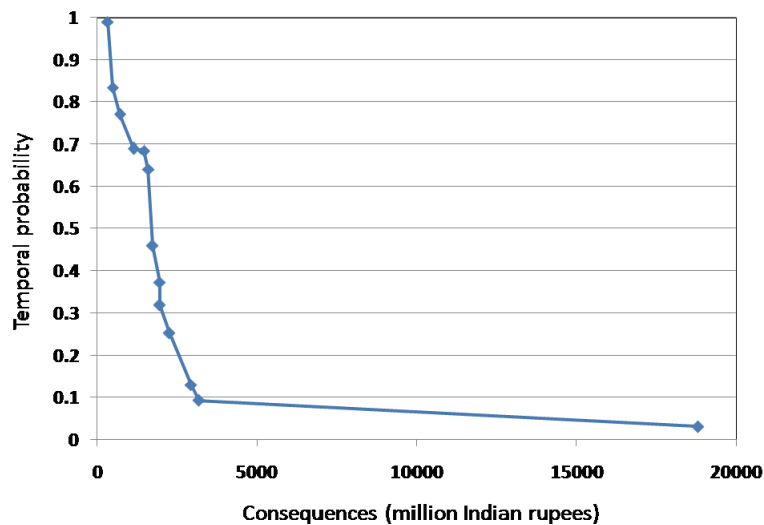


Figure 7.9: Total risk due to landslide in the Okhimath area.

## 7.4 Conclusion

In this chapter the use of a semi-automatically prepared landslide inventory from high resolution images in landslide hazard and risk assessment was demonstrated. The landslide susceptibility map was prepared using the established *wofe* model. The matching of prediction rate curve with the success rate curve, and the high value (0.651) of the area under ROC curve, indicates that semi-automatically prepared landslide inventory were successful in deriving weights for the evidence layers essential for preparing the landslide susceptibility map. This was mainly possible since the multi-temporal outputs from the semi-automatic methods were georeferenced to a common spatial framework and were available in a GIS ready format for further statistical analysis such as done by *wofe* model. The seven evidence layers for landslide susceptibility assessment used in this chapter were selected based on their high contribution to landsliding, which was also highlighted in previous studies. The present study validates the importance of these evidence layers for susceptibility assessment. Temporal probability was estimated by frequency analysis of historical rainfall data using Gumbel

distribution model. The landslide susceptibility map was transformed to a hazard map by integrating it with the spatial probability determined for each observation year using the annual landslide inventory. The risk curve, although, not perfectly concave, was able to depict the risk scenario in the Okhimath area. Although two elements at risk are considered in this study, the analysis allowed us to know the most landslide risk areas in Okhimath. The vulnerability values available in the literature were mainly used in risk assessment. This was done due to lack of damage assessment details. With a realistic assessment of vulnerability, the landslide risk curve for Okhimath area can be improved.

### ***Acknowledgements***

We thank Saibal Ghosh and Pankaj Jaiswal for very useful discussion.

## **Chapter 8: Synthesis**

This chapter provides a summary of the object-based methods developed in this research for semi-automatic detection of landslides, their advantages and limitations for a landslide rapid response system, accuracy of the generated landslide inventory maps, and how these maps are useful for landslide hazard and risk assessment. Finally, it gives an insight into a proposal towards landslide inventory mapping for hazard and risk assessment in India.

### **8.1 Introduction**

The availability of a new generation of high resolution satellite imagery offers a huge potential to develop rapid response systems for several types of natural disasters. Gradually disaster response and damage mapping have become increasingly dependent on space-based inputs (Arciniegas et al., 2007; Gamba et al., 2007; Joyce et al., 2009; Rau et al., 2007), as both the spatial and temporal resolution of available platforms have increased. Fast and robust products based on space-based inputs are being generated by many international agencies, including the International Charter "Space and Major Disasters". Recently, Voigt et al. (2007) showed how such support provided during disaster crisis management was useful for humanitarian causes. Given the requirement of a rapid response system, identification of the areas affected by natural disasters and the quantification of the damaging effects is of paramount importance for planning immediate relief operations. Landslides are one of principal natural disaster types that affect life and property in mountainous areas. Previously, identification of landslides was done either by visual image interpretation using post-landslide satellite images or in the field, which requires a considerable amount of time, especially if large areas have to be covered (Ray et al., 2009; Vinod Kumar et al., 2006; Wang et al., 2009). The main objective of this research was to develop an image analysis technique for the rapid detection of landslides in the aftermath of a triggering event (e.g. extreme rainfall or earthquake). The technique is not only intended to help post-disaster response but also capable of creating event-based landslide inventories, which are considered crucial for hazard and risk assessment. To achieve this, we used data from new generation sensors, the high spatial resolution stereoscopic Cartosat-1 (2.5 m) and Resourcesat-1 LISS-IV Mx (5.8 m), which were shown to have the potential to identify landslides with a minimum area of 774 m<sup>2</sup>. With the increase in spatial resolution of satellite data, the context becomes more important than the absolute DN values of the pixels for the accurate detection of any target feature. Therefore, a knowledge-based spectral-spatial-morphometric technique using object-based image analysis was

developed for the rapid detection of landslides. The method was modelled on the cognitive approach an expert uses during visual image interpretation for the identification of landslides. In the following sections, we discuss the main achievements and limitations of this research.

## **8.2 The role of DEM for detection of landslides**

Mass movements are geomorphic processes, and topographic information is extremely important for their identification. Morphometric parameters such as slope, flow direction, terrain curvature and relief derived from digital elevation model (DEM) contribute to the successful identification of landslides. High resolution DEMs were traditionally mainly generated from overlapping aerial photographs, but nowadays LiDAR is increasingly being considered as the best source for DEMs in landslide studies (Guzzetti et al., 1999; van Den Eeckhaut et al., 2007; van Westen et al., 2008). In the absence of these, new dedicated satellite missions, such as Cartosat-1 and ALOS-PRISM, have immense potential for fast and accurate generation of DSMs over large areas. While the term DEM was used for generic discussion in this research, digital surface model (DSM) refers to the elevation model extracted from satellite data by digital photogrammetric method and digital terrain model (DTM) refers to vegetation height corrected DSM.

In chapter 2, we presented the results on the extraction of a DSM from high resolution along-track stereoscopic data from Cartosat-1 and discussed the effects of sun elevation angle and valley orientation on the accuracy of DSMs. Along-track stereoscopy reduces the radiometric variation between the image pairs and helps in better extraction of a DEM than across-track stereoscopy. Using SAT-PP photogrammetric software and low (38°) and high (62°) sun elevation angle Cartosat-1 images, we generated a 10 m resolution DSM, which showed an absence of spikes and sinks that characterised the DSM generated using LPS software, due to its improved image matching technique. However, manual editing of the DSM was unavoidable, even though digital photogrammetry with computationally efficient software was attempted. This was mainly due to the steep slopes of the rugged Himalayan terrain that produce occlusion and shadow effects. Nevertheless, generation of a new DSM using post-landslide stereoscopic image is not a prerequisite for the detection of landslides by the method developed in this research, and high resolution DEMs prepared beforehand for steep and rugged mountainous areas can be used. Therefore, in order to be able to carry out rapid mapping of landslides in any susceptible areas, generation of accurate DEMs is essential.

Vertical RMSEs of high and low sun elevation angle DSMs calculated by comparing with check points obtained from a DGPS survey, were 2.31 and 2.51 m, respectively, which is considered the optimal given the spatial resolution (2.5 m) of the Cartosat-1 data. Spatial accuracy, which has a significant influence on the DEM derivatives, was measured by comparing the location of drainage lines. It was found that valleys oriented in the N-S direction offered less problems for image matching resulting in a better spatial accuracy, in comparison to E-W oriented valleys. Therefore, less effort in manual editing was required for such areas. For valleys perpendicular to the satellite track, the DSM extracted from a low sun elevation angle data showed a 45% higher spatial accuracy than the DSM extracted from high sun elevation angle data. The results indicate that the sun elevation angle and valley orientation affect the spatial accuracy of the DSM, though metric accuracy remains comparable.

The measurement of landslide volume was addressed in chapter 3. DSMs derived from Cartosat-1 data were converted to DTMs by applying vegetation height correction. The landslide volume was estimated by elevation change analysis using pre- and post-landslide DTMs. For the example used, the loss ( $0.55 \times 10^6 \text{ m}^3$ ) and gain volumes ( $1.43 \times 10^6 \text{ m}^3$ ) calculated with ground control points are comparable with the loss ( $0.54 \times 10^6 \text{ m}^3$ ) and gain volumes ( $1.41 \times 10^6 \text{ m}^3$ ) volume without ground control points, indicating that RPCs alone were sufficient for estimation of volume, thus freeing rapid volume assessment entirely from field data requirement. However, the volume values calculated showed deviations of about +18% and -12% for the volume loss and gain areas, respectively, when compared with the corresponding reference volumes. Although estimation of volume from Cartosat-1 data for large landslides was shown in chapter 3 to be effective, calculation of landslide volume for small landslides from Cartosat-1 data, ideal for a DEM of 10 m grid size, needs to be examined.

### **8.3 Knowledge-based object-oriented method**

In addition to the DN values used in pixel-based image analysis methods, objects (which are groups of homogeneous pixels) allow the incorporation of shape, size and context into the image analysis. This helped in the application of landslide process knowledge to image analysis using satellite images and satellite derived DEMs. The results of the object-oriented image analysis are verifiable on the ground and ready for further GIS analysis.

#### **8.3.1 Detection of landslides using multispectral images**

The characterisation of landslides, which forms the first step towards the detection of landslides, was addressed in chapter 4. Objects were derived by

multi-resolution segmentation of LISS-IV (5.8 m) multispectral image. Landslide candidate objects were identified using a NDVI threshold. Features, such as river sands, built-up areas, shadows, rivers, barren rocky and agricultural lands and roads having similar or lower NDVI values than the threshold, were subsequently identified and removed. Once all these false positives were removed, the remaining objects represented mostly landslides. They were further classified based on material type and failure mechanism using the criteria defined by Varnes (1984) and Working Party on the World Landslide Inventory (UNESCO-WP/WLI, 1993b). While some previous researchers (e.g. Barlow et al., 2006) used a nearest neighbourhood classification in object-based environment to detect landslides, others (e.g. Moine et al., 2009) partly characterised landslides for their detection using object-oriented analysis (OOA). However, we, for the first time, comprehensively characterised five different types of landslides using the visual image interpretation keys. Segmentation using a terrain curvature layer helped to classify the landslide failure mechanism. Classification based on material type was achieved using adjacency conditions to the land cover units. A generic procedure was developed using eCognition software for the identification and classification of landslides. The method was able to detect five types of landslides: shallow translational rock slides, rotational rock slides, translational rock slides, debris slides and debris flows, with their extent ( $m^2$ ) showing 69.9 and 69.5% recognition and classification accuracies, respectively, and a 9.2% error of commission. Detection of landslides in a terrain having several identical features was another major achievement of this research. However, the procedure of hard coding in many stages and selection of scale factors for deriving objects requires a substantial user interaction and is not directly applicable in other areas.

In chapter 5, we focused on further generalisation of the automatic landslide detection procedure. We developed a new plateau objective function (POF) by combining spatial autocorrelation and intra-segment variance of objects, which eliminated a large part of the subjectivity in the selection of scale factors during the multiresolution segmentation for the derivation of objects that were used for identification and classification of landslides. False positives were identified at multiple levels using multiple optimum scale factors determined by the POF, unlike a single factor as used in chapter 4. This led to a better accuracy of the extent of landslides (76.9 and 74.4 %, recognition and classification accuracies, respectively) and a low error of commission (4.3%). The assignment of the scale factor to a false positive identification was done interactively, which remained a limitation of the study. However, knowledge of existing false positive classes in an area, and their spectral and spatial relationship vis-a-vis scale factor for a sample area

of the image may help in linking the optimal scales to false positives. Nevertheless, the user-driven thresholds applied at various stages of the routine developed in chapter 4 were avoided by the use of data-driven thresholds determined by a K-means clustering algorithm. Finally, when the routine developed in the western Himalayas was tested in another area in the eastern Himalayas without any change to its structure, it produced results having similar accuracy (77.7%) for the extent of landslides. This indicates that the procedure developed in chapter 5 is generic and transferable. However, the reference landslide inventory of the eastern Himalayas was prepared with extensive field work and contains additional landslides found in the image shadow areas. Those landslides could not be detected by OOA. Unsupervised selection of optimal scales and threshold values for detection of landslides are significant achievements of this chapter.

### **8.3.2 Detection of landslides using panchromatic images**

In many areas around the world, systematic landslide inventory data are not available. Satellite images are available for several parts of the world in the archives of many data providers, although those high resolution images are mostly panchromatic in nature, which poses a challenge, particularly due to the limitation that NDVI as used in chapters 4 and 5 cannot be generated from those images.

In chapter 6, we presented a method for generating historical landslide inventories for a period of 9 years from 1997 to 2006 except 2004, using a time-series of IRS-1D panchromatic images (5.8 m). The methodology developed in chapters 4 and 5 was slightly modified to address some of the specific issues related to panchromatic images. Object-based change detection using multi-temporal images was attempted for the first time in this chapter. While panchromatic images were used to derive objects through multiresolution segmentation, brightness was used as a NDVI replacement for the extraction of landslide candidates. However, instead of using global threshold values for brightness, we used an adaptive local brightness threshold for the extraction of landslide candidates. DN values from pre- and post-landslide images were converted to top of the atmosphere (TOA) reflectance values to compensate for seasonal setting in data acquisition and illumination effects. Subsequently, a change detection procedure with normalised TOA reflectance images was used to identify some landslide candidates that could not be detected by the local thresholding procedure. Use of brightness threshold had a positive effect in terms of the number of false positives to be eliminated, since rivers and shadow areas were excluded from the false positives. Grey level co-occurrence matrix (GLCM) texture measures were used extensively for the identification of false positives.

Finally, landslides were classified based on material type and failure mechanism, using the same knowledge-based method as discussed in chapter 4. Year-wise accuracy assessment of each landslide type was carried out separately. 95.7% recognition accuracy for the extent of shallow translational landslide, the dominant landslide types, after the August 1998 super event could be achieved in this study, with an 10.4% error of commission. Debris slides, although a minor proportion of all landslides, showed a recognition accuracy of the landslide extent in the range of 55.7 to 98.5%. However, parts of the channel deposits were incorrectly classified as debris slides leading to a high error of commission is high, which indicates that without spectral information, creation of a multi-temporal inventory is quite challenging.

## **8.4 Use of the semi-automated landslide detection technique**

### **8.4.1 Rapid event-based mapping**

In this research we developed a set of generic procedures for the semi-automatic detection of landslides. Although the methodology was developed using satellite data in parts of the Indian Himalayas, no field data specific to this area were used in the procedure, and therefore it has the potential to be applied in any other landslide prone area of the world for landslide detection. The model is also less data demanding, since it uses only high resolution post-landslide satellite image and a DTM (existing or new). Although a post-landslide DEM is not mandatory, we suggest using it if available, particularly for the identification of large landslides as the morphology has likely changed due to landsliding. Similarly, pre-landslide high resolution satellite image, if available, would also improve the accuracy of landslide detection. The type of satellite data (i.e. spectral channels and spatial resolution) used in this model are commonly available and the number of satellites providing such data is growing every year (van Westen et al., 2008). Therefore, the developed method has immense potential to be used in supporting crisis management by providing specific information about landslide occurrences.

One disadvantage of the procedure is that the segment optimisation procedure discussed in chapter 5 requires knowledge of broad land cover types of the local area, so that the false positives can be assigned to a corresponding scale factor. Although it is not difficult, particularly through a rapid reconnaissance of high resolution images, to overcome this it is suggested to divide the area (if it is large) into tiles and optimise the rule set tile-wise by understanding the scale dependency of land cover units. Once

the optimisation is done it can be used to routinely identify landslides. This will be very effective in areas where the recurrence of landslides is frequent.

### **8.4.2 Hazard and risk assessment**

A landslide inventory containing landslide events over a substantial period of time is a fundamental requirement for hazard and risk assessment. Using the methodology explained in chapters 4 to 6, landslide inventories for a 13 year period (1997-2009) were prepared.

In chapter 7, we have shown the use of landslide inventories prepared by the semi-automatic method for landslide hazard and risk assessment. A susceptibility map was made using the Weights-of-Evidence method, which is a data-driven bivariate method, wherein weights were derived using the semi-automatically prepared historical landslide inventories combined with a series of pre-disposing factor maps. Seven evidence layers were used for the calculation of weights, selected in such a way that the majority could be derived from satellite data. Validation done using the test data created through a temporal subsetting of the inventories showed a good prediction result that is evident from the high value (0.651) of area under the ROC curve. This was mainly possible since the historical inventories prepared by the semi-automatic method were georeferenced to a common spatial framework and were available in a GIS ready format for further statistical analysis. While temporal probability was calculated using rainfall data of previous 34 years (1978-2009) through Gumbel frequency distribution analysis, spatial probability was determined by calculating landslide density for the inventories per susceptibility class that represent a given return period. Elements at risk, such as building footprints and roads, were interpreted from high resolution satellite image. Due to the lack of landslide damage details of the study area, vulnerability values (0.3 to 1) for buildings and roads, available in the literature, were used in the risk assessment. Finally, the costs of the buildings and roads were multiplied with their respective vulnerabilities and landslide spatial probability to derive the total loss for different return period scenarios corresponding to the landslide inventory period. Subsequently, a risk curve between the loss and temporal probability was created. The risk curve, although without an ideal concave shape due to uncertainty involved in vulnerability assumptions, can be used to estimate loss due to any future rainfall event in the Okhimath area. This study showed that the inventory prepared by OOA is not only useful for a landslide rapid response system, but also can be used for landslide hazard and risk assessment.

## **8.5 Future work**

Several new methods were applied to high resolution satellite images and DEMs for the detection of landslides and the creation of historical landslide inventories. The methodology uses a knowledge-based procedure through cognitive reasoning and was tested in two geomorphologically distinct areas in the Himalayas in India. Recently, Tumuhairwe (2011) has evaluated the transferability of this methodology to detect landslides triggered due to the 2010 Haiti earthquake, and obtained reasonably good results. However, it will be interesting to further test it in additional areas, particularly in a post-disaster scenario, to verify the flexibility, transferability and robustness of the landslide detection procedure. The methodology identified five types of commonly occurring landslides. Identification of other landslide types, such as rock falls or topples, still need to be tested. The method can only identify landslides that disrupt the vegetation (low NDVI) or create objects that are identifiable by their high reflectance. Identification of landslides that retain (part of) the land cover is difficult using the developed method.

Identification of some of the land cover units, such as agricultural areas or barren land, as landslide false positives was done in a crisp manner, although they are sometimes fuzzy in nature. Since the methodology uses adjacency conditions to land use/land cover units for the classification of landslides based on material type, it is worth to address landslide classification with a fuzzy concept and test the outcome of the semi-automatic procedure. Erroneous identification of those land cover units will also classify the landslides wrongly. Therefore, evaluation of uncertainty and error propagation of landslide classification might be useful.

Finally, the methodology presented in the dissertation uses satellite data in the visible region of the electromagnetic spectrum (EMR). In tropical regions, where landslides are triggered by rainfall, such post-landslide satellite data are often cloudy. Therefore, data providers have to wait until the conditions become cloud free, an unavoidable yet unfortunate scenario during the critical post-disaster period. Satellites operating in the microwave region can provide data in such conditions since radar signal can penetrate through clouds. Nevertheless, microwave satellite data have some other inherent problems, such as topographic distortions through foreshortening and layover effects. Removal of these effects and characterisation of microwave data for landslide detection is quite challenging, but can greatly benefit any rapid response system by providing landslide specific information, particularly in cloudy conditions. However, using the Permanent Scatterer (PS) method this can be overcome also rather easily. But then there are other problems, as

these methods are best for slow moving landslides and are not very applicable in vegetated area, as well as areas with limited corner reflectors.

### **8.5.1 Towards an operational method in India**

The results presented in this research are the outcome of the GSI-NRSC-ITC joint collaboration on landslide studies. While scientific innovation through this research is critical, it is implicit that the new methodology should also contribute towards the operational requirement of landslide hazard and risk mapping of India, where 15 % of the geographical area is prone to landslides. However, the landslide inventory available is spatially discontinuous and temporally sporadic. The National Remote Sensing Centre (NRSC), a unit of Indian Space Research Organisation (ISRO), is the satellite data provider for the country and has a vast amount of data available in the archives collected from ISRO's own satellites and also from foreign satellites. Baseline satellite imagery and DEM data pertaining to landslide prone areas of India need to be created that can be handled in tiles. For each tile the semi-automatic landslide detection procedure has to be optimised that can subsequently be used to identify landslides in prospective and retrospective manner. This effort will lead to an operational method towards the creation of a centralised systematic landslide inventory database for India.

The Geological Survey of India (GSI), which is a partner in this collaboration, has a vast amount of geological data and field observations. These data form an input for the landslide hazard assessment. Also under this collaborative programme, new innovative methods were developed for landslide susceptibility, hazard and risk assessment using field data and a landslide inventory made through visual interpretation of satellite data. However, now with the availability of a semi-automatic detection method, historical landslide inventory in a GIS database can be prepared faster, which will aid effective and faster landslide hazard and risk mapping for the vast mountainous areas of India. Altogether, although it sounds very optimistic now, an operational method for medium scale landslide hazard and risk mapping using the findings of these studies is quite achievable.

More importantly, the outcome of this study will give an impetus to the landslide research and unfold the potential of object-based research for future disaster support and management activities not only in India but also elsewhere.



## Bibliography

- Aguilar, F.J., Aguera, F., Aguilar, M.A. and Carvajal, F., 2005. Effects of terrain morphology, sampling density, and interpolation methods on grid DEM accuracy. *Photogrammetric Engineering and Remote Sensing*, 71(7): 805-816.
- Ahmed, N. et al., 2007. Extraction and validation of Cartosat-1 DEM. *Journal of the Indian Society of Remote Sensing*, 35(2): 121-127.
- Akcay, H.G. and Aksoy, S., 2008. Automatic detection of geospatial objects using multiple hierarchical segmentations. *IEEE Transactions on Geoscience and Remote Sensing*, 46(7): 2097-2111.
- Anbalagan, R., 1992. Landslide hazard evaluation and zonation mapping in mountainous terrain. *Engineering Geology*, 32(4): 269-277.
- Arciniegas, G.A., Bijker, W., Kerle, N. and Tolpekin, V.A., 2007. Coherence- and Amplitude-Based Analysis of Seismogenic Damage in Bam, Iran, Using ENVISAT ASAR Data. *IEEE Transactions on Geoscience and Remote Sensing*, 45(6): 1571-1581.
- Baatz, M. and Schäpe, A., 2000. Multiresolution Segmentation: an optimization approach for high quality multi-scale image segmentation, In: Strobl, L.J., Blaschke T. and Griesebener T. (Eds.), *Angewandte geographische informationsverarbeitung XII, Beiträge zum AGIT Symposium Salzburg 2000*. Herbert Wichmann Verlag, Heidelberg, pp. 12-23.
- Bahuguna, I.M., Kulkarni, A.V. and Nayak, S., 2004. DEM from IRS-1C PAN stereo coverages over Himalayan glaciated region—accuracy and its utility. *International Journal of Remote Sensing*, 25(19): 4029-4041.
- Bahuguna, I.M., Kulkarni, A.V. and Nayak, S., 2008. Impact of slope on DEM extracted from IRS 1C PAN stereo images covering Himalayan glaciated region: A few case studies. *International Journal of Geoinformatics*, 4(2): 21-28.
- Baltsavias, E., Kocaman, S., Akca, D. and Wolff, K., 2007. Geometric and radiometric investigations of Cartosat-1 data, ISPRS Workshop, "High Resolution Earth Imaging for Geospatial Information", Hannover, Germany, pp. (Proceedings on CDROM).
- Baltsavias, E., Kocaman, S. and Wolff, K., 2008. Analysis of Cartosat-1 images regarding image quality, 3D point measurement and DSM generation. *The Photogrammetric Record*, 23(123): 305-322.
- Barlow, J., Franklin, S. and Martin, Y., 2006. High spatial resolution satellite imagery, DEM derivatives, and image segmentation for the detection of mass wasting processes. *Photogrammetric Engineering and Remote Sensing*, 72(6): 687-692.
- Barlow, J., Martin, Y. and Franklin, S.E., 2003. Detecting translational landslide scars using segmentation of Landsat ETM+ and DEM data in the northern Cascade Mountains, British Columbia. *Canadian Journal of Remote Sensing*, 29(4): 510-517.
- Barnard, P.L., Owen, L.A., Sharma, M.C. and Finkel, R.C., 2001. Natural and human-induced landsliding in the Garhwal Himalaya of northern India. *Geomorphology*, 40(1-2): 21-35.
- Bell, R. and Glade, T., 2004. Quantitative risk analysis for landslides – Examples from Bildudalur, NW-Iceland. *Natural Hazards and Earth System Sciences*, 4: 117-131.

## *Bibliography*

---

- Benz, U.C., Hofmann, P., Willhauck, G., Lingenfelder, I. and Heynen, M., 2004. Multi-resolution, object-oriented fuzzy analysis of remote sensing data for GIS-ready information. *ISPRS Journal of Photogrammetry and Remote Sensing*, 58(3/4): 239-258.
- Berthier, E. and Toutin, T., 2008. SPOT5-HRS digital elevation models and the monitoring of glacier elevation changes in North-West Canada and South-East Alaska. *Remote Sensing of Environment*, 112(5): 2443-2454.
- Blaschke, T., 2010. Object based image analysis for remote sensing. *ISPRS Journal of Photogrammetry and Remote Sensing*, 65(1): 2-16.
- Blaschke, T., Burnett, C. and Pekkarinen, A., 2006. Image segmentation methods for object-based analysis and classification. In: S.M. de Jong and F.D. van der Meer (Editors), *Remote sensing image analysis: including the spatial domain*. Springer, Dordrecht, The Netherlands, pp. 211-236.
- Blaschke, T. and Strobl, T., 2001. What's wrong with pixels? Some recent developments interfacing remote sensing and GIS, *GeoBIT/GIS*, pp. 12-17.
- Bolstad, P.V. and Stowe, T., 1994. An Evaluation of DEM accuracy: Elevation, Slope and Aspect. *Photogrammetric Engineering and Remote Sensing*, 60(11): 1327-1332.
- Bonham-Carter, G.F., Agterberg, F.P. and Wright, D.F., 1989. Weights of evidence modelling: a new approach to mapping mineral potential. *Statistical application in Earth Sciences*, 89(9): 171-183.
- Borghuis, A.M., Chang, K. and Lee, H.Y., 2007. Comparison between automated and manual mapping of typhoon-triggered landslides from SPOT-5 imagery. *International Journal of Remote Sensing*, 28(7-8): 1843-1856.
- Brardinoni, F., Slaymaker, O. and Hassan, M.A., 2003. Landslide inventory in a rugged forested watershed: a comparison between air-photo and field survey data. *Geomorphology*, 54(3-4): 179-196.
- Carranza, E.J.M. and Hale, M., 2003. Evidential belief functions for data-driven geologically constrained mapping of gold potential, Baguio district, Philippines. *Ore Geology Reviews*, 22(1-2): 117-132.
- Carrara, A., Cardinali, M. and Guzzetti, F., 1992. Uncertainty in assessing landslide hazard and risk. *ITC Journal 2*: 172-183.
- Carrara, A. and Merenda, L., 1976. Landslide inventory in northern Calabria, southern Italy. *Geological Society of America Bulletin*, 87: 1153-1162.
- Casson, B., Delacourt, C., Baratoux, D. and Allemand, P., 2003. Seventeen years of the "La Clapiere" landslide evolution analysed from orthorectified aerial photographs. *Engineering Geology*, 68(1-2): 123-139.
- Castellanos Abella, E.A., 2008. Multi-scale landslide risk assessment in Cuba. ITC dissertation 154 Thesis, Utrecht University, Utrecht, 273 pp.
- Chandler, J., 1999. Effective application of automated digital photogrammetry for geomorphological research. *Earth Surface Processes and Landforms*, 24: 51-63.
- Chang, Y.-L. et al., 2007. Multisource data fusion for landslide classification using generalized positive boolean functions. *IEEE Transactions on Geoscience and Remote Sensing*, 45(6): 1697-1708.
- Chaplot, V. et al., 2006. Accuracy of interpolation techniques for the derivation of digital elevation models in relation to landform types and data density. *Geomorphology*, 77(1-2): 126-141.

- Chen, K.S., Crawford, M.M., Gamba, P. and Smith, J.S., 2007. Introduction for the special issue on remote sensing for major disaster prevention, monitoring, and assessment. *IEEE Transactions on Geoscience and Remote Sensing*, 45(6): 1515-1518.
- Chen, R.-F. et al., 2005. Large earthquake-triggered landslides and mountain belt erosion: The Tsaoiling case, Taiwan. *Comptes Rendus Geosciences*, 337(13): 1164-1172.
- Cheng, K.S., Wei, C. and Chang, S.C., 2004. Locating landslides using multi-temporal satellite images. *Advances in Space Research*, 33(3): 296-301.
- Chow, V.T., Maidment D.R. and Mays, L.R., 1988. *Applied Hydrology*. McGraw-Hill, New York, USA.
- Cruden, D. and Varnes, D.J., 1996. Landslide types and processes. In: A.K. Turner and R.L. Schuster (Editors), *Landslides Investigation and Mitigation. Special Report 247*. Transportation Research Board, National Academy of Sciences, Washington D.C., pp. 36-75.
- Dai, F.C. and Lee, C.F., 2001. Frequency-volume relation and prediction of rainfall-induced landslides. *Engineering Geology*, 59(3-4): 253-266.
- Daniels, A.E., 2006. Incorporating domain knowledge and spatial relationships into land cover classifications: a rule-based approach. *International Journal of Remote Sensing*, 24(14): 2949-2975.
- Definiens, 2007. *Developer 7: Userguide*. Definiens Imaging GmbH.
- Devoli, G., Morales, A. and Hoeg, K., 2007. Historical landslides in Nicaragua—collection and analysis of data. *Landslides*, 4(1): 5-18.
- Dewitte, O. and Demoulin, A., 2005. Morphometry and kinematics of landslides inferred from precise DTMs in West Belgium. *Natural Hazards and Earth System Sciences*, 5(2): 259-265.
- Dissanska, M., Bernier, M. and Payette, S., 2009. Object-based classification of very high resolution panchromatic images for evaluating recent change in the structure of patterned peatlands. *Canadian Journal of Remote Sensing*, 35(2): 189-215.
- Dragut, L. and Blaschke, T., 2006. Automated classification of landform elements using object-based image analysis. *Geomorphology*, 81(3/4): 330-344.
- Dragut, L., Tiede, D. and Levick, S.R., 2010. ESP: a tool to estimate scale parameter for multiresolution image segmentation of remotely sensed data. *International Journal of Geographical Information Science*, 24(6): 859-871.
- Dubuisson-Jolly, M.P. and Gupta, A., 2000. Colour and texture fusion: application to aerial image segmentation and GIS updating. *Image and Vision Computing*, 18(10): 823-832.
- Dunning, S.A., Mitchell, W.A., Rosser, N.J. and Petley, D.N., 2007. The Hattian Bala rock avalanche and associated landslides triggered by the Kashmir Earthquake of 8 October 2005. *Engineering Geology*, 93(3-4): 130-144.
- Eckert, S., Kellenberger, T. and Itten, K., 2005. Accuracy assessment of automatically derived digital elevation models from aster data in mountainous terrain. *International Journal of Remote Sensing*, 26(9): 1943-1957.
- eCognition, 2009. *eCognition Developer 8, Reference Book*. Definiens AG, Munich, Germany.

## *Bibliography*

---

- Ehsani, A.H. and Quiel, F., 2008. Application of Self Organizing Map and SRTM data to characterize yardangs in the Lut desert, Iran. *Remote Sensing of Environment*, 112(7): 3284-3294.
- Elmqvist, B., Ardö, J. and Olsson, L., 2008. Land use studies in drylands: an evaluation of object-oriented classification of very high resolution panchromatic imagery. *International Journal of Remote Sensing*, 29(24): 7129 - 7140.
- Endreny, T.A., Wood, E.F. and Lettenmaier, D.P., 2000. Satellite-derived digital elevation model accuracy: hydrogeomorphological analysis requirements. *Hydrological Processes*, 14(1): 1-20.
- Espindola, G.M., Camara, G., Reis, I.A., Bins, L.S. and Monteiro, A.M., 2006. Parameter selection for region-growing image segmentation algorithms using spatial autocorrelation. *International Journal of Remote Sensing*, 27(14): 3035-3040.
- FGDC, 1998. Geospatial Positioning Accuracy Standards, Part 3: National Standard for Spatial Data Accuracy, U.S. Federal Geographic Data Committee. URL: <http://www.fgdc.gov/standards/projects/FGDC-standards-projects/accuracy/part3/index.html> (last date accessed: 20 March 2009).
- Florinsky, I.V., 1998. Combined analysis of digital terrain models and remote sensing data in landscape investigations. *Progress in Physical Geography*, 22(1): 33-60.
- Galli, M., Ardizzone, F., Cardinali, M., Guzzetti, F. and Reichenbach, P., 2008. Comparing landslide inventory maps. *Geomorphology*, 94(3-4): 268-289.
- Gamba, P., Dell'Acqua, F. and Trianni, G., 2007. Rapid Damage Detection in the Bam Area Using Multitemporal SAR and Exploiting Ancillary Data. *IEEE Transactions on Geoscience and Remote Sensing*, 45(6): 1582-1589.
- Gao, Y., Mas, J.F., Kerle, N. and Navarrete, A., In Press. Optimal region growing segmentation and its effect on classification accuracy. *International Journal of Remote Sensing*.
- Ghosh, S., Gunther, A., Carranza, E.J.M., van Westen, C.J. and Jetten, V.G., 2010. Rock slope instability assessment using spatially distributed structural orientation data in Darjeeling Himalaya (India). *Earth Surf. Process. Landforms*, 35(15): 1773-1792.
- Ghosh, S. et al., 2009. A quantitative approach for improving the BIS (Indian) method of medium-scale landslide susceptibility. *Journal of the Geological Society of India*, 74(5): 625-638.
- Glade, T., 2003. Vulnerability assessment in landslide risk analysis. *Beitrag zur erdsystemforschung*, 134(2): 123-146.
- Gong, J., Li, Z., Zhu, Q., Sui, H. and Zhou, Y., 2000. Effects of Various Factors on the Accuracy of DEMs: An Intensive Experimental Investigation. *Photogrammetric Engineering and Remote Sensing*, 66(9): 1113-1117.
- Gooch, M.J., Chandler, J.H. and Stojic, M., 1999. Accuracy assessment of digital elevation models generated using the Erdas Imagine OrthoMAX digital photogrammetric system. *The Photogrammetric Record*, 16(93): 519-531.
- Gorokhovich, Y. and Voustianiouk, A., 2006. Accuracy assessment of the processed SRTM-based elevation data by CGIAR using field data from

- USA and Thailand and its relation to the terrain characteristics. *Remote Sensing of Environment*, 104(4): 409-415.
- Gorum, T. et al., 2010. Distribution Pattern of Earthquake-induced Landslides Triggered by the 12 May 2008 Wenchuan Earthquake. *Geomorphology*, In press.
- Gruen, A., Kocaman, S. and Wolff, K., 2007. High Accuracy 3D Processing of Stereo Satellite Images in Mountainous Areas, Dreilaendertagung 2007, Muttenz-Basel, Switzerland.
- Gumbel, E.J., 1958. *Statistics of extremes*. Columbia University Press, New York, USA, 375 pp.
- Guzzetti, F., Cardinali, M., Reichenbach, P. and Carrara, A., 2000. Comparing landslide maps: A case study in the upper Tiber River Basin, central Italy. *Environmental Management*, 25(3): 247-263.
- Guzzetti, F. et al., 2004. Landslides triggered by the 23 November 2000 rainfall event in the Imperia Province, Western Liguria, Italy. *Engineering Geology*, 73(3-4): 229-245.
- Guzzetti, F., Carrara, A., Cardinali, M. and Reichenbach, P., 1999. Landslide hazard evaluation: a review of current techniques and their application in a multi-scale study, Central Italy. *Geomorphology*, 31(1-4): 181-216.
- Guzzetti, F., Reichenbach, P., Cardinali, M., Galli, M. and Ardizzone, F., 2005. Probabilistic landslide hazard assessment at the basin scale. *Geomorphology*, 72(1-4): 272-299.
- Haralick, R.M., Shanmugam, K. and Dinstein, I., 1973. Textural features for image classification *IEEE Transactions on Systems, Man, and Cybernetics*, 6: 610-621.
- Haralick, R.M. and Shapiro, L.G., 1985. Survey: Image segmentation techniques. *Computer Vision, Graphics, and Image Processing*, 29(1): 100-132.
- Hirano, A., Welch, R. and Lang, H., 2003. Mapping from ASTER stereo image data: DEM validation and accuracy assessment. *ISPRS Journal of Photogrammetry and Remote Sensing*, 57(5-6): 356-370.
- Hofmann, T., Puzicha, J. and Buhmann, J., 1998. Unsupervised texture segmentation in a deterministic annealing framework. *IEEE Transactions on Pattern Analysis and Machine Intelligence*, 20(8): 803-818.
- Höhle, J. and Potuckova, M., 2006. The EuroSDR Test "Checking and Improving of Digital Terrain Models" (Official publication no. 51). URL: <http://bono.hostireland.com/~eurocdr/publications/51.pdf> (last date accessed: 20 March 2009).
- Holmes, K.W., Chadwick, O.A. and Kyriakidis, P.C., 2000. Error in a USGS 30-meter digital elevation model and its impact on terrain modeling. *Journal of Hydrology*, 233(1-4): 154-173.
- Holt, A.C., Seto, E.Y.W., Rivard, T. and Gong, P., 2009. Object-based detection and classification of vehicles from high-resolution aerial photography. *Photogrammetric Engineering and Remote Sensing*, 75(7): 871-880.
- Hu, Y. and Tao, C.V., 2002. Updating Solutions of the Rational Function Model Using Additional Control Information. *Photogrammetric Engineering and Remote Sensing*, 68(7): 715-723.
- Iwahashi, J. and Pike, R.J., 2007. Automated classifications of topography from DEMs by an unsupervised nested-means algorithm and a three-part geometric signature. *Geomorphology*, 86(3-4): 409-440.

## *Bibliography*

---

- Jaiswal, P. and van Westen, C.J., 2009. Estimating temporal probability for landslide initiation along transportation routes based on rainfall thresholds. *Geomorphology*, 112(1-2): 96-105.
- Jaiswal, P., van Westen, C.J. and Jetten, V., 2011. Quantitative assessment of landslide hazard along transportation lines using historical records. *Landslides*, In Press.
- Joyce, K.E., Belliss, S.E., Samsonov, S.V., McNeill, S.J. and Glassey, P.J., 2009. A review of the status of satellite remote sensing and image processing techniques for mapping natural hazards and disasters. *Progress in Physical Geography*, 33(2): 183-207.
- Kääb, A., 2002. Monitoring high-mountain terrain deformation from repeated air- and spaceborne optical data: examples using digital aerial imagery and ASTER data. *ISPRS Journal of Photogrammetry and Remote Sensing*, 57(1-2): 39-52.
- Kerle, N., 2002. Volume estimation of the 1998 flank collapse at Casita volcano, Nicaragua: A comparison of photogrammetric and conventional techniques. *Earth Surface Processes and Landforms*, 27(7): 759-772.
- Kerle, N. and de Leeuw, J., 2009. Reviving Legacy Population Maps With Object-Oriented Image Processing Techniques. *IEEE Transactions on Geoscience and Remote Sensing*, 47(7): 2392-2402.
- Kratky, V., 1989. Rigorous photogrammetric processing of SPOT images at CCM Canada. *ISPRS Journal of Photogrammetry and Remote Sensing*, 44(2): 53-71.
- Laliberte, A.S. and Rango, A., 2009. Texture and Scale in Object-Based Analysis of Subdecimeter Resolution Unmanned Aerial Vehicle (UAV) Imagery. *IEEE Transactions on Geoscience and Remote Sensing*, 47(3): 761-770.
- Laliberte, A.S. et al., 2004. Object-oriented image analysis for mapping shrub encroachment from 1937 to 2003 in southern New Mexico. *Remote Sensing of Environment*, 93(1/2): 198-210.
- Latry, C. and Rouge, B., 2003. Super resolution: quincunx sampling and fusion processing, *Geoscience and Remote Sensing Symposium. IGARSS'03*, pp. 315-317.
- Li, Z., Zhu, Q. and Gold, C., 2005. *Digital Terrain Modeling Principles and Methodology*. CRC Press, New York, 323 pp.
- Light, D.L. et al., 1980. Satellite photogrammetry. In: C.C. Slama, C. Theurer and S.W. Henriksen (Editors), *Manual of photogrammetry - 4<sup>th</sup> edition*. American Society for Photogrammetry and Remote Sensing, Bethesda, Maryland, pp. 883-977.
- Lin, M.-L. and Tung, C.-C., 2004. A GIS-based potential analysis of the landslides induced by the Chi-Chi earthquake. *Engineering Geology*, 71(1/2): 63-77.
- Loczy, D. et al., 2007. Geomorphological tasks in planning the rehabilitation of coal mining areas at Pecs, Hungary. *Geografia Fisica E Dinamica Quaternaria*, 30(2): 203-207.
- Lu, D., Batistella, M. and Moran, E., 2008. Integration of landsat TM and SPOT HRG images for vegetation change detection in the Brazilian Amazon. *Photogrammetric Engineering and Remote Sensing*, 74(4): 421-430.

- Lu, D., Mausel, P., Brondizio, E. and Moran, E., 2004. Change detection techniques. *International Journal of Remote Sensing*, 25(12): 2365-2407.
- Lu, P., Stumpf, A., Kerle, N. and Casagli, N., 2011. Object-oriented change detection for landslide rapid mapping. *IEEE Geoscience and Remote Sensing Letters*, 8(4): 701-705.
- Malamud, B.D., Turcotte, D.L., Guzzetti, F. and Reichenbach, P., 2004. Landslide inventories and their statistical properties. *Earth Surface Processes and Landforms*, 29: 687-711.
- Malleswara Rao, T.C., Venugopala Rao, K., Ravi Kumar, A., Rao, D.P. and Deekshatulu, B.L., 1996. Digital Terrain Model (DTM) from Indian Remote Sensing (IRS) satellite data from the overlap area of two adjacent paths using digital photogrammetric techniques. *Photogrammetric Engineering and Remote Sensing*, 62(6): 727-731.
- Mantovani, F., Soeters, R. and van Westen, C.J., 1996. Remote sensing techniques for landslide studies and hazard zonation in Europe. *Geomorphology*, 15(3/4): 213-225.
- Martha, T.R., Guha, A., Vinod Kumar, K., Kamaraju, M.V.V. and Raju, E.V.R., 2010a. Recent coal fire and land use status of Jharia Coalfield, India from satellite data. *International Journal of Remote Sensing*, 31(12): 3243-3262.
- Martha, T.R., Kerle, N., Jetten, V., van Westen, C.J. and Vinod Kumar, K., 2010b. Characterising spectral, spatial and morphometric properties of landslides for automatic detection using object-oriented methods. *Geomorphology*, 116(1/2): 24-36.
- Martha, T.R., Kerle, N., van Westen, C.J., Jetten, V. and Vinod Kumar, K., 2010c. Effect of sun elevation angle on DSMs derived from Cartosat-1 data. *Photogrammetric Engineering and Remote Sensing*, 76(4): 429-438.
- Martha, T.R., Kerle, N., van Westen, C.J., Jetten, V. and Vinod Kumar, K., In Press. Segment Optimisation and Data-Driven Thresholding for Knowledge-Based Landslide Detection by Object-Based Image Analysis. *IEEE Transactions on Geoscience and Remote Sensing*.
- Mathew, J., Jha, V.K. and Rawat, G.S., 2007. Weights of evidence modelling for landslide hazard zonation mapping in part of Bhagirathi valley, Uttarakhand. *Current Science*, 92(5): 628-638.
- McDermid, G.J. and Franklin, S.E., 1994. Spectral, spatial, and geomorphometric variables for the remote sensing of slope processes. *Remote Sensing of Environment*, 49: 57-71.
- McDermid, G.J. et al., 2008. Object-based approaches to change analysis and thematic map update: challenges and limitations. *Canadian Journal of Remote Sensing*, 34(5): 462-466.
- Metternicht, G., Hurni, L. and Gogu, R., 2005. Remote sensing of landslides: An analysis of the potential contribution to geo-spatial systems for hazard assessment in mountainous environments. *Remote Sensing of Environment*, 98(2-3): 284-303.
- Moine, M., Puissant, A. and Malet, J.-P., 2009. Detection of landslides from aerial and satellite images with a semi-automatic method. Application to the Barcelonnette basin (Alpes-de-Haute-Provence, France). In: J.-P. Malet, A. Remaitre and T. Bogaard (Editors), *Landslide Processes: from*

## *Bibliography*

---

- geomorphological mapping to dynamic modelling. CERG, Strasbourg, France, pp. 63-68.
- Möller, M., Lymburner, L. and Volk, M., 2007. The comparison index: A tool for assessing the accuracy of image segmentation. *International Journal of Applied Earth Observation and Geoinformation*, 9(3): 311-321.
- Murphy, M.A. and Burgess, W.P., 2006. Geometry, kinematics, and landscape characteristics of an active transtension zone, Karakoram fault system, Southwest Tibet. *Journal of Structural Geology*, 28(2): 268-283.
- Murphy, P.N.C., Ogilvie, J., Meng, F.-R. and Arp, P., 2008. Stream network modelling using lidar and photogrammetric digital elevation models: a comparison and field verification. *Hydrological Processes*, 22: 1747-1754.
- Nadim, F., Kjekstad, O., Peduzzi, P., Herold, C. and Jaedicke, C., 2006. Global landslide and avalanche hotspots. *Landslides*, 3(2): 159-173.
- Naithani, A.K., 2002. The August, 1998 Okhimath tragedy in Rudraprayag district of Garhwal Himalaya, Uttaranchal, India. *GAIA*, 16: 145-156.
- Naithani, A.K., Kumar, D. and Prasad, C., 2002. The catastrophic landslide of 16 July 2001 in Phata Byung area, Rudraprayag District, Garhwal Himalaya, India. *Current Science*, 82(8): 921-923.
- Navulur, K., 2007a. Multispectral image analysis using the object - oriented paradigm. CRC Press, Boca Raton, 165 pp.
- Navulur, K., 2007b. Multispectral image analysis using the object oriented paradigm. CRC Press, Boca Raton.
- Nayak, J., 2010. Landslide risk assessment along a major road corridor based on historical landslide inventory and traffic analysis. MSc Thesis, University of Twente Faculty of Geo-Information and Earth Observation, Enschede, The Netherlands, 104 pp.
- Negi, D.S., Kaushik, V.K. and Manocha, O.P., 2002. PAN-PAN change detection system for satellite imageries. *Defence Science Journal*, 52(3): 329-336.
- Neuhäuser, B. and Terhorst, B., 2007. Landslide susceptibility assessment using "weights-of-evidence" applied to a study area at the Jurassic escarpment (SW-Germany). *Geomorphology*, 86(1-2): 12-24.
- Nichol, J. and Wong, M.S., 2005a. Satellite remote sensing for detailed landslide inventories using change detection and image fusion. *International Journal of Remote Sensing*, 26(9): 1913-1926.
- Nichol, J. and Wong, M.S., 2005b. Satellite remote sensing for detailed landslides inventories using change detection and image fusion. *Int. J. Remote Sens.*, 26(9): 1913-1926.
- NRSC, 2006. Cartosat-1 data user's handbook. Available at [http://www.nrsc.gov.in/IRS\\_Documents/Handbook/cartosat1.pdf](http://www.nrsc.gov.in/IRS_Documents/Handbook/cartosat1.pdf).
- OFDA/CRED, 2006. EM-DAT International Disaster Database - [www.em-dat.net](http://www.em-dat.net). Université Catholique de Louvain, Brussels, Belgium.
- Okura, Y., Kitahara, H., Kawanami, A. and Kurokawa, U., 2003. Topography and volume effects on travel distance of surface failure. *Engineering Geology*, 67(3-4): 243-254.
- Otsu, N., 1979. A Threshold Selection Method from Gray-Level Histograms. *IEEE Transactions on Systems, Man and Cybernetics*, 9(1): 62-66.
- Pike, R.J., 1988. The geometric signature: Quantifying landslide-terrain types from digital elevation models. *Mathematical Geology*, 20(5): 491-511.

- Poli, S. and Sterlacchini, S., 2007. Landslide Representation Strategies in Susceptibility Studies using Weights-of-Evidence Modeling Technique. *Natural Resources Research*, 16(2): 121-134.
- Pradhan, B., 2010. Remote sensing and GIS-based landslide hazard analysis and cross-validation using multivariate logistic regression model on three test areas in Malaysia. *Advances in Space Research*, 45(10): 1244-1256.
- Prenzel, B. and Treitz, P., 2004. Remote sensing change detection for a watershed in north Sulawesi, Indonesia. *Progress in Planning*, 61(4): 349-363.
- Radhika, V.N., Kartikeyan, B., Gopala Krishna, B., Chowdhury, S. and P.K., S., 2007. Robust Stereo Image Matching for Spaceborne Imagery. *IEEE Transactions on Geoscience and Remote Sensing*, 45(9): 2993-3000.
- Rao, P.V.N. et al., 2002. Textural analysis of IRS-1D panchromatic data for land cover classification. *International Journal of Remote Sensing*, 23(17): 3327-3345.
- Rau, J.Y., Chen, L.C., Liu, J.K. and Wu, T.H., 2007. Dynamics monitoring and disaster assessment for watershed management using time-series satellite images. *IEEE Transactions on Geoscience and Remote Sensing*, 45(6): 1641-1649.
- Rawat, U.S. and Rawat, J.S., 1998. A report on geotechnical reconnaissance of the excessive landsliding in August, 1998 near Okhimath, Rudraprayag district, U.P. Technical report. Geological Survey of India, Northern Region, Lucknow.
- Ray, P.K.C. et al., 2009. Analysis of seismicity-induced landslides due to the 8 October 2005 earthquake in Kashmir Himalaya. *Current Science*, 97(12): 1742-1755.
- Rosin, P.L., 2001. Unimodal thresholding. *Pattern Recognition*, 34(11): 2083-2096.
- Rosin, P.L. and Hervas, J., 2005. Remote sensing image thresholding methods for determining landslide activity. *International Journal of Remote Sensing*, 26(6): 1075-1092.
- Sadasiva Rao, B., Murali Mohan, A.S.R.K.V., Kalyanaraman, K. and Radhakrishnan, K., 2006. Evaluation of Cartosat-I Stereo Data of Rome. *International Symposium on Geospatial Databases for Sustainable Development, International Symposium on Geospatial Databases for Sustainable Development*. ISPRS TC-IV, Goa, India.
- Sawatzky, D.L., Raines, G.L., Bonham-Carter, G.F. and Looney, C.G., 2009. Spatial Data Modeller (SDM): ArcMAP 9.3 geoprocessing tools for spatial data modelling using weights of evidence, logistic regression, fuzzy logic and neural networks. <http://arcscripts.esri.com/details.asp?dbid=15341>.
- Schneevoigt, N.J., van der Linden, S., Thamm, H.-P. and Schrott, L., 2008. Detecting Alpine landforms from remotely sensed imagery. A pilot study in the Bavarian Alps. *Geomorphology*, 93(1-2): 104-119.
- Schwarz, G., 1978. Estimating the dimension of a model. *Annals of Statistics*, 6(2): 461-464.
- Scott, K.M. et al., 2005. Catastrophic precipitation-triggered lahar at Casita volcano, Nicaragua: occurrence, bulking and transformation. *Earth Surface Processes Landforms*, 30: 59-79.
- Sezgin, M. and Sankur, B., 2004. Survey over image thresholding techniques and quantitative performance evaluation. *Journal of electronic imaging*, 13(1): 146-165.

## *Bibliography*

---

- Singhroy, V., Mattar, K.E. and Gray, A.L., 1998. Landslide characterisation in Canada using interferometric SAR and combined SAR and TM images. *Advances in Space Research*, 21(3): 465-476.
- Singhroy, V. and Molch, K., 2004. Characterizing and monitoring rockslides from SAR techniques. *Advances in Space Research*, 33(3): 290-295.
- Smith, M.J., Rose, J. and Booth, S., 2006. Geomorphological mapping of glacial landforms from remotely sensed data: An evaluation of the principal data sources and an assessment of their quality. *Geomorphology*, 76(1-2): 148-165.
- Smits, P.C. and Annoni, A., 2000. Toward specification-driven change detection. *IEEE Transactions on Geoscience and Remote Sensing*, 38(3): 1484-1488.
- Soeters, R. and van Westen, C.J., 1996. Slope Instability. Recognition, analysis and zonation. In: A.K. Turner and R.L. Schuster (Editors), *Landslide: Investigations and Mitigation. Special Report 247*. Transportation Research Board. National Academy of Sciences, Washington D.C, pp. 129-177.
- Song, C., Woodcock, C.E., Seto, K.C., Lenney, M.P. and Macomber, S.A., 2001. Classification and Change Detection Using Landsat TM Data: When and How to Correct Atmospheric Effects? *Remote Sensing of Environment*, 75(2): 230-244.
- Strahler, A.N., 1965. *Introduction to physical geography*. Wiley & Sons, New York.
- Surazakov, A.B. and Aizen, V.B., 2006. Estimating volume change of mountain glaciers using SRTM and map-based topographic data. *IEEE Transactions on Geoscience and Remote Sensing*, 44(10): 2991-2995.
- Tao, C.V. and Hu, Y., 2002. 3D Reconstruction methods based on Rational Function Model. *Photogrammetric Engineering and Remote Sensing*, 68(7): 705-714.
- Tarantino, C., Blonda, P. and Pasquariello, G., 2007. Remote sensed data for automatic detection of land-use changes due to human activity in support to landslide studies. *Natural Hazards*, 41(1): 245-267.
- Tarboton, D.G., 1997. A New Method for the Determination of Flow Directions and Contributing Areas in Grid Digital Elevation Models. *Water Resources Research*, 33(2): 309-319.
- Thiery, Y., Malet, J.P., Sterlacchini, S., Puissant, A. and Maquaire, O., 2007. Landslide susceptibility assessment by bivariate methods at large scales: Application to a complex mountainous environment. *Geomorphology*, 92(1-2): 38-59.
- Toutin, T., 2001. Elevation modelling from satellite visible and infrared (VIR) data. *International Journal of Remote Sensing*, 22(6): 1097-1125.
- Toutin, T., 2004. Comparison of stereo-extracted DTM from different high-resolution sensors: SPOT-5, EROS-A, IKONOS-II, and QuickBird. *IEEE Transactions on Geoscience and Remote Sensing*, 42(10): 2121-2129.
- Toutin, T., 2006. Generation of DSMs from SPOT-5 in-track HRS and across-track HRG stereo data using spatiotriangulation and autocalibration. *ISPRS Journal of Photogrammetry and Remote Sensing*, 60(3): 170-181.
- Toutin, T., 2008. ASTER DEMs for geomatic and geoscientific applications: a review. *International Journal of Remote Sensing*, 29(7): 1855-1875.

- Townsend, P.A. et al., 2009. Changes in the extent of surface mining and reclamation in the Central Appalachians detected using a 1976-2006 Landsat time series. *Remote Sensing of Environment*, 113(1): 62-72.
- Townshend, J.R.G. et al., 2000. Beware of per-pixel characterization of land cover. *International Journal of Remote Sensing*, 21(4): 839 - 843.
- Tralli, D.M., Blom, R.G., Zlotnicki, V., Donnellan, A. and Evans, D.L., 2005. Satellite remote sensing of earthquake, volcano, flood, landslide and coastal inundation hazards. *ISPRS Journal of Photogrammetry and Remote Sensing*, 59(4): 185-198.
- Tsutsui, K., Miyazaki, S., Nakagawa, H., Shiraishi, T. and Rokugawa, S., 2004. Data fusion techniques of heterogeneous sensor images for debris hazard assessments, IGARSS 2004. IEEE, Anchorage, Alaska.
- Tsutsui, K. et al., 2007. Detection and volume estimation of large-scale landslides based on elevation-change analysis using DEMs extracted from high-resolution satellite stereo imagery. *IEEE Transactions on Geoscience and Remote Sensing*, 45(6): 1681-1696.
- Tumuhairwe, S., 2011. Evaluation of transferability of a generic algorithm for object oriented landslide mapping and pattern analysis for the 2010 Haiti earthquake. MSc Thesis, University of Twente Faculty of Geo-information Science and Earth Observation ITC, Enschede, The Netherlands, 82 pp.
- UNESCO-WP/WLI, 1993a. *Multilingual Landslide Glossary*. Bitech Publishers Ltd, Richmond, 34 pp.
- UNESCO-WP/WLI, 1993b. A suggested method for describing the activity of a landslide. *Bulletin of the International Association of Engineering Geology*(47): 53-57.
- van Asselen, S. and Seijmonsbergen, A.C., 2006. Expert-driven semi-automated geomorphological mapping for a mountainous area using a laser DTM. *Geomorphology*, 78(3-4): 309-320.
- van Den Eeckhaut, M. et al., 2007. Use of LIDAR-derived images for mapping old landslides under forest. *Earth Surface Processes and Landforms*, 32(5): 754-769.
- Van Niel, T.G., McVicar, T.R., Li, L., Gallant, J.C. and Yang, Q., 2008. The impact of misregistration on SRTM and DEM image differences. *Remote Sensing of Environment*, 112(5): 2430-2442.
- van Westen, C.J., Castellanos, E. and Kuriakose, S.L., 2008. Spatial data for landslide susceptibility, hazard, and vulnerability assessment: An overview. *Engineering Geology*, 102(3-4): 112-131.
- van Westen, C.J. and Lulie Getahun, F., 2003. Analyzing the evolution of the Tessina landslide using aerial photographs and digital elevation models. *Geomorphology*, 54(1-2): 77-89.
- van Westen, C.J., Rengers, N. and Soeters, R., 2003. Use of geomorphological information in indirect landslide susceptibility assessment. *Natural Hazards*, 30(3): 399-419.
- van Westen, C.J., van Asch, T.W.J. and Soeters, R., 2006. Landslide hazard and risk zonation—why is it still so difficult? *Bulletin of Engineering Geology and Environment*, 65(5): 167-184.
- Varnes, D.J., 1978. Slope movements types and processes. In: R.L. Schuster and R.L. Krizek (Editors), *Landslides: Analysis and Control*. Special Report 176. Transportation Research Board, National Academy of Sciences, Washington D.C., pp. 11-33.

## *Bibliography*

---

- Varnes, D.J., 1984. Landslide Hazard Zonation: a review of principles and practice. UNESCO, Darantiere, Paris, 61 pp.
- Vinod Kumar, K., Martha, T.R. and Roy, P.S., 2006. Mapping damage in the Jammu and Kashmir caused by 8 October 2005 Mw 7.3 earthquake from the Cartosat-1 and Resourcesat-1 imagery. *International Journal of Remote Sensing*, 27(20): 4449-4459.
- Voigt, S. et al., 2007. Satellite Image Analysis for Disaster and Crisis-Management Support. *IEEE Transactions on Geoscience and Remote Sensing*, 45(6): 1520-1528.
- Wang, F. et al., 2009. Preliminary investigation of some large landslides triggered by the 2008 Wenchuan earthquake, Sichuan Province, China. *Landslides*, 6(1): 47-54.
- Weibel, R. and Heller, M., 1991. Digital terrain modelling. In: D.J. Maguire, M.F. Goodchild and D.W. Rhind (Editors), *Geographical Information Systems, Principles and Applications*, vol. 1. Longman, Harlow, pp. 269-297.
- Westaway, R.M., Lane, S.N. and Hicks, D.M., 2001. Remote sensing of clear-Water, shallow, gravel-bed rivers using digital photogrammetry. *Photogrammetric Engineering and Remote Sensing*, 67(11): 1271-1281.
- Wise, S., 2000. Assessing the quality for hydrological applications of digital elevation models derived from contours. *Hydrological Processes*, 14(11-12): 1909-1929.
- Wise, S.M., 2007. Effect of differing DEM creation methods on the results from a hydrological model. *Computers and Geosciences*, 33: 1351-1365.
- Xu, M. et al., 2010. Change detection of an earthquake-induced barrier lake based on remote sensing image classification. *International Journal of Remote Sensing*, 31(13): 3521 - 3534.
- Yan, G., Mas, J.F., Maathuis, B.H.P., Xiangmin, Z. and Van Dijk, P.M., 2006. Comparison of pixel-based and object-oriented image classification approaches - a case study in a coal fire area, Wuda, Inner Mongolia, China. *International Journal of Remote Sensing*, 27(18): 4039 - 4055.
- Zézere, J.L., Garcia, R.A.C., Oliveira, S.C. and Reis, E., 2008. Probabilistic landslide risk analysis considering direct costs in the area north of Lisbon (Portugal). *Geomorphology*, 94(3-4): 467-495.
- Zhang, H., Fritts, J.E. and Goldman, S.A., 2008. Image segmentation evaluation : a survey of unsupervised methods. *Computer vision and image understanding*, 110(2): 260-280.
- Zhang, L. and Gruen, A., 2006. Multi-image matching for DSM generation from IKONOS imagery. *ISPRS Journal of Photogrammetry and Remote Sensing*, 60(3): 195-211.
- Zhang, Q., Wang, J., Gong, P. and Shi, P., 2003. Study of urban spatial patterns from SPOT panchromatic imagery using textural analysis. *International Journal of Remote Sensing*, 24(21): 4137 - 4160.

## Summary

A comprehensive landslide inventory is a prerequisite for planning immediate landslide disaster response, and for quantitative landslide hazard and risk assessment. Interpretation of remote sensing data (aerial photographs and satellite images) and field mapping have traditionally been the most widely used techniques for generating landslide inventories. Several research attempts have been made to automate this process in order to save time. Since pixel-based methods have not produced sufficiently accurate results for detection and classification of landslides, object-oriented analysis (OOA) which imitates the human interpretation process in identification of landslides, has emerged as a good alternative recently due to the inherent ability of OOA to incorporate additional information layers such as digital terrain models (DTMs) and thematic maps in the analysis. Furthermore, as landslides are geomorphic processes, their characterisation in different types, following a classification such as the one by Varnes (1984) mostly relies on contextual criteria, which can best be described by objects obtained from segmenting the digital image into spatially cohesive regions / objects rather than pixel values.

This research outlines the development of semi-automatic image analysis algorithms that combine spectral, shape, texture, morphometric and contextual information derived from high resolution satellite data and DTMs for the preparation of new as well as historical landslide inventories. The main innovative aspect of the research lies in the selection of landslide diagnostic parameters and their use in the comprehensive characterisation of different types of landslides, a concept which is addressed for the first time for detection of landslides in an object-based environment.

DTM accuracy is an important factor since its morphometric derivatives, such as terrain curvature, slope, and flow direction, contribute to the successful detection and classification of landslides. New generation Cartosat-1 along-track stereoscopic data, which are provided with RPCs for block triangulation, were used to create a digital surface model (DSM) with 10 m grid size. Along-track satellite data have advantages for DSM generation, due to improved correlation between image pairs and high B/H ratio. However, difficulties arise in very steep areas, particularly in valleys oriented across the satellite track direction. Use of control points obtained from DGPS survey improved the absolute accuracy and resulted in vertical and planimetric RMS errors of 2.31 and <1 m, respectively, which are acceptable given the spatial resolution of Cartosat-1 only 2.5 m. However, for deriving accurate morphometric information, spatial accuracy is more important than the absolute accuracy. Therefore, drainage lines were used as a proxy to

## *Summary*

---

measure the spatial accuracy of the DSM, which showed that for valleys perpendicular to the satellite track, the DSM extracted from a low sun elevation angle data had 45 % higher spatial accuracy than the DSM extracted from high sun elevation angle data. However, in other areas these data proved to be a good source for elevation information. The research showed that sun elevation angle and local valley orientation can have a pronounced effect on the accuracy of a DSM. Conversion of a DSM to a DTM is necessary for calculating landslide volume and terrain morphometric parameters. This was done by subtracting vegetation height from the DSM. The landslide volume extracted from pre- and post-landslide DTMs without control points matched well with volume extracted from the DTMs with control points, indicating that a field survey for control points is not a strict requirement. It also showed that landslide volume information can be derived only with RPCs, if both pre- and post-image pairs can be brought into the same relative reference framework.

A set of approaches was developed that exploit the object properties extracted using a region growing segmentation of multispectral Resourcesat-1 LISS-IV Mx (5.8 m) image. Okhimath town, an area in the rugged Indian Himalayas frequently affected by landslides, was selected for developing the methodology. Landslides were characterised from an object-based detection perspective, and an algorithm comprising 45 individual routines, such as controlled segmentation, merging and classification was developed using eCognition software, which detected 42 major and minor landslides in an 80 km<sup>2</sup> area. The algorithm, consisting of three sub-modules, initially extracts landslide candidates using an NDVI threshold, and subsequently false positives were eliminated from the landslide candidates using spectral, texture, shape and contextual criteria. Landslide classification was done using terrain curvature and contextual criteria, and five different types of landslides were identified. The object-based classification when compared with a landslide inventory map prepared by stereoscopic photo-interpretation and detailed field check resulted in a detection accuracy of 76.4%, while 69.1% of the landslides were correctly classified in different landslide types. The results are considered to be good, since landslides are detected in an area dominated by false positives such as rocky barren land, uncultivated agricultural terraces and river sands. The minimum landslide size detected by the method was 774 m<sup>2</sup>, which indicates that the algorithm is not sensitive to sizes.

The algorithm developed required user defined segmentation criteria to control the object size, which was considered a drawback in applying a fast and generic method for landslide detection and classification. Therefore, an

objective method to optimise segments was developed subsequently. Using spatial autocorrelation and intrasegment variance, a new plateau objective function (POF) was developed, which was used to determine the segmentation criteria for multi-scale analysis, essential for the detection of landslides and elimination of false positives. Another drawback of the originally developed algorithm was the use of manual thresholds for the elimination of false positives from landslide candidates. This was adjusted using a K-means clustering method. The improved algorithm, comprising of four sub-modules, resulted in a detection accuracy of 76.9% for the training area and 77.7% accuracy for a geomorphologically distinct validation area. It not only increased the accuracy of detection but also reduced the overall error of commission. The objective determination of the scale factor and unsupervised selection of thresholds for landslide diagnostic parameters made an important contribution for making this method transferable to other areas.

In the previous algorithm, NDVI derived from multispectral satellite data was used in landslide detection. However, in several cases, particularly while preparing a historical landslide inventory from archived high resolution images, only panchromatic data are available. To use these data, a third algorithm, which is a modified version of the second one, was developed using a brightness threshold instead of NDVI to extract landslide candidates. Local thresholds using contextual criteria show better results than global thresholds, and allowed to identify small translational landslides within barren rocky land that are generally bright. To eliminate false positives, more texture measures, such as GLCM homogeneity and standard deviation, were used along with shape and contextual criteria. Finally, a multi-temporal annual landslide inventory for 13 years was prepared and used for the generation of a landslide susceptibility map with the help of a bivariate model (weights of evidence). The spatial probability was determined from the density of landslide for each observation period within each susceptibility class, and the temporal probability was calculated using a Gumbel frequency distribution analysis. These data were used together with the susceptibility map and a road and building map to produce a risk curve for the Okhimath area, which indicates the likely loss due to future landslide occurrences.

The final algorithm for the detection of landslides, developed in this study is generic and requires two primary inputs (a satellite image and a DTM), while *a priori* knowledge about the terrain is not mandatory. The semi-automatic approach is flexible enough to address the spatial and spectral variability of landslides and false positives. The knowledge-based method shows considerable improvement over previous pixel- and object-based methods of

### *Summary*

---

landslide detection in terms of the location, size and type of landslide. The method has increased the potential to rapidly generate event-based landslide inventories after major triggering events, within a short period of time, and without fieldwork. The method developed in this research has proven its value in several areas in the Indian Himalayas and could potentially contribute to the rapid detection of landslides in other susceptible areas.

## Samenvatting

Een inventarisatie van locaties waar aardverschuivingen zijn opgetreden is een eerste vereiste voor een adequate rampenbestrijding na een aardverschuivingramp, alsmede voor de kwantitatieve analyse van het gevaar en risico. Deze gegevens worden traditioneel verkregen door middel van een visuele interpretatie van remote sensing beelden (luchtfoto's en satellietbeelden) en veldwerk. Dit is echter een zeer tijdrovende activiteit, en het is dan ook moeilijk om snel na een ramp met veel massabewegingen in een groot bergachtig gebied een goed overzicht te krijgen van de probleemgebieden. Vandaar dat er verscheidene onderzoekspogingen zijn gedaan om dit proces te automatiseren en daardoor te versnellen. Aangezien de pixel-gebaseerde methodes niet tot voldoende nauwkeurige resultaten voor de detectie en classificatie van massabewegingen hebben geleid, wordt de nadruk steeds meer gelegd op *Object-Oriented Analysis* (OOA) als alternatief. OOA is een methode die het menselijke interpretatieproces voor de identificatie van massabewegingen kan imiteren, en maakt gebruik van aanvullende informatie zoals digitale terreinmodellen (DTM's) en thematische kaarten in de analyse. Massabewegingen zijn geomorfologische processen, en hun karakterisering in verschillende types, volgens een classificatie zoals Varnes (1984), is onder meer gebaseerd op contextuele criteria, die het beste verkregen kunnen worden door middel van het segmenteren van digitale beelden in ruimtelijk homogene objecten, in plaats van individuele pixels.

Dit onderzoek schetst de ontwikkeling van semi-automatische algoritmen voor beeldanalyse, die spectrale informatie combineren met vorm, textuur, morfometrische en contextuele informatie vanuit hoge resolutie satellietbeelden en DTM's voor de kartering van aardverschuivingen in berggebieden. Het belangrijkste innovatieve aspect van het onderzoek ligt in de selectie van typerende parameters voor massabewegingen en hun gebruik in de karakterisering van verschillende types van aardverschuivingen, met behulp van *Object-Oriented Analysis*.

De nauwkeurigheid van DTM's is binnen de analyse een belangrijke factor, aangezien de morfometrische afgeleide kaarten, zoals terreinkromming, helling, en stroomrichting, bijdragen aan het succesvol detecteren en classificeren van aardverschuivingen. *Along-track* stereoscopische data van de nieuwe Indiase Cartosat-1 satelliet, in combinatie met *Rational Polynomial Coefficients* (RPC's) voor bloktriangulering, werden gebruikt voor het maken van een digitaal oppervlaktemodel (DSM) met een resolutie van 10 meter. Deze *along-track* satellietgegevens hebben voordelen voor de generatie van een DSM, vanwege een betere correlatie tussen beeldparen en een hoge B/H verhouding. Er deden zich helaas wel moeilijkheden voor in zeer steile

## *Samenvatting*

---

gebieden, in het bijzonder in valleien die loodrecht op de satelliet bewegingsrichting waren georiënteerd. Het gebruik van controlepunten die met DGPS waren gemeten verbeterde de absolute nauwkeurigheid en resulteerde in RMS fouten van 2.31 in verticale en <1 m in planimetrische zin, welke acceptabel zijn gezien de ruimtelijke resolutie van 2.5 m voor Cartosat-1. Voor het afleiden van nauwkeurige morfometrische informatie, is de ruimtelijke nauwkeurigheid echter belangrijker dan de absolute nauwkeurigheid. Daarom werden de drainagelijnen gebruikt om de ruimtelijke nauwkeurigheid van het DSM te meten. Het onderzoek toonde aan dat de hoek van de zon waaronder de satelliet beelden genomen waren en de oriëntatie van valleien een uitgesproken effect op de nauwkeurigheid van een DSM kunnen hebben. Het DSM dat werd vervaardigd uit Cartosat-1 beelden die genomen waren onder een lage hoek van de zon resulteerde in 45% hogere nauwkeurigheid voor valleien die loodrecht georiënteerd zijn op de bewegingsrichting van de satelliet, in vergelijking met beelden die met een hoge zonnehoek gemaakt waren. Maar in andere gebieden bleken deze gegevens een goede bron voor hoogte informatie te zijn.

De omzetting van een digitaal oppervlakte model (DSM) naar een digitaal terreinmodel (DTM) is noodzakelijk voor het berekenen van het volume van massabewegingen en voor het bepalen van morfometrische parameters. Dit werd gedaan door de vegetatiehoogte van het DSM af te trekken. Het gebruik van controlepunten bij het maken van DTM's voor en na een aardverschuiving bleek geen grote verschillen op te leveren in de berekening van het volume. Hieruit kan worden geconcludeerd dat voor dergelijk onderzoek het gebruik van controlepunten geen strikte vereiste is, en dat de volume informatie slechts met het gebruik van RPC's kan worden bepaald, als beide beelden in hetzelfde relatieve referentiekader worden gebracht.

Een reeks benaderingen werd ontwikkeld die de eigenschappen bepaald van objecten die geëxtraheerd zijn uit een multi-spectraal beeld van Resourcesat-1 LISS-IV Mx (5.8 m resolutie) door middel van een *region-growing* algoritme. Als testgebied voor het ontwikkelen van de methodologie werd het gebied rondom Okhimath geselecteerd, in de deelstaat Uttarakhand in het Himalayagebergte. De aardverschuivingen werden gedetecteerd met OOA, en een algoritme dat uit 45 individuele routines bestaat, waaronder een gecontroleerde segmentatie, het samenvoegen van objecten en de classificatie in verschillende types. Voor deze analyse werd de eCognition software gebruikt, en de analyse resulteerde in de detectie en classificatie van 42 aardverschuivingen van verschillende grootte in een gebied van 80 km<sup>2</sup>. Het algoritme, dat uit drie submodules bestaat, extraheert eerst mogelijke aardverschuivingen door middel van een NDVI drempelwaarde,

waarna de *fout-positieven* geëlimineerd worden op basis van spectrale, textuur, vorm en contextuele criteria. Classificatie van de objecten in 5 types van massabewegingen werd vervolgens uitgevoerd d.m.v. morfometrische en contextuele criteria. De OOA-gebaseerde classificatie werd vervolgens vergeleken met een kartering gebaseerd op stereoscopische luchtfoto-interpretatie en veldwerk. Daaruit bleek dat de opsporingsnauwkeurigheid 76.4% was, terwijl de classificatie in 69.1% van de gevallen correct was. Deze relatief goede resultaten konden worden behaald, ondanks het feit dat in het gebied veel *fout-positieven* aanwezig zijn, zoals niet begroeid rotsachtig terrein, landbouwterrassen, and rivierafzettingen. De minimum grootte van aardverschuivingen die door deze methode kon worden gedetecteerd was 774 m<sup>2</sup>, wat erop wijst dat het algoritme niet gevoelig voor grootte is. Het ontwikkelde algoritme vereist nog wel een zekere mate van gebruikersinteractie voor het bepalen van segmentatiecriteria voor de objectgrootte, wat een nadeel is in de toepassing als een snelle en generieke methode. Daarom werd vervolgens een meer objectieve methode om segmenten te optimaliseren ontwikkeld. Een nieuwe *Plateau Objective Function* (POF) werd ontwikkeld m.b.v. ruimtelijke autocorrelatie en intrasegment variantie, die werd gebruikt om de segmentatiecriteria voor multi-schaal analyse te bepalen, welke essentieel zijn voor de opsporing van aardverschuivingen en de verwijdering van *fout-positieven*. Een ander nadeel van het oorspronkelijk ontwikkelde algoritme was het gebruik van subjectieve drempelwaardes voor de verwijdering van *fout-positieven*. Dit werd aangepast met behulp van een *K-means* clustermethode. Het verbeterde algoritme, bestaande uit vier submodules, resulteerde in een opsporingsnauwkeurigheid van 76.9% voor het testgebied en 77.7% voor een geomorfologisch verschillend validatiegebied in Darjeeling. Het nieuwe algoritme verhoogde de nauwkeurigheid van detectie, maar verminderde ook het aantal onterecht geclassificeerde aardverschuivingsobjecten. Het vernieuwde algoritme is sneller te gebruiken en is beter in te zetten in andere gebieden, vanwege de objectieve bepaling van de schaalfactor en de automatische selectie van drempelwaardes voor relevant parameters.

De bovengenoemde algoritmes maken gebruik van NDVI waardes die uit multi-spectrale satellietbeelden worden berekend. Echter in veel gevallen zijn deze multi-spectrale beelden niet beschikbaar, bijvoorbeeld wanneer historische beelden gebruikt worden voor het maken van een multi-temporele database van massabewegingen. In veel van dit soort gevallen zijn alleen gearchiveerde panchromatische beelden beschikbaar. Om ook deze gegevens te kunnen gebruiken, werd een derde algoritme ontwikkeld, waarbij een drempelwaarde voor de reflectie werd gebruikt in plaats van NDVI voor de detectie van mogelijke aardverschuivingen.

## *Samenvatting*

---

De bepaling van lokale drempelwaardes die contextuele criteria gebruiken tonen betere resultaten dan globale drempels, en maken het mogelijk om kleine oppervlakkige afglijdingen te detecteren zelfs binnen onbegroeid rotsachtig gebied. Voor het elimineren van *fout-positieven* werden een aantal textuur gerelateerde criteria gebruikt, zoals *Grey Level Co-occurrence Matrix (GLCM)* homogeniteit en standaardafwijking, samen met informatie over vorm en contextuele criteria. Met behulp van deze methode werden jaarlijkse inventarisatiekaarten van massabewegingen geproduceerd voor een periode van 13 jaar. Deze werden gebruikt voor het genereren van een gevoeligheidskaart voor aardverschuivingen met behulp van de zogenaamde *Weights-of-Evidence* methode. De ruimtelijke waarschijnlijkheid werd bepaald aan de hand van de dichtheid van massabewegingen per gevoeligheidsklasse voor elke observatieperiode. De temporele waarschijnlijkheid voor massabewegingen werd bepaald met behulp van een *Gumbel* analyse. Deze gegevens werden gebruikt samen met de gevoeligheidskaart en informatie over wegen en gebouwen voor het produceren van een risico curve voor het gebied, waarin de jaarlijkse kans op schade bepaald wordt voor toekomstige massabewegingen.

Het uiteindelijke algoritme voor de detectie en classificatie van aardverschuivingen dat in deze studie werd ontwikkeld is generiek en vereist twee primaire invoergegevens (een satellietbeeld en een DTM), en vereist geen *a priori* kennis over het terrein. De halfautomatische benadering is flexibel genoeg om de ruimtelijke en spectrale variabiliteit van aardverschuivingen te analyseren en het aantal *fout-positieven* beperkt te houden. Deze methode is een aanzienlijke verbetering vergeleken met eerder ontwikkelde op pixels gebaseerde classificatiemethodes. Het stelt de gebruiker in staat om in korte tijd een inventarisatie te maken van aardverschuivingen die veroorzaakt zijn door extreme regenval of aardbevingen, en levert informatie over de locatie, types en de grootte van massabewegingen. De methode die in dit onderzoek werd ontwikkeld heeft zijn waarde bewezen in verscheidene gebieden in het Indiase Himalayagebergte en biedt de mogelijkheid tot een snelle inventarisatie van massabewegingen in andere gebieden op de wereld.

## Biography



Tapas Ranjan Martha was born on 05 August 1977 in Begunia, Khurda district, Odisha state, India. He is a gold medalist from the Khallikote (Autonomous) college, Berhampur, Odisha, India, where he completed his bachelor degree in Geology (Hons.) during 1993 to 1996 period. He worked on his MSc. Tech degree in applied geology from 1996 to 1999 at the Indian School of Mines (ISM), Dhanbad, India ([www.ismdhanbad.ac.in](http://www.ismdhanbad.ac.in)), and continued there as a researcher from 1999 to 2001. In 2001 he joined the National Remote Sensing Centre (NRSC) of the Indian Space Research Organisation (ISRO), Department of Space, Government of India ([www.nrsc.gov.in](http://www.nrsc.gov.in)) in Hyderabad, India as a scientist. Since then his work has mainly focused on image interpretation for the preparation of thematic layers and their integration in GIS for several geotechnical, mineral and oil exploration, and geo-environmental projects. He has contributed to landslide hazard zonation (LHZ) program of ISRO. Now he is involved in the National Geomorphological and Lineament mapping project (NGM), which aims at preparation of geomorphological and lineament maps of India on 1:50,000 scale. In 2007, he was deputed to ITC, The Netherlands to carry out advanced research on rapid detection of landslides from Earth Observation (EO) data under a GSI-NRSC-ITC joint agreement. The PhD thesis is the outcome of the research done under the agreement. He can be reached through E-mail: [trmartha@rediffmail.com](mailto:trmartha@rediffmail.com); [tapas\\_martha@nrsc.gov.in](mailto:tapas_martha@nrsc.gov.in); [tapas1977@gmail.com](mailto:tapas1977@gmail.com).

## Publications

1. **Tapas R. Martha**, N. Kerle, Cees J. van Westen, V. Jetten and K. Vinod Kumar (2010) Effect of sun elevation angle on DSMs derived from Cartosat - 1 data. *Photogrammetric Engineering and Remote Sensing*, 76 (4), 429-438.
2. **Tapas R. Martha**, N. Kerle, V. Jetten, Cees J. van Westen and K. Vinod Kumar (2010) Landslide volumetric analysis using Cartosat - 1 derived DEMs. *IEEE Geoscience and Remote Sensing Letters*, 7 (3), 582-586.
3. **Tapas R. Martha**, N. Kerle, V. Jetten, Cees J. van Westen and K. Vinod Kumar (2010) Characterising spectral, spatial and morphometric properties of landslides for semi - automatic detection using object - oriented methods. *Geomorphology*, 116 (1-2), 24-36.
4. **Tapas R. Martha**, N. Kerle, Cees J. van Westen, V. Jetten and K. Vinod Kumar (2011) Segment optimisation and data-driven thresholding for knowledge-based landslide detection by object-based image analysis. *IEEE Transactions on Geoscience and Remote Sensing* (In press).
5. Martha, T.R., Kerle, N., van Westen, C.J., Jetten, V.G. and Kumar, K.V. (2011) Object-oriented analysis of multi-temporal panchromatic images for creation of historical landslide inventories. *Remote Sensing of Environment* (In revision).
6. Martha, T.R., van Westen, C.J., Kerle, N., Jetten, V.G. and Kumar, K.V. (2011) Landslide hazard and risk assessment using landslide inventories created semi-automatically by object-oriented analysis. *Journal of the Geological Society of India* (In revision).
7. **Tapas R. Martha**, N. Kerle, Cees J. van Westen and K. Vinod Kumar (2008) High resolution DEM from Cartosat - 1 for landslide investigation in the Himalayan region, India. In: European Geosciences Union (EGU) General Assembly, 13-18 April 2008, Vienna, Austria (in CDROM).
8. N. Kerle and **Tapas R. Martha**, (2010) The potential of object - based and cognitive methods for rapid detection and characterisation of landslides. In: 6<sup>th</sup> International Symposium on Geo-information for Disaster Management, 2-4 February 2010, Torino, Italy (in CDROM).
9. **Tapas R. Martha**, N. Kerle (2010) Segment optimisation for object - based landslide detection. In: GEOBIA 2010: geographic object - based image analysis, 29 June-2 July 2010, Ghent, Belgium: proceedings / editor E.A. Addink, F.M.B. Van Coillie: International Society for Photogrammetry and Remote Sensing (ISPRS), 2010. - (International Archives of Photogrammetry and Remote Sensing: IAPRS: ISPRS; XXXVIII-4/C7), 6 p (in CDROM).
10. **Tapas R. Martha** and N. Kerle (2010) Object - oriented and cognitive detection and characterisation of landslides. Presented at the 8th International Workshop on Remote Sensing for Disaster Management, 30 September-1 October 2010, Tokyo, Japan. 2 p.

## **ITC Dissertation List**

[http://www.itc.nl/Pub/research\\_programme/Graduate-programme/Graduate-programme-PhD\\_Graduates.html](http://www.itc.nl/Pub/research_programme/Graduate-programme/Graduate-programme-PhD_Graduates.html)